BARRIER ENGINEERING FOR HIGH-PERFORMANCE nBn INFRARED PHOTODETECTORS

A THESIS SUBMITTED TO
THE GRADUATE SCHOOL OF NATURAL AND APPLIED SCIENCES
OF
MIDDLE EAST TECHNICAL UNIVERSITY

BY

FATİH UZGUR

IN PARTIAL FULFILLMENT OF THE REQUIREMENTS
FOR
THE DEGREE OF DOCTOR OF PHILOSOPHY
IN
MICRO AND NANOTECHNOLOGY

AUGUST 2020

Approval of the thesis:

BARRIER ENGINEERING FOR HIGH-PERFORMANCE nBn INFRARED PHOTODETECTORS

submitted by **FATİH UZGUR** in partial fulfillment of the requirements for the degree of **Doctor of Philosophy in Micro and Nanotechnology, Middle East Technical University** by,

Prof. Dr. Halil Kalıpçılar
Dean, Graduate School of **Natural and Applied Sciences** _____

Prof. Dr. Almıla Güvenç Yazıcıoğlu
Head of the Department, **Micro and Nanotechnology** _____

Assoc. Prof. Dr. Serdar Kocaman
Supervisor, **Electrical - Electronics Eng., METU** _____

Assoc. Prof. Dr. Alpan Bek
Co-Supervisor, **Physics, METU** _____

Examining Committee Members:

Prof. Dr. Cengiz Beşikci
Electrical - Electronics Eng., METU _____

Assoc. Prof. Dr. Serdar Kocaman
Electrical - Electronics Eng., METU _____

Prof. Dr. Mehmet Parlak
Physics, METU _____

Prof. Dr. Uğur Serincan
Physics, Eskişehir Tech. Uni. _____

Assoc. Prof. Dr. Mustafa Kulakcı
Physics, Eskişehir Tech. Uni. _____

Date: 06.08.2020

I hereby declare that all information in this document has been obtained and presented in accordance with academic rules and ethical conduct. I also declare that, as required by these rules and conduct, I have fully cited and referenced all material and results that are not original to this work.

Name, Last name : Fatih Uzgur

Signature :

ABSTRACT

BARRIER ENGINEERING FOR HIGH-PERFORMANCE nBn INFRARED PHOTODETECTORS

Uzgur, Fatih
Doctor of Philosophy, Micro and Nanotechnology
Supervisor: Assoc. Prof. Dr. Serdar Kocaman
Co-Supervisor: Assoc. Prof. Dr. Alpan Bek

August 2020, 170 pages

Despite intensive studies, for high-performance applications, lowering dark current is still a challenging problem for pn-type infrared (IR) photodetectors. Over the last two decades, barrier-type IR detectors have been proposed as a solution for obtaining high-performance and high operation temperature conditions. However, the valence band discontinuity limits the material alternatives to which the barrier detector architecture can be applied. In this thesis work, it has been numerically shown that some material limitations in the barrier detector architecture can be eliminated using bandgap engineering techniques. Herein, simulations and analyses were performed by using Synopsys Sentaurus technology computer-aided design (TCAD) commercial device simulator via calculations of the current, continuity, and Poisson's equations with high precision. In this study, delta-doped layers, together with compositionally grading, were utilized to get InGaAs and HgCdTe nBn type IR barrier detector configurations. For the shortwave IR (SWIR) band InGaAs nBn detector, lattice-matched InAlAs and lattice-mismatched InGaAs were used for the barrier material. At least 40 and 20 times improvement, respectively, were calculated

in the dark current level by suppressing the surface leakage and generation-recombination (G-R) current mechanisms without compromising any photo-response when compared to the conventional pn junction. This method was also applied successfully for obtaining an extended SWIR (eSWIR)/SWIR InGaAs dual-band nBn detector structure. In the case of HgCdTe material systems, strong suppression of G-R and trap assisted tunneling (TAT) currents were numerically demonstrated with the designed nBn structures in the SWIR, midwave IR (MWIR), and longwave IR (LWIR) bands, which could be useful for the alternative substrate HgCdTe technology. The HgCdTe dual-band nBn detector configuration was also examined in MWIR/LWIR bands again by using compositionally graded and delta-doped layers. Thanks to the flexibility of this method, the length and thickness of the barrier can be adjusted, while zero valence band offset is achieved at the same time for the compositionally bandgap adjustable materials.

Keywords: Infrared detectors, InGaAs, HgCdTe, unipolar barrier detector, nBn

ÖZ

YÜKSEK PERFORMANSLI nBn KIZILÖTESİ FOTODEDEKTÖRLER İÇİN BARİYER MÜHENDİSLİĞİ

Uzgur, Fatih
Doktora, Mikro ve Nanoteknoloji
Tez Yöneticisi: Doç. Dr. Serdar Kocaman
Ortak Tez Yöneticisi: Doç. Dr. Alpan Bek

Ağustos 2020, 170 sayfa

Yüksek performans uygulamaları için pn kızılötesi foto dedektörlerinde karanlık akımı azaltmak, yoğun çalışmalara rağmen hala zorlu bir problemdir. Son yirmi yıldır bariyer tipi kızılötesi dedektörler, yüksek performans ve yüksek çalışma sıcaklığı koşulları için bir çözüm olarak önerilmektedir. Ancak valans bandı süreksizliği bariyer dedektör mimarisinin uygulanabileceği dedektör malzemelerini sınırlamaktadır. Bu tez çalışmasında bant aralığı mühendisliği teknikleri kullanılarak bariyer dedektör mimarisindeki bazı malzeme sınırlamalarının ortadan kaldırılabileceği nümerik olarak gösterilmiştir. Bu çalışmada ticari Synopsys Sentaurus TCAD simülatörü kullanılarak akım, süreklilik ve Poisson denklemlerinin yüksek hassasiyetle hesaplandığı simülasyonlar ve analizler yapılmıştır. Bu çalışmada bant aralığı derecelendirme ve delta katkılı katmanlar kullanılarak InGaAs ve HgCdTe nBn dedektör yapıları elde edilmiştir. SWIR InGaAs nBn dedektörleri için örgü uyumlu InAlAs ve örgü uyumsuz InGaAs malzemeleri bariyer katmanı olarak kullanılmıştır. Yüzey sızıntı ve G-R akım mekanizmaları baskılanarak, konvansiyonel InGaAs pn dedektörüne kıyasla, foto tepkiden ödün vermeksizin karanlık akım seviyesinde InAlAs bariyerli dedektör için en az 40 kat ve InGaAs

bariyerli dedektör için de en az 20 kat iyileşme gösterilmiştir. Ayrıca önerilen bu metot, e-SWIR/SWIR InGaAs çift bantlı nBn dedektör yapısının elde edilmesinde de başarıyla uygulanmıştır. Diğer bir çalışmada, HgCdTe malzemesi ile SWIR, MWIR ve LWIR dalga boyu aralıkları için nBn dedektörü tasarlanmıştır. Bu tasarlanan yapılarda G-R ve TAT akımlarının güçlü bir şekilde bastırıldığı ve önerilen bu yöntemin alternatif taban HgCdTe teknolojisi için de uygulanabilir olduğu gösterilmiştir. Yine bu tezde HgCdTe MWIR/LWIR çift bantlı nBn dedektör yapısı, aynı yöntem (bant aralığı derecelendirme ve delta katkılı katmanlar) kullanılarak nümerik olarak ortaya konulmuştur. Bu yöntemin esnekliği sayesinde kompozisyonla bant aralığı değiştirilebilen dedektör malzemeleri için bariyer yüksekliği ve kalınlığı ayarlanabilirken, aynı zamanda sıfır valans bant ofseti de elde edilebilmektedir.

Anahtar Kelimeler: Kızılötesi dedektörler, InGaAs, HgCdTe, tek-kutuplu bariyer dedektör, nBn

To my parents Kadriye and Harun,

and

to my wife Melek and my son Ömer Salih

ACKNOWLEDGMENTS

First, I would like to express my deep and sincere gratitude to my research supervisor Assoc. Prof. Dr. Serdar Kocaman for allowing me the opportunity to perform this research and providing his invaluable guidance throughout this work. His dynamism, vision, sincerity, and motivation have inspired me deeply. With his guidance, I was able to learn the methodology to conduct this research and present the work as clearly as possible. It has been a great privilege and honor to work and study under his guidance.

I would like to thank Prof. Dr. Cengiz Beşikci for giving me the opportunity to do research in a highly sophisticated laboratory in addition to his technical comments and enlightening discussions.

I would like to thank my co-supervisor, Assoc. Prof. Dr. Alpan Bek for his constant support and suggestions.

I would like to thank Prof. Dr. Mehmet Parlak, Prof. Dr. Uğur Serincan and Assoc. Prof. Dr. Mustafa Kulakcı for their valuable comments and being on my thesis committee.

I would like to thank Alper Şahin, Musa Selim Gül, Abdulkadir Gürbüz, Halil İbrahim Binici, Eren Deniz Tansel, Hatice Hatipoğlu, Tolga Yıldırım, Necati Işık, Elif Merve Özalp, Onur Tanış, Tuğçe Demirsoy Çetin and Ebru Kızıl for their friendship, help and enjoyable moments in and outside of laboratory.

I would like to thank M. Halid Dolaş, Kübra Çırçır, Yiğit Özer, Kaan Sel, Utku Karaca, Eray Yurtseven, Ekin Kızılkan and Muammer Kozan for their technical comments as well as their friendship.

I would like to thank Alaaddin Öztürk, Alptekin Aydınlı, Aydın Sinan Apaydın, Davut Divarcioğlu, Abdulhamit Dönder, Hasan Burhan Beytur, Celal İler, Oruç Altıntaşı, Furkan Karakaya, Mehmet Gilik, Adil Adilli, Utku Çekmez, Alim

Yolalmaz, Fırat Es, Emine Hande Çiftpınar, İsmail Kabaçelik, Salar H. Sedani, Hidayet Samedov, Nariman Pashayev, Tural Jafarli and Yakup Midilli for their friendship, help and enjoyable moments in and outside the campus.

I would like to thank Scientific and Technological Research Council of Turkey (TUBITAK) for partially funding this work under grant number TUBITAK 118E771.

I would like to thank Mr. Özgür Şen for his extraordinary effort to keep the laboratory working and his friendship.

I would like to express my special thanks to Mr. Doğan Ketencigil for his encouragement to the academic study.

I would like to express my extremely grateful to my parents Kadriye and Harun for their love, prayers, caring and sacrifices for educating and preparing me for my future.

I would like to express my thanks to my sisters Rumeysa Uzgur, Esra Topbaç and Vildan Öztürk for their endless support and valuable prayers.

I would also like to express my thanks to my wife's parents Şaziye and Muharrem Çelik and my sister in law Elif Çelik for understanding and continuing support.

Last but not least, I am immensely grateful to my wife Melek and my son Ömer Salih. I appreciate their patience, sacrifice, and moral support.

TABLE OF CONTENTS

LIST OF TABLES

TABLES

LIST OF FIGURES

FIGURES

LIST OF ABBREVIATIONS

ABBREVIATIONS	
IR	Infrared
TCAD	Technology Computer-Aided Design
SWIR	Short Wavelength Infrared
MWIR	Mid Wavelength Infrared
LWIR	Long Wavelength Infrared
VLWIR	Very Long Wavelength Infrared
eSWIR	Extended Short Wavelength Infrared
InGaAs	Indium Gallium Arsenide
InAlGaAs	Indium Aluminum Gallium Arsenide
InP	Indium Phosphide
GaAs	Gallium Arsenide
GaSb	Gallium Antimonide
AlSb	Aluminum Antimonide
InAs	Indium Arsenide
InAsSb	Indium Arsenide antimonide
CdZnTe	Cadmium Zinc Telluride
HgCdTe	Mercury Cadmium Telluride
MCT	Mercury Cadmium Telluride
FPA	Focal Plane Array
VOx	Vanadium Oxide
PbS	Lead sulfide
PbSe	Lead selenide
PbSnTe	Lead Tin Telluride
Si	Silicon
G-R	Generation-Recombination
TAT	Trap Assisted Tunneling
BTBT	Band to Band Tunneling
SRH	Schockley-Read-Hall

CCD	Charge-Coupled Device
QWIP	Quantum Well Infrared Photodetector
QDIP	Quantum dot infrared photodetector
NEP	Noise Equivalent Power
BLIP	Background Limited Performance
PV	Photovoltaic
ABCS	Antimonite Based Compound Semiconductors
CBIRD	Complementary Barrier Infrared Detector
eB	Electron Barrier
hB	Hole Barrier
SL	Super Lattice
DHBT	Double Heterojunction Bipolar Transistor
CGS	Compositionally Graded Semiconductor
VCSEL	Vertical-Cavity Surface-Emitting Laser
PDEs	Partial Differential Equations
TEC	Thermoelectric Cooler
UAV	Unmanned Aerial Vehicle
MOSFET	Metal Oxide Semiconductor Field Effect Transistor
HBT	Heterojunction Bipolar Transistor
HEMT	High-electron-mobility transistor
OICD	Optoelectronic integrated circuit devices
PD	Photodiode
APD	Avalanche Photodiode
MBE	Molecular beam epitaxy
DLHJ	Double Layer Heterojunction
TLHJ	Two-color Triple Layer Heterojunction
HDVIP	High-Density Vertically Integrated Photodetector

CHAPTER 1

INTRODUCTION

Infrared (IR) light is an electromagnetic (EM) radiation whose wavelength range covers from ~ 0.7 μm to ~ 1000 μm of the EM spectrum. It is emitted from every substance, including the human body, due to vibration or rotation of atoms or molecules at any temperature [1].

With advanced IR detection techniques, remarkable progress has been made in the scientific, space, medical, civilian and military fields, such as spectroscopy, deep space exploration, hyperspectral remote sensing, medical IR thermography, meteorology, telecom, laser imaging detection and ranging (LIDAR), night vision, laser marking, anti-air missile seekers, chemical detection and surveillance.

IR detectors are transducers that convert IR radiation into electrical signals. The detection can be achieved by using thermal or photon detectors. For thermal detectors, the radiation collected as heat is converted into electric signals. In photodetectors, on the other hand, electrical signals are generated due to a change in the electrical conductivity of the active medium [2]. Although thermal detectors have lower production costs, they are not advantageous for applications requiring high performance due mainly to their slow response. Photon IR detectors are much more preferred for high-performance applications since they have fast response and in addition, spectral information. However, the cooling requirement limits the application areas of photon detectors because of economic and technical reasons.

This thesis work presents the valence band compensated nBn architecture as a solution to reach a high-performance IR photon detector structure. In the remainder of this chapter, a summary of the history of the IR detectors, and types of IR detectors, are presented together with the output of the thesis work.

In the second chapter, dark current mechanisms and performance parameters are discussed. In the third chapter, the concepts of barrier detectors and a literature review are reported. In the fourth chapter, the applied nBn architecture and technology computer-aided design (TCAD)-based simulation method are presented. In the fifth chapter, first, InGaAs shortwave IR (SWIR) detector technologies are reviewed, and then All InGaAs barrier detectors, InAlGaAs lattice-matched barrier InGaAs nBn detector and dual-band InGaAs detector designs are presented with their performance and sensitivity analyses. In the sixth chapter, first, HgCdTe material and detector technologies are reviewed, and then the same method is applied for HgCdTe material in the shortwave IR (SWIR), midwave IR (MWIR), longwave IR (LWIR), and also MWIR/LWIR dual-band nBn structures. In the last chapter, conclusions and future work are discussed.

1.1 A Brief History of Infrared Detectors

The existence of IR light was discovered for the first time by Herschel in 1800 [3]. He measured temperature change under different colors of sunlight spectrum using thermometers and a prism (Figure1.1). He realized that the highest temperature was measured immediately after the red region of the spectrum. In subsequent experiments, Herschel found that beyond the red region of the spectrum, there were invisible light rays that showed optical properties as visible light.

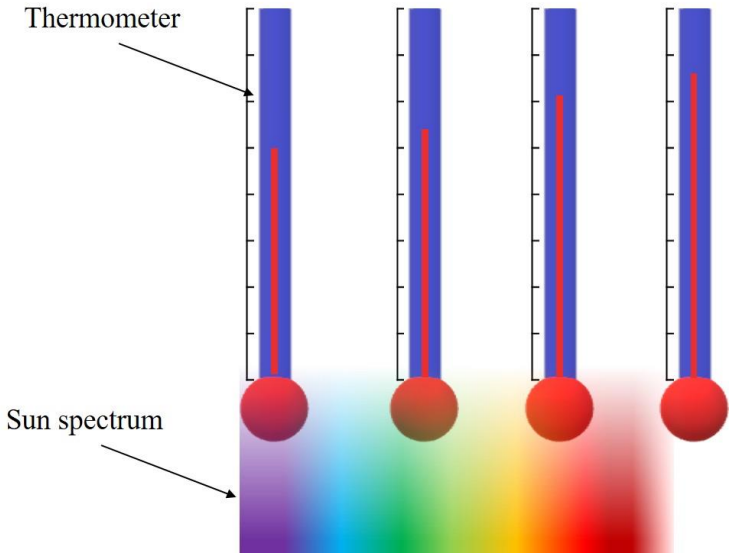

Figure 1.1. Herschel's experiment setup (redrawn from ref. [3]).

The next significant progress was made by Thomas Johann Seebeck in 1821. His invention can be considered as the starting point for thermal sensors. He measured a small electric current between junctions that were made of different metals and kept at different temperatures using a compass magnet [4]. Later, Nobili invented the first thermocouple based on Seebeck's thermoelectric effect in 1829 [5]. Four years later, Melloni came up with the idea of an integrated thermocouple (thermopile). It was so sensitive that it could detect the temperature of a person standing 30 feet away [5]. In 1880, Samuel Pierpont Langley invented the first

bolometer, which was more sensitive than thermopiles [5]. The bolometer basically is consisted of two thin platinum foils connected with two arms of a Wheatstone bridge, which is a circuit used for sensitive measurement of the variation of the resistance. He used the bolometer for studying solar irradiance intensity in the IR region [5].

The IR detectors mentioned thus far have been classified as thermal detectors. The first photon detector was developed by Theodore W. Case in 1919 [5]. He showed that some sulfide salts had photoconductive behavior and exhibited a good reaction in the red region of the spectrum. He then patented the "Thalofide cell", which was composed of sulphur, thallium, and oxygen. These detectors showed maximum sensitivity at 1 μm wavelength [6].

Since the discovery of IR radiation, different detector technologies have been developed. In addition to that mentioned above, the detector technologies that have emerged to date can be listed as follows: Golay cell, pyroelectric detectors, photon drag, Josephson junctions, Schottky barriers, intrinsic photodetectors, extrinsic photodetectors, superlattice detectors, quantum well detectors, quantum dot detectors and barrier-type IR detectors [7]. Some of these detector technologies are discussed later in this chapter.

1.2 Basics of Infrared Detection

1.2.1 Blackbody Radiation

Electromagnetic (EM) radiation is a wave that consists of packets of EM energy called photons. Bands of the EM spectrum is shown in Figure 1.2.

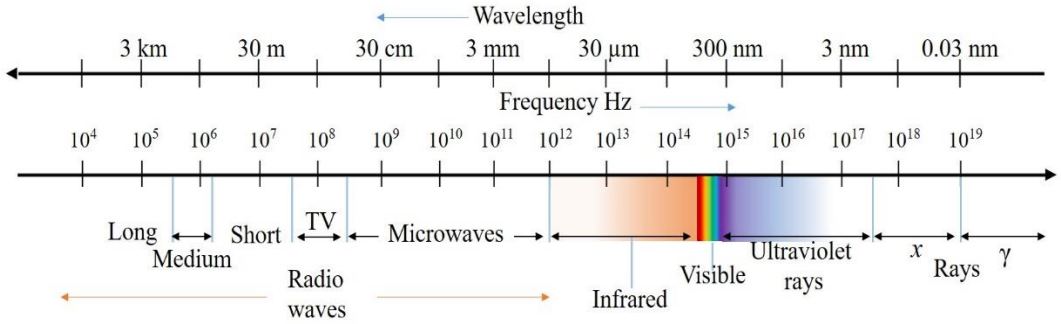

Figure 1.2. Bands of the EM spectrum with frequency and wavelength ranges (redrawn from ref. [2]).

In general, in the case of the visible and the IR regions, the unit of light is expressed in terms of wavelengths, since frequencies of these regions are around the millions of megahertz and a wavelength of light can be very sensitively measured. The relation between wavelength, frequency and the energy of a photon (ε) is given in Eq. (1.1):

$$c = \lambda\nu, \qquad \varepsilon = h\nu = \frac{hc}{\lambda} \tag{1.1}$$

where c is the speed of the light in free space (~ 3×10^8 m/s), λ is the wavelength, υ is the optical frequency, and h is the Planck constant (6.62×10^{-34} J.s).

The nature of radiation emissions from matter is explained by the blackbody phenomena [2]. A blackbody is a hypothetical object that perfectly absorbs and emits every wavelength of the EM spectrum. In the thermal equilibrium, the relationship between the incident and emitted radiation from a substance is given by Kirchhoff's law of thermal radiation:

$$1 = \alpha + \rho + T \tag{1.2}$$

where α is the absorbance, ρ is the reflectance and T is the transmittance.

The most accurate expression of the spectral radiance of a blackbody is given by Planck's equation [5]:

$$M_\lambda(\lambda, T) = \frac{2\pi hc^2}{\lambda^5} \frac{1}{e^{hc/\lambda kT} - 1} \tag{1.3}$$

where $M_\lambda(\lambda, T)$ is the spectral radiant exitance (W/cm^2-μm), h is Planck's constant, c is the speed of light, T is the absolute temperature of the object, and k is the Boltzmann constant. The blackbody radiant exitance spectrum for different temperatures is shown in Figure 1.3.

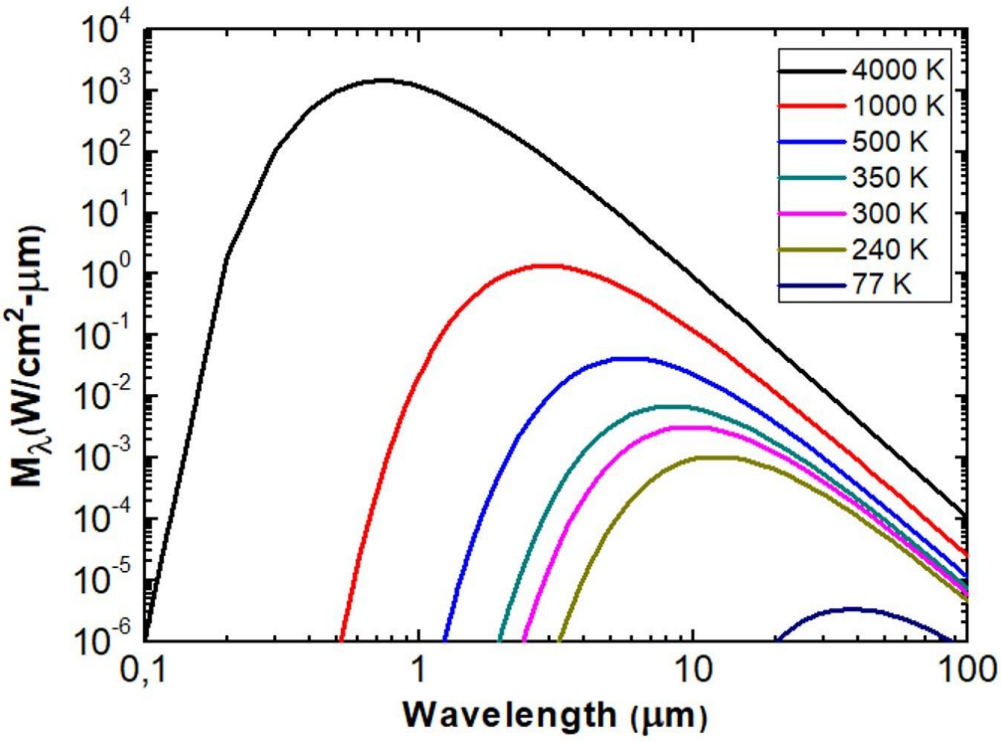

Figure 1.3. Blackbody radiation spectrum (redrawn from ref. [8]).

$$\lambda_{max} = \frac{2898\ \mu m.K}{T}. \quad (1.4)$$

At room temperature, the maximum radiant exitance of a blackbody is observed at a wavelength of around 10 μm. As the temperature increases, the peak wavelength shifts to short wavelengths and the total radiant exitance increases. If spectral radiant exitances are integrated over all wavelengths, the total radiant exitance can be calculated using Eq. (1.5) [2]:

$$M(T) = \int_0^\infty M_\lambda\,(\lambda, T)d\lambda = \int_0^\infty \frac{2\pi hc^2}{\lambda^5(e^{\frac{hc}{\lambda kt}} - 1)} d\lambda = \frac{2\pi^5 k^4}{15c^2h^3} T^4 = \sigma T^4 \quad (1.5)$$

where $\sigma = 5.67\times10^{-12}$ W/cm^{2}K^4 (the Stefan–Boltzmann constant).

The spectrum given by a blackbody indicates the theoretical upper limit that a source can radiate for any specific temperature.

At the same temperature, the ratio of the spectral exitance of a source to a blackbody is called emissivity:

$$\varepsilon(\lambda, T) = \frac{M(\lambda, T)_{Source}}{M(\lambda, T)_{Blackbody}}. \quad (1.6)$$

In general, the emissivity depends on wavelength and temperature. Emissivity has no unit and its value varies between 0 and 1. For an ideal blackbody, this value is ε = 1 and is independent of the wavelength and temperature.

1.2.2 Atmospheric Transmission

In the presence of an atmosphere, operation of the IR detectors are affected by the physical and chemical contents of the air. Therefore, specifications of the detector should be determined according to the properties of the atmosphere. In particular, scattering and absorption affect the transmission of the IR light in the atmosphere, but this effect will appear differently for each wavelength interval.

If the particle size is larger than the wavelength in the atmosphere, the scattering of the IR light does not depend on the wavelength of the IR beam (Mie scattering). However, if the size of the particles is comparible to the wavelength, scattering is inversely proportional to the fourth power of the wavelength ($1/\lambda^4$, Rayleigh scattering).

The atmospheric transmission spectrum of IR light through 2 km at sea level is shown in Figure 1.4. Since some gas compounds of the atmosphere absorb IR light at certain wavelengths, the detection of these absorbed wavelengths would be restricted.

In general, the atmospheric transmission spectrum is mainly divided into three bands according to the atmospheric absorption. Mostly, water, oxygen, carbon dioxide molecules give rise to absorption bands, which are SWIR (0.7-2.7 μm), MWIR (3-5 μm), and LWIR (8-12 μm).

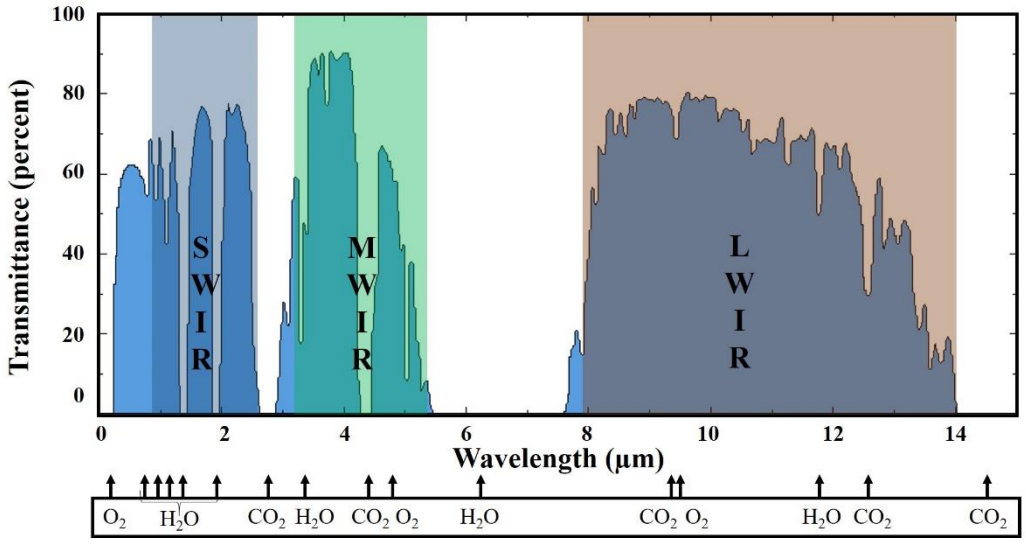

Figure 1.4. Atmospheric transmission of the EM spectrum (redrawn from ref. [8]).

The LWIR band range is generally used in long-range applications requiring high precision and high performance in cold weather conditions and in passive thermal imaging. Moreover, the LWIR wavelength can transmit through mist and smoke.

As seen in Figure 1.3, the peak exitance wavelength of objects at room temperature is around 10 μm, which is within the LWIR band. If the contrast is more important than the sensitivity, the MWIR band range is more appropriate, since the emitted flux from targets change more rapidly when the temperature of the target changes. Additionally, MWIR is more suitable for hot object detection. The SWIR band covers wavelengths between 0.7 to 2.7 μm of the IR spectrum. SWIR detection is not possible from a source at room temperature, which has a very low photon exitance in that region (Figure 1.3). It needs an extra source, like a laser or a natural source to allow detection by reflection.

1.3 Types of Infrared Detectors

As previously mentioned, IR detectors are classified into two types, as thermal and photon detectors, and these types will briefly be discussed here.

1.3.1 Thermal Detectors

In thermal detectors, the IR light source causes an increase in the temperature of the absorber. This increase is measured by a temperature-dependent mechanism, in which the IR light is converted into an electrical signal. A temperature increase caused by the radiation coming into the detector is expressed by the heat balance, as in Eq. [2]:

$$C_{th}\frac{d\Delta T}{dt} + G_{th}\Delta T = \varepsilon\phi \tag{1.7}$$

where, C_{th}, G_{th} and ε are the thermal capacitance, thermal conductance, and emissivity of the detector, respectively, and T is the constant temperature of a heat sink. In this case, when the optical signal Φ reaches the detector, it causes a temperature increase of ΔT.

The schematic representation of a simple thermal detector is shown in Figure 1.5.

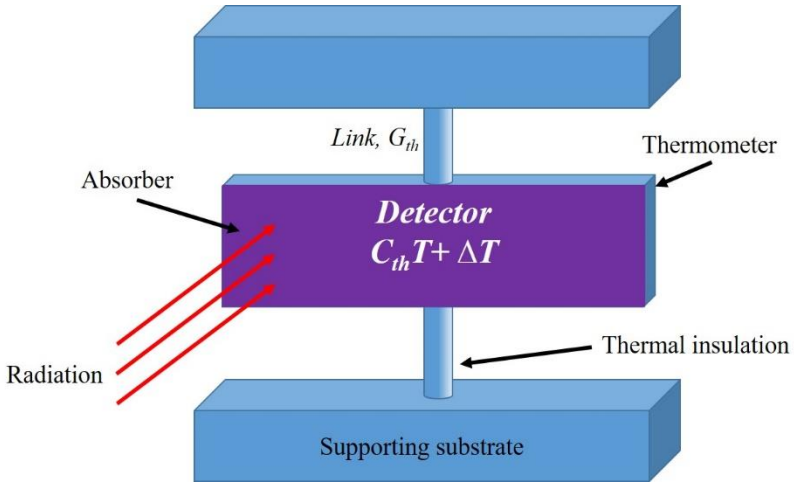

Figure 1.5. General representation of a thermal detector (redrawn from ref. [2]).

In general, an absorber is placed between two legs, which are linked to the heat sink. When light shines onto the absorber, a temperature change occurs. However, this change does not depend on the wavelength of the incident light; it only depends on the incident power of the light.

Thermopile: A thermopile is an IR detector type based on the Seebeck effect [2]. Thermopile is constructed by connecting several thermocouples. Basically, a thermocouple is composed of a junction of two metals with different conductivities, as shown in Figure 1.6. If the junction is heated, a potential difference occurs at the ends of these two different metals. A thermopile is the oldest IR sensor and has less sensitivity than other thermal detectors.

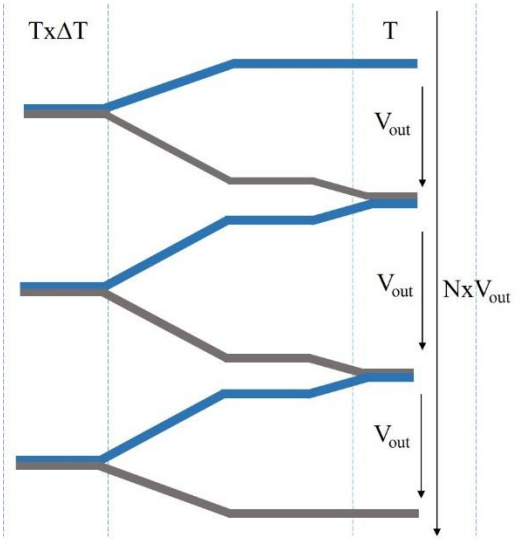

Figure 1.6. Schematic structure of a thermopile made of three thermocouples (redrawn from ref. [2]).

Bolometers: In the case of bolometer detectors, the light causes a resistance change in the absorber, and this change is converted into an electrical signal [2]. In this device, the absorber must have a small thermal capacitance and a large temperature coefficient for efficient detection. Unlike the thermopile, a bolometer needs a bias voltage.

Modern bolometer technology began in the early 1980s. The most widely used thermistor material is vanadium oxide (VOx). Nowadays, low-cost, large-area, monolithic two-dimensional (2D) focal plane arrays (FPAs) can be produced using silicon micromachining technology (Figure 1.7) [9].

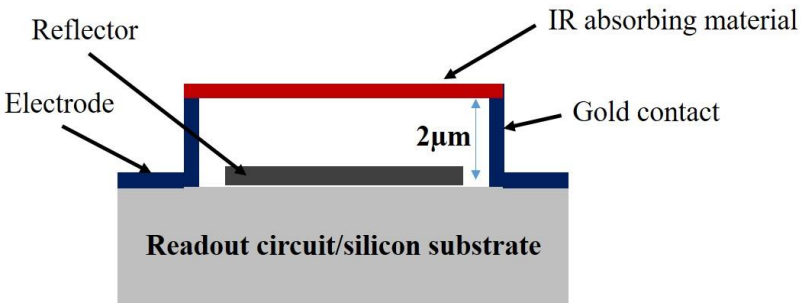

Figure 1.7. General representation of a Honeywell microbolometer (redrawn from ref. [2]).

Pyroelectric detectors: When a pyroelectric crystal is exposed to heat, the surface charges become polarized in one direction (Figure 1.8) [2]. If this temperature does not change, this asymmetry is compensated by the free charges. If, however, these temperature changes are faster than this compensating process, the asymmetry can be rearranged, and an electric signal can be measured.

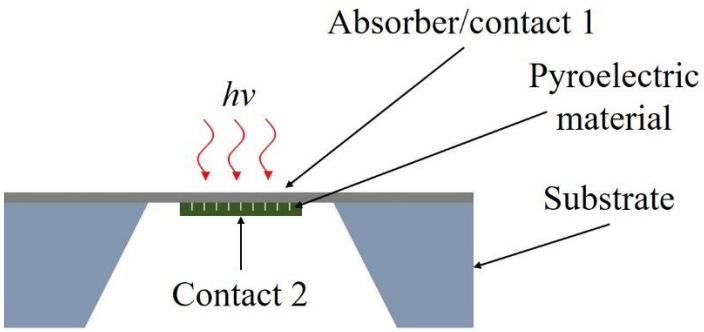

Figure 1.8. Schematic representation of a pyroelectric IR detector (redrawn from ref. [2]).

Therefore, compared to other thermal detectors, pyroelectric detectors measure change in temperature rather than temperature level.

1.3.2 Photon Detectors

In photon detectors, the light interacts with the electrons of the detector material, and it changes the electronic energy distribution [7]. The response of the photon detector per unit incident radiation power varies according to the wavelength absorbed by the detector. Although they have a very fast response and a good signal-to-noise (S/N) ratio, they usually need to be cooled, mostly for suppression of thermal generation [7]. There are many photon detector technologies, which can be listed as follows: photoconductor, photovoltaic (PV), unipolar barrier detectors, Schottky diode detectors, and low-dimensional IR detectors.

1.3.2.1 Photoconductive Detectors

In photoconductor detectors, light creates electron-hole pairs in the absorber, and these photogenerated charges increase the conductivity [2]. If voltage is applied, these photogenerated charges participate in the current, and the IR signal is measured. In general, photoconductor detectors are classified into two types, intrinsic and extrinsic.

Intrinsic photoconductive detectors: In intrinsic photoconductive detectors, the cutoff wavelength of the detector is determined by the bandgap of the absorber. The incoming photon excites electrons from the valence band to the conduction band, and free electron-hole pairs are generated. PbS, PbSe, PbSnTe, HgCdTe, InGaAs, InSb, InAs and InAsSb are common intrinsic photoconductive materials [2].

Extrinsic photoconductive detectors: In this type of detectors, a high-bandgap semiconductor absorber doped with impurities is used. The excitation occurs between the impurity level and the bottom of the conduction band, so the cutoff wavelength is determined by the energy difference of these two levels. Extrinsic detectors can be used in a very wide spectrum up to 300 μm. However, they are mostly preferred larger than 20 μm in applications [7]. Si:Ga, Ge:Hg, and Si:In are common extrinsic photoconductive materials [2].

1.3.2.2 Photovoltaic Detectors

PV detectors are usually formed by combining (metallurgical junction) two different types (n-type and p-type) of semiconductors. In the region of the junction, there are no free charge due to the generated electric field between fixed ions; therefore, it is called the depletion region. In PV detectors, photocurrent is created by photoelectrons and photoholes which are generated within the depletion region and within a distance as far as the diffusion length from the depletion region [2]. The strong electric field in the depletion region sweeps the photogenerated electrons into

n-type and holes into p-type regions; thus, photocurrent is generated [10] (Figure 1.9).

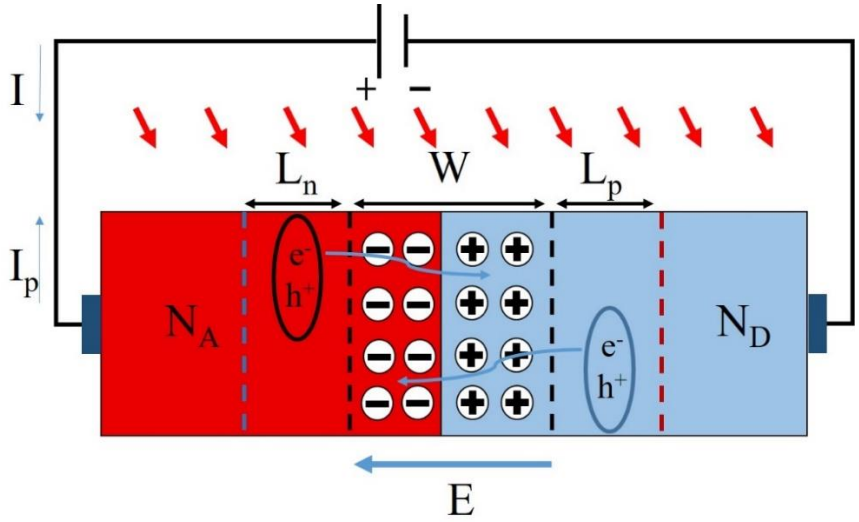

Figure 1.9. Schematic structure of a PV detector (redrawn from ref. [8]).

The photocurrent (I_p) produced by the PV detector is expressed as:

$$I_p = qAg_{op}(L_p + L_n + W) \tag{1.8}$$

where L_n, L_p, and W are the electron diffusion length in p-type material, hole diffusion length in n-type material, and depletion region of the pn junction. A, q, and g_{op} are the cross-section, electron charge, and optical generation rate. PV detectors will be discussed in more detail in the next chapter.

1.3.2.3 Barrier detectors

Barrier detectors are a relatively a new type photodetector that includes a high bandgap barrier material between the absorber and contact layers for blocking the majority carriers (e.g., electrons for n-type material), without demising the flow of the minority carriers (e.g., holes for n-type material) [11]. In the barrier-type detectors, the depletion region related and surface leakage dark current mechanisms can be suppressed, but there are some restrictions, such as finding appropriate barrier material and Fermi level alignment between the absorber and barrier material. In

Figure 1.10, pBn- and nBn-type barrier detectors are illustrated. Barrier detectors will be discussed in details in the third chapter.

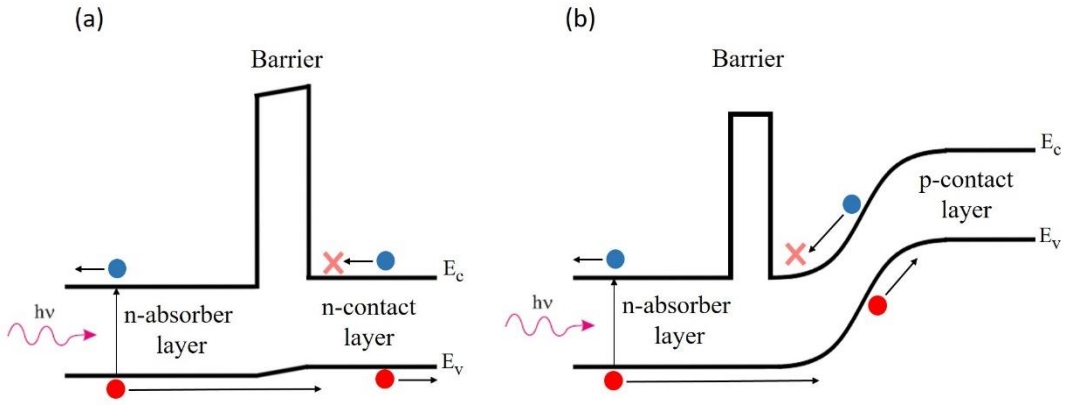

Figure 1.10. Illustrations of (a) nBn- and (b) nBp-type barrier detector is illustrated (redrawn from ref. [11]).

1.3.2.4 Schottky Diode Detectors

Such detectors are known as Schottky-barrier photoemissive detectors. The most well-known Schottky-barrier IR detector is PtSi. In this detector, IR radiation is absorbed in the metal. Hot holes (high kinetic-energy holes) are produced during the process. These hot holes are injected into the semiconductor by passing over the potential barrier, and the negative charge in the silicide is directly transferred into the charge-coupled device (CCD) (Figure 1.11) [2].

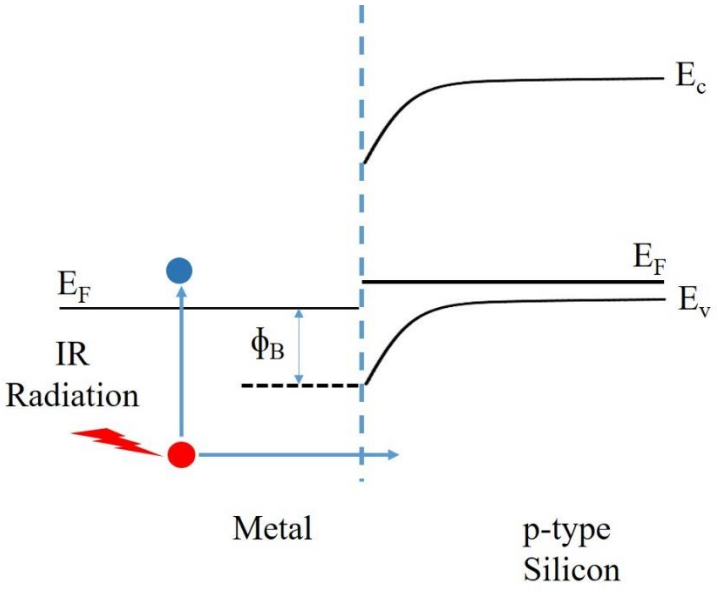

Figure 1.11. Band diagram of a Schottky diode IR detector (redrawn from ref. [12]).

1.3.2.5 Low Dimensional Detectors

Low-dimensional semiconductor was first proposed by Esaki and Tsu [13]. In the case of a low-dimensional semiconductor, when the dimensions of the material are reduced in quantum scales, the electronic and optical properties can be engineered depending on the size. The discovery of this feature led to the development of superlattice (type-I and type-II) and quantum dot IR photodetector (QDIP) detector technologies.

Type-I: Quantum well IR photodetectors (QWIPs) are Type-I superlattice detectors, which are low-band-gap semiconductor material sandwiched between two high-band-gap semiconductor materials as seen Figure 1.12. In QWIPs, the electron transition occurs between the sub-bands. QWIP materials are usually selected from the III-V group; the most well-known are InGaAs-InP [14] and AlGaAs-GaAs [15] material systems.

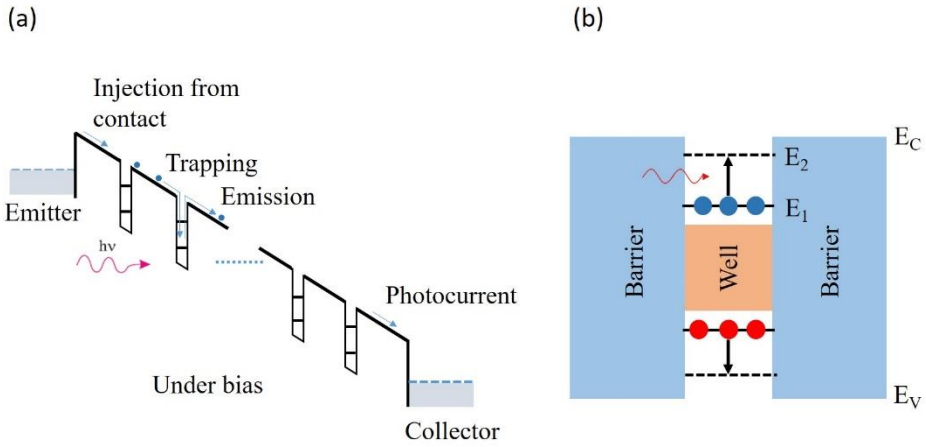

Figure 1.12. (a) Band structure of a QWIP IR detector and (b) band diagram of a single quantum well (redrawn from ref. [2] and [15]).

High-quality material, uniformity, fast response time, and long integration time are some of the important features of QWIPs. Additionally, QWIPs have low quantum efficiency.

Type-II: In type-II superlattice detectors, the quantum well structures in the periodic structure are so close to each other that the wave functions of the electrons in the quantum wells overlap, and this forms electron and hole minibands. The absorption wavelength is determined by the energy gap between these minibands (Figure 1.13). The most well-known type-II superlattice material systems are InSb-InAsSb, InAs-GaInSb, and InAs-GaSb [16], [17].

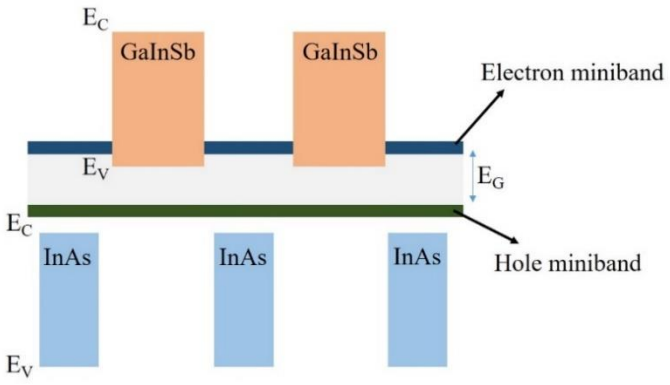

Figure 1.13. Band structure of a type-II superlattice IR detector (redrawn from ref. [17]).

1.4 The Contributions of This Thesis

Barrier detector architecture allows higher performance than conventional pn detector architecture. However, the applicability of this architecture is limited since suitable barrier materials are not easily found for all kinds of detector systems. Antimonite-based compound semiconductors (ABCS) (or 6.1Å III-V family materials) are the most suitable material system to obtain a barrier detector since type-II heterojunction structures can be designed with various alloy and superlattice materials. However, this type of barrier design is not suitable for InGaAs and HgCdTe material systems which are technologically mature, since these two detector materials form the type-I heterojunction structure. The main contribution of this thesis is to show that a barrier-type InGaAs and HgCdTe can be obtained using compositionally graded and delta-doped layers. The outcome was presented in the literature with the following studies:

For the InGaAs nBn detector, lattice-matched InAlAs and lattice-mismatched InGaAs used for barrier material:

- Uzgur, Fatih, et al. "All InGaAs unipolar barrier infrared detectors." IEEE Transactions on Electron Devices 65.4 (2018): 1397-1403.
- Uzgur, Fatih, et al. "Al/Sb free InGaAs unipolar barrier infrared detectors." Infrared Technology and Applications XLIII. Vol. 10177. International Society for Optics and Photonics, 2017.
- Uzgur, Fatih, and Serdar Kocaman. "InGaAs nBn SWIR detector design with lattice-matched InAlGaAs barrier." Turkish Journal of Electrical Engineering & Computer Sciences 27.1 (2019): 1-10.

At least 40 and 20 times dark current improvement for the lattice-matched and lattice-mismatched barrier nBn detectors, respectively, were numerically shown in the dark current level by suppressing surface leakage and generation-recombination (G-R) current mechanisms in the SWIR band, without compromising any photo-response when compared to the conventional pn junction.

In the case of HgCdTe material systems, strong suppression of G-R and trap-assisted tunneling (TAT) currents have been shown to be possible with the designed structures in SWIR, MWIR, and LWIR bands for the alternative substrate HgCdTe technology:

- Uzgur, Fatih, and Serdar Kocaman. "Barrier engineering for HgCdTe unipolar detectors on alternative substrates." Infrared Physics & Technology 97 (2019): 123-128.

A HgCdTe dual-band nBn detector configuration was also numerically examined in MWIR/LWIR bands using compositionally graded and delta-doped layers:

- Uzgur, Fatih, and Serdar Kocaman. "A dual-band HgCdTe nBn infrared detector design." Infrared Sensors, Devices, and Applications IX. Vol. 11129. International Society for Optics and Photonics, 2019.

Moreover, the method was applied successfully for obtaining an extended SWIR (eSWIR)/SWIR InGaAs dual-band nBn detector structure and the results were used for a project application by the TÜBİTAK 1001-Scientific and Technological Research Projects Funding Program, in a project named “Genişletilmiş SWIR Bölgesinde Çalışan Delta Katkılı nBn Yapısında Kızılötesi Dedektör”. This project was accepted and began in March 2019 under grant number TUBİTAK 118E771.

CHAPTER 2

DARK CURRENT MECHANISMS AND FIGURES OF MERIT

In this chapter, first, the dark current mechanisms will be explained through a pn junction detector before talking about the superiority of the nBn detector over the pn detector. Next, the dark current properties of the nBn detector will be mentioned briefly. Finally, the infrared detector performance parameters will be explained. An nBn-pn detector comparison will be discussed in more detail in the next chapter.

2.1 pn Infrared Photodetector (Photodiode)

A pn detector is obtained by combining n-type and p-type semiconductor materials to form a metallurgical junction. Due to the difference in the carrier concentrations, electrons in the n-type region and holes in the p-type region diffuse to the other regions simultaneously. With the diffusion of electrons and holes, an electric field is formed by the charged fixed dopant atoms that the electrons and holes leave behind in the junction region. The potential difference created by this electric field is called built-in potential (V_b). In addition, since the free charges will be swept away by the electric field, this region is also called the depletion region (Figure 2.1) [2].

If the energy of the incident photons on the detector is larger than the bandgap of the semiconductor absorber material, electron-hole pairs are generated in the absorber. If the electron-hole pairs are generated in the depletion region, or if the electron-hole pairs generated in the quasi-neutral region have the ability to reach the depletion region, the electric field sweeps electrons into the n-type region and holes into the p-type region. Thus, photocurrent is obtained without applying an external voltage from the detector, which is called the PV effect [2].

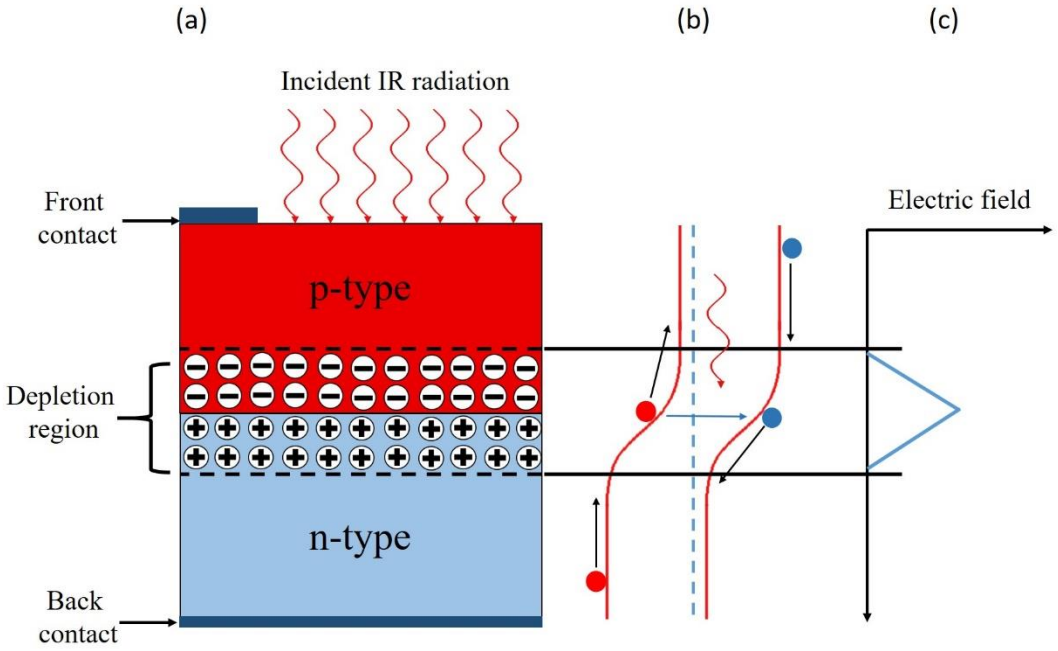

Figure 2.1. A simple pn junction IR detector; (a) detector pixel structure, (b) energy band diagram, and (c) electric field in depletion region (redrawn from ref. [2]).

The equivalent circuit of a pn detector is given in Figure 2.2. Here, R_s is a series resistor that is very small, C_d is the total capacitance, and R_L is the load resistance. C_a and R_a are the input capacitance and resistance of the amplifier.

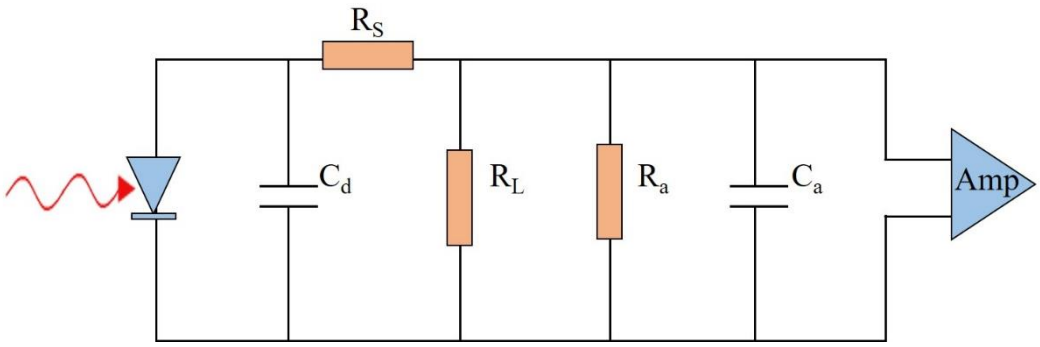

Figure 2.2. Equivalent circuit for an illuminated pn junction IR detector (redrawn from ref. [2]).

Dynamic resistance is one of the most crucial parameters affecting the performance of semiconductor IR detectors. In most applications, a small bias, at which dynamic resistance is maximum, is selected as the operating voltage [2]. The dynamic resistance of a pn junction is the slope of the its I-V characteristic at any point, expressed as:

$$R = \frac{dV}{dI}. \tag{2.1}$$

Low dynamic resistance increases Johnson noise as can be seen in the formula below:

$$i_{n,Johnson} = \sqrt{\frac{4kT\Delta f}{R}} \tag{2.2}$$

where R is the dynamic resistance. Moreover, high dynamic resistance is essential for high injection efficiency from an IR detector to silicon multiplexers [18].

The expression of the total current density of a pn junction photodetector is given as follows:

$$J(V, \Phi) = J_d(V) - J_p(\Phi) \tag{2.3}$$

where J_d is the dark current density and varies with the bias voltage, and J_p is the photocurrent density that depends on the photon flux density. The photocurrent I_p is given with the following equation:

$$I_p = J_p A_d = \eta q A_d \Phi \tag{2.4}$$

where η is the quantum efficiency, q is unit charge and A_d is the area of the detector. Photo and dark I-V characteristics for a pn junction IR detector are given in Figure 2.3.

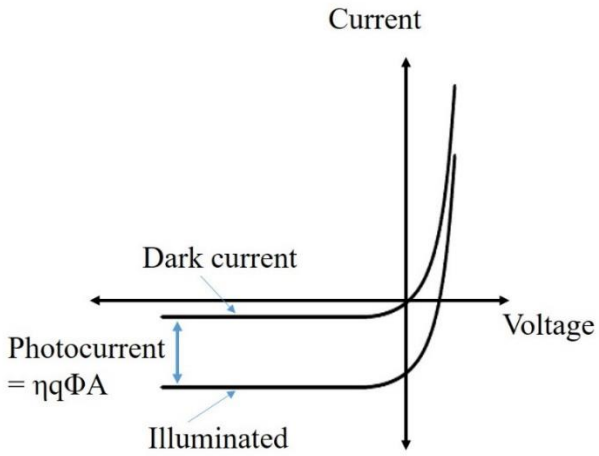

Figure 2.3. Photo and dark I-V characteristics for a pn junction IR detector (redrawn from ref. [2]).

Dark current mechanisms are the most critical parameters that impact IR detector performance. In section 2.1.1, dark current mechanisms will be discussed in detail.

2.1.1 Dark Current Mechanisms

2.1.1.1 Dark Current for an Ideal pn Junction

The equation that gives the dark current characteristic of an ideal pn junction photodetector is called the Shockley equation [8], [19], as given below:

$$I_d = I_s\left(e^{\frac{qV}{kT}} - 1\right) = qA_d\left(\frac{D_p}{L_p}p_n + \frac{D_n}{L_n}n_p\right)\left(e^{\frac{qV}{kT}} - 1\right) \tag{2.5}$$

$$L_p = \sqrt{D_p\tau_p}\ ,\ L_n = \sqrt{D_n\tau_n} \tag{2.6}$$

$$I_d = qA_d\left(\frac{L_p}{\tau_p}p_n + \frac{L_n}{\tau_n}n_p\right)\left(e^{\frac{qV}{kT}} - 1\right) \tag{2.7}$$

where I_s is the reverse saturation current, V is the applied voltage, k is the Boltzmann constant, T is the temperature of the detector, D_p and D_n are the minority carrier diffusion coefficients, L_p and L_n are the minority carrier diffusion lengths, p_n and n_p

are the minority carrier concentrations, and τ_p and τ_n are the minority carrier lifetimes for holes and electrons in the n-type and p-type regions, respectively. The Shockley equation for V<0 and |V|>> kT/q under reverse bias can be modified as follows:

$$I_d = -qA_d\left(\frac{L_p}{\tau_p}p_n + \frac{L_n}{\tau_n}n_p\right) = -qA_d\left(\frac{L_p}{\tau_p}\frac{n_i^2}{N_D} + \frac{L_n}{\tau_n}\frac{n_i^2}{N_A}\right) \tag{2.8}$$

$$p_n = \frac{n_i^2}{N_D} \quad , \quad n_p = \frac{n_i^2}{N_A} \tag{2.9}$$

where N_D is the donor doping density of the n-region, N_A is the acceptor doping density of the p-region, and n_i is intrinsic carrier concentration [19]:

$$n_i = 2\left(\frac{2\pi kT}{h^2}\right)^{3/2}\left(m_n^* m_p^*\right)^{3/4} e^{-E_g/2kT} . \tag{2.10}$$

The expression of n_i^2 which is given in the equation above leads to strong temperature dependency of the dark current. Therefore, the dark current of an ideal pn photodetector is determined only by the diffusion current that depends on the temperature. Such detectors are called diffusion-limited photodetectors [2].

2.1.1.2 Dark Current for a Real pn Junction

In reality, there are many dark current mechanisms in addition to the diffusion current for pn junction detectors. These dark current mechanisms originate from the native properties of semiconductor material or material defects, and the dark currents are also generated in the depletion region, in the quasi-neutral, or on the surface of the semiconductor [20].

The total dark current can be given as the sum of all dark current components, as shown below:

$$I_{DARK} = I_{DIFF} + I_{G-R} + I_{TAT} + I_{BTBT} + I_{SURFACE} . \tag{2.11}$$

Diffusion current (I_{DIFF}) is thermally produced by minority carrier generation in a neutral region. The G-R current (I_{G-R}) occurs in the depletion region through the Shockley-Read-Hall (SRH) mechanism via impurity or trap states. The TAT current (I_{TAT}) is another trap-aided and depletion region related dark current mechanism. Here, electrons in the valence band pass into the conduction band via traps in the depletion region aided by tunneling and thermal excitation. In the band-to-band tunneling (BTBT) current (I_{BTBT}), the electrons tunnel directly from the valence band to the conduction band through the depletion region (Figure 2.4). Surface leakage current ($I_{SURFACE}$) occurs because the dangling bonds on the crystal surface act like traps. Additionally, these traps can cause Fermi level pinning on the surface.

In the following sections, the dark current mechanisms mentioned above will be discussed in more detail.

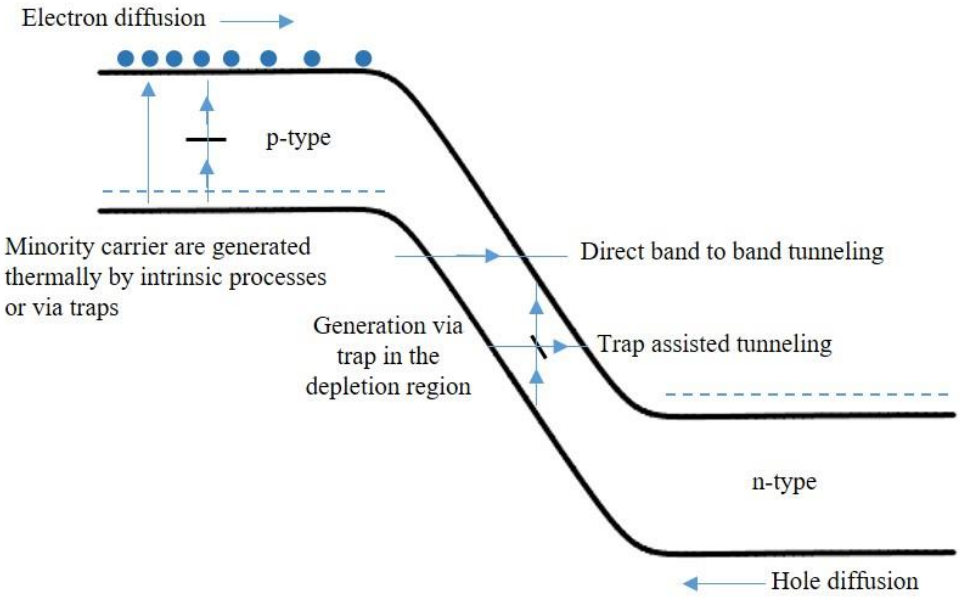

Figure 2.4. Schematic representation of the band diagram of a reverse biased pn junction diode (redrawn from ref. [2]).

2.1.1.2.1 Diffusion Current

Diffusion current (I_{diff}) is caused by thermally generated minority carriers through SRH, Auger, and radiative mechanisms in a quasi-neutral region for narrow-bandgap semiconductors. Here, the minority carrier lifetime is determined by the dominant generation-recombination mechanism in the same region [21], [22].

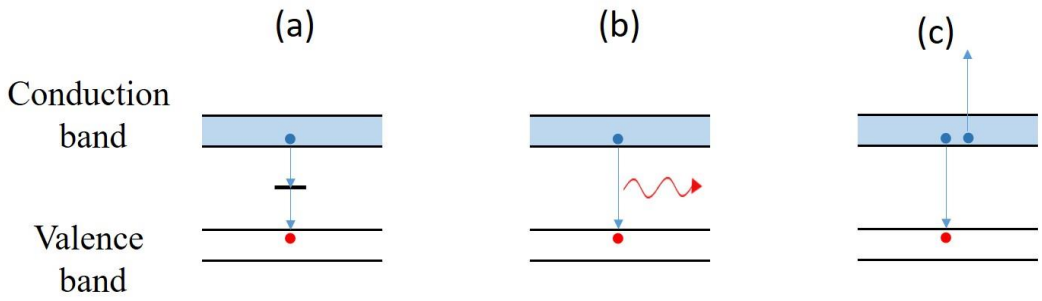

Figure 2.5. Generation-recombination mechanisms; (a) SRH, (b) Radiative, and (c) Auger (redrawn from ref. [23]).

SRH process occurs via trap-induced trap states in the bandgap (Figure 2.5 (a)). Radiative recombination is an intrinsic mechanism that takes place when free electrons and holes in conduction and valence bands recombine, resulting in photon emissions (Figure 2.5 (b)). Auger recombination is an intrinsic mechanism that involves three particles. Excess energy resulting from Auger recombination is transferred to the third particle (Figure 2.5 (c)).

These three recombination mechanisms will be discussed in detail in the following sections.

2.1.1.2.2 Shockley-Read-Hall Mechanism

The SRH generation-recombination (G-R) mechanism takes place via the thermal effect through the levels (G-R center) within the forbidden energy band-gap, and it is not intrinsic. G-R levels are caused by native defects or residual impurities, which comprise dislocations, grain boundaries, interstitial impurities, substitutional

impurities, and vacancies in the crystal semiconductor material. In this process, excess energy is emitted as a phonon [21], [22]. The SRH mechanism determines the quality of the IR detector material. In detectors with high crystal purity, the SRH lifetime is higher [23].

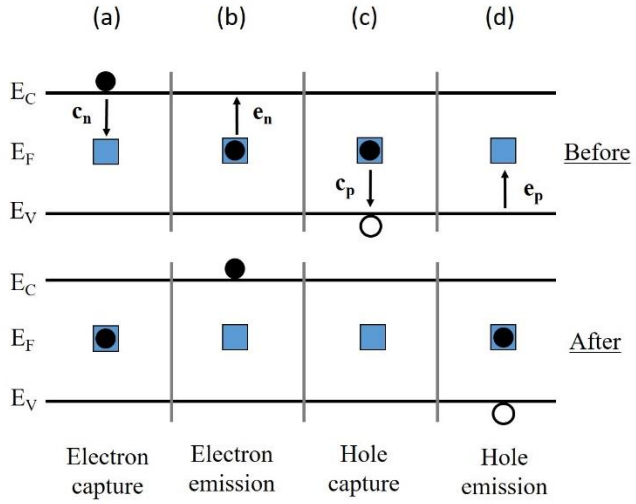

Figure 2.6. SRH processes via G-R centers (redrawn from ref. [24]).

There are four types of SRH mechanisms, as can be seen in Figure 2.6: (a) the electron in the conduction band can be captured by the GR center, (b) the electron can be excited from the GR center to the conduction band, (c) the electron in the G-R center can annihilate the hole in the valence band, and (d) the electron in the valence band can be excited to the G-R center, causing hole emission in the valence band [25].

The net SRH recombination rate R_{net}^{SRH} ($cm^{-3}s^{-1}$) is determined by the G-R center trap density N_t (cm^{-3}), electron and hole capture cross-section areas σ_n and σ_p (cm^2), conduction and valence band carrier concentrations n and p, G-R center energy level E_T and carrier thermal velocity v_{th} (cm/s), as in Eq. (2.12) below:

$$R_{net}^{SRH} = \frac{\sigma_n \sigma_n v_{th}(n_0 p_0 - np)N_t}{\sigma_n(n + n_1) + \sigma_p(p + p_1)} \tag{2.12}$$

where n_1 and p_1 are the carrier concentrations for the Fermi level corresponding to the G-R trap level [23]. Here, n_1 and p_1 are given by:

$$n_1 = N_C e^{\frac{-E_T}{kT}} \tag{2.13}$$

$$p_1 = N_V e^{-\frac{(E_G - E_T)}{kT}} \tag{2.14}$$

where, N_c and N_v are the effective density of the states at the conduction and valence bands (cm^{-3}). The simplified version of the net SRH recombination rate can be expressed as:

$$R_{net}^{SRH} = \frac{np - n_i^2}{\tau_{n0}(n + n_1) + \tau_{p0}(p + p_1)}, \tag{2.15}$$

$$R_{net}^{SRH} = \frac{(n_0 + \Delta n)(p_0 + \Delta p) - n_i^2}{\tau_{p0}(n_0 + \Delta n + n_1) + \tau_{n0}(p_0 + \Delta p + p_1)}, \tag{2.16}$$

$$R_{net}^{SRH} = \frac{(n_0 + p_0 + \Delta n)\Delta n}{\tau_{p0}(n_0 + \Delta n + n_1) + \tau_{n0}(p_0 + \Delta p + p_1)}. \tag{2.17}$$

SRH lifetime can be expressed as:

$$\tau_{SRH} = \frac{\tau_{p0}(n_0 + \Delta n + n_1) + \tau_{n0}(p_0 + \Delta n + p_1)}{(n_0 + p_0 + \Delta n)} \tag{2.18}$$

In the case of low carrier injection ($\Delta n << n_0$ or $\Delta p << p_0$), assuming that $E_T=E_F$ then $n_1=p_1=n_i$ (n_0 and p_0 are the electron and hole equilibrium concentrations (cm^{-3}) for the n-type and p-type semiconductors, [8], [26]), as shown below:

$$R = \frac{\Delta p}{\tau_{p0}}, \qquad for\ an\ n-type\ semiconductor \tag{2.19}$$

$$R = \frac{\Delta n}{\tau_{n0}}, \qquad for\ a\ p-type\ semiconductor \tag{2.20}$$

where Δn and Δp are excess electron and hole concentrations (n= n_0+Δn, p= p_0+Δp).

The hole minority carrier lifetime (τ_{p0}) for an n-type semiconductor material is expressed as:

$$\tau_{p0} = \frac{1}{\sigma_p v_{th} N_t} \tag{2.21}$$

while the electron minority carrier lifetime (τ_{n0}) for a p-type semiconductor material is expressed by:

$$\tau_{n0} = \frac{1}{\sigma_n v_{th} N_t} \ . \tag{2.22}$$

Due to the nature of the bulk crystal structure, the periodicity terminates on the surface with incomplete bonds. These incomplete bonds form SRH trap levels within the bandgap [26].

The surface SRH rate ($cm^{-2}s^{-1}$) can be expressed as below [27]:

$$R_{net}^{SRH\ surf} = \frac{np - n_i^2}{(n + n_1)/_{S_p} + (p + p_1)/_{S_n}}, \tag{2.23}$$

$$s_n = \sigma_n v_{th} N_{t\ (suface)}\ , \tag{2.24}$$

$$s_p = \sigma_p v_{th} N_{t\ (suface)}\ , \tag{2.25}$$

$$n_1 = N_C e^{\frac{-E_{Tsurf}}{kT}}\ , \tag{2.26}$$

$$p_1 = N_V e^{-\frac{(E_G - E_{Tsurf})}{kT}}\ , \tag{2.27}$$

where s_n and s_p are the surface recombination velocities (cm/s), and $N_{t(surface)}$ is the surface trap (acceptor or donor like) density (cm^{-2}).

2.1.1.2.3 Radiative mechanism

Radiative recombination occurs when free electrons and holes in the conduction and valence bands recombine, resulting in photon emission (Figure 2.7). This mechanism is an intrinsic mechanism, since it is determined by the electronic band structure of the semiconductor material. Radiative recombination usually takes place in direct bandgap semiconductor materials [26].

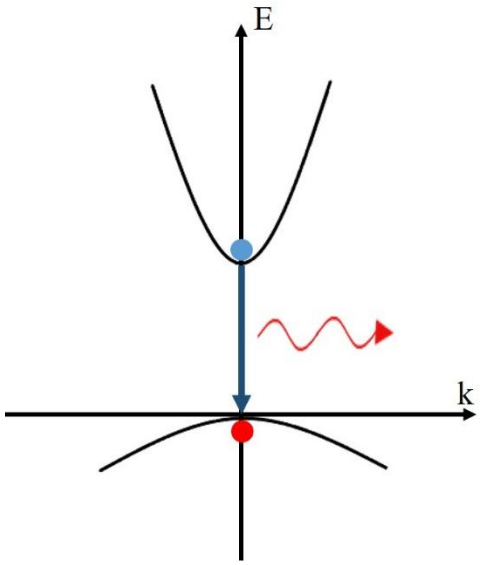

Figure 2.7. Radiative recombination mechanism (redrawn from ref. [26]).

The radiative recombination rate ($cm^{-3}s^{-1}$) depends on the carrier and intrinsic carrier concentrations of a semiconductor material [28], as shown below:

$$R_{net}^{rad} = B(np - n_i^2) \tag{2.28}$$

$$R_{net}^{rad} = B((n_0 + \Delta n)(p_0 + \Delta p) - n_i^2) \tag{2.29}$$

$$R_{net}^{rad} = B(n_0\Delta n + p_0\Delta n + \Delta n^2)\,, \qquad (\Delta n = \Delta p) \tag{2.30}$$

The radiative recombination lifetime is given as:

$$\tau_{rad} = \frac{1}{B(n_0 + p_0 + \Delta n)}, \tag{2.31}$$

where B ($cm^{-3}s^{-1}$) is called the radiative recombination coefficient and is expressed as follows [18]:

$$B = 5.8 \times 10^{-13}\sqrt{\varepsilon_\infty}\left(\frac{m_0}{m_e + m_{hh}}\right)^{\frac{3}{2}}\left(1 + \frac{m_0}{m_e} + \frac{m_0}{m_{hh}}\right)\left(\frac{300}{T}\right)^{\frac{3}{2}} \cdot \left(E_g^2 + 3k_BTE_g + 3.75\,(k_BT)^2\right) \tag{2.32}$$

where ε_∞ is the static dielectric constant, m_e and m_{hh} are the electron and hole effective masses and m_0 is the mass of the electron.

For the n-type material in the case of low-level injection ($\Delta n \rightarrow 0$) [29],

$$\tau_{rad(li)} = \frac{1}{Bn_0} \tag{2.33}$$

and in the case of high-level injection,

$$\tau_{rad(hi)} = \frac{1}{B\Delta n}. \tag{2.34}$$

The absorber immediately reabsorbs photons emitted as a result of radiative recombination. Moreover, in a detector array, any detector can absorb photons emitted by other detectors or from a passive element [2].

2.1.1.2.4 Auger Mechanisms

Auger recombination is an intrinsic mechanism that involves three particles. This mechanism generally occurs at low temperatures in low and direct bandgap semiconductor materials. In this process, an electron in the conduction band (C)

recombines with a hole in the heavy-hole band (H), and the resulting excess energy is transferred to a third particle. The third particle, which is called auger carrier, is an electron in the conduction band or a hole in the valence band that releases excess energy into the lattice as a phonon or as heat [26].

Depending on the type of Auger carrier and where it is generated, the Auger recombination mechanism is divided into three types (Figure 2.8) [26].

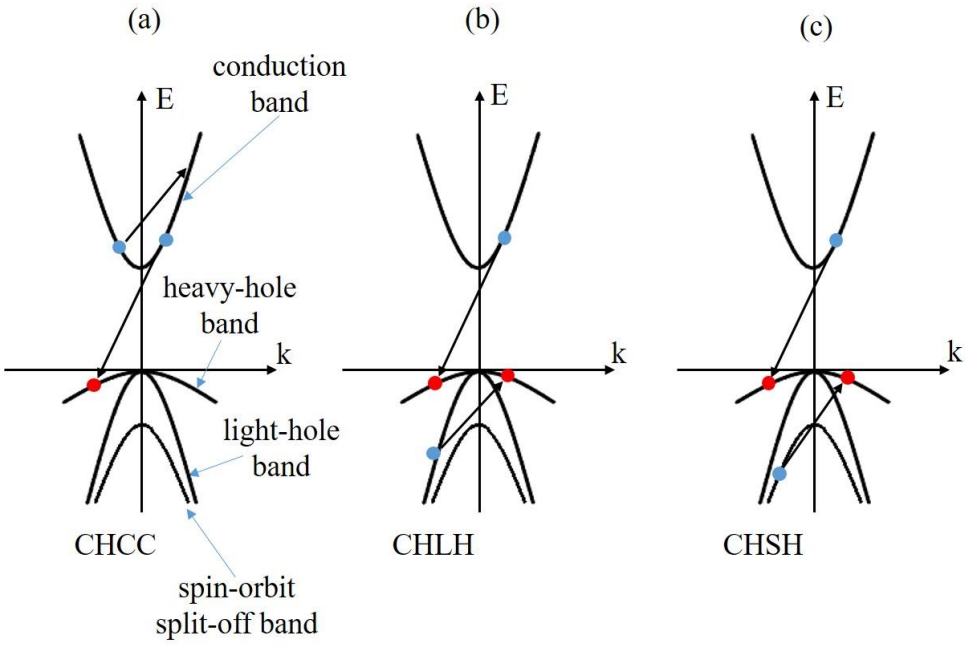

Figure 2.8. Auger recombination mechanisms: (a) Auger 1 process, (b) Auger 7 process, (c) Auger S process (redrawn from ref. [26]).

The first process is called Auger 1 or CHCC (Figure 2.8 (a)). In this process, the excess energy is transferred to an electron in the conduction band (C), and then the electron is excited to a higher state in the conduction band (C). Since this process requires two electrons in the conduction band and a hole in the valence band, Auger 1 is dominant in n-type semiconductor materials [23]. The second process is called Auger 7 or CHLH (Figure 2.8 (b)). In this process, the excess energy is transferred to an electron in the light hole band (L). In this situation, the electron is excited to a vacancy state in the heavy-hole band (H) [26]. Auger 7 process is more dominant in

p-type semiconductor materials, since it consists of an electron and two holes [23]. The last one is called Auger S or CHSH (Figure 2.8 (c)). In this process, the excess energy is transferred to an electron in the split of the band (S). In this case, the electron is exited to an empty state in the heavy-hole band (H). More generally, the Auger S process occurs when the Eg approaches the ΔE (spin-orbit splitting) (for example, InAs, InAsSb). The total Auger recombination rate ($cm^{-3}s^{-1}$) can be expressed as:

$$R_{total}^{auger} = G_{A1}(pn^2 - nn_i^2) + G_{A7}(np^2 - pn_i^2)\,, \tag{2.35}$$

$$G_{A1} = \frac{1}{2n_i^2\tau_{A1}^i} = \left[2n_i^2 \frac{3.8\times10^{-18}\varepsilon_s^2\left(1+\frac{m_e^*}{m_h^*}\right)^{0.5}\left(1+2\frac{m_e^*}{m_h^*}\right)}{m_e^*|F_1F_2|^2\left(\frac{kT}{E_G}\right)^{1.5}} \times \exp\left(\frac{1+2\frac{m_e^*}{m_h^*}\frac{E_G}{kT}}{1+\frac{m_e^*}{m_h^*}}\right)\right]^{-1}, \tag{2.36}$$

$$G_{A7} = \frac{1}{2n_i^2\tau_{A7}^i} = G_{A1}\left[\frac{\gamma'\left(1-\frac{5E_G}{4kT}\right)}{1-\frac{3E_G}{2kT}}\right]^{-1}, \tag{2.37}$$

$$\frac{\tau_{A7}^i}{\tau_{A1}^i} = \frac{\gamma'\left(1-\frac{5E_G}{4kT}\right)}{1-\frac{3E_G}{2kT}} = \gamma\,, \tag{2.38}$$

where E_G (eV) is the energy band-gap, m_e^* and m_h^* are the electron and hole effective masses, n_i (cm^{-3}) is the intrinsic carrier concentration, ε_s is the relative static dielectric constant, τ^i_{A1} and τ^i_{A7} are the intrinsic lifetime for Auger 1 and Auger 7, γ

is the fitting parameter, and $|F_1F_2|$ is the overlap integral [24]. Auger lifetimes for under low injection conditions are expressed as:

$$\tau_{A1} = \frac{2\tau_{A1}^{i} n_i^2}{n(n+p)}\ , \quad \text{for n} - \text{type material,} \tag{2.39}$$

$$\tau_{A7} = \frac{2\tau_{A7}^{i} n_i^2}{p(n+p)}\ , \text{for p} - \text{type material.} \tag{2.40}$$

2.1.1.2.5 Recombination lifetime

The bulk carrier lifetime can be defined as:

$$\frac{1}{\tau_{bulk}} = \frac{1}{\tau_{srh}} + \frac{1}{\tau_{rad}} + \frac{1}{\tau_{Auger}}. \tag{2.41}$$

The carrier lifetimes for n-type material can be written as [29], [30]:

$$\tau_{srh}^{-1} = \frac{n_0 + \Delta n}{\tau_{p0}(n_0 + \Delta n) + \tau_{n0}(\Delta n)}, \tag{2.42}$$

$$\tau_{rad}^{-1} = B(n_0 + \Delta n)\ , \tag{2.43}$$

$$\tau_{Auger\,1}^{-1} = C_n(n_0 + \Delta n)^2,\ C_n = G_{A1}\ . \tag{2.44}$$

thus, the total carrier lifetime for the n-type material is defined as follows:

$$\tau_{bulk}^{-1} = \frac{n_0 + \Delta n}{\tau_{p0}(n_0 + \Delta n) + \tau_{n0}(\Delta n)} + B(n_0 + \Delta n) + C_n(n_0 + \Delta n)^2\ . \tag{2.45}$$

In case of low injection ($\Delta n \rightarrow 0$), the minority carrier lifetime can be simplified as [30]:

$$\tau_{MC}^{-1} = \tau_{p_0}^{-1} + Bn_0 + C_n n_0^2 \tag{2.46}$$

where τ_{p0} is the hole minority carrier lifetime, B is the radiative recombination coefficient, and C_n is the Auger 1 recombination coefficient.

Effective lifetime for a semiconductor material can be given as:

$$\frac{1}{\tau_{eff}} = \frac{1}{\tau_{bulk}} + \frac{1}{\tau_{surf}} = \left(\frac{1}{\tau_{srh}} + \frac{1}{\tau_{rad}} + \frac{1}{\tau_{Auger}}\right) + \frac{1}{\tau_{surf}}. \tag{2.47}$$

Surface recombination lifetime can be given as [31]:

$$\frac{1}{\tau_{surf}} = \left(\frac{W}{2S} + \frac{1}{D_n}\left(\frac{W}{\pi}\right)^2\right)^{-1}, \tag{2.48}$$

where; W (cm) is the width of a sample, S (cm/s) is the surface recombination velocity, and D_n (cm^2/s) is the diffusion constant.

2.1.1.3 G-R Dark Current

One of the dark current components is the G-R current, which is generated in the depletion region (space-charge region) through the SRH mechanism via impurity or trap states. Since the Fermi level passes through midgap in the depletion region, the thermal activation energy is equal to half of the bandgap (Figure 2.9). In addition to this, the electron-hole pair generated in the depletion region is swept into quasi-neutral regions due to the strong electric field. Thus, the SRH rate is more significant in the depletion region than in the quasi-neutral regions [32], [33].

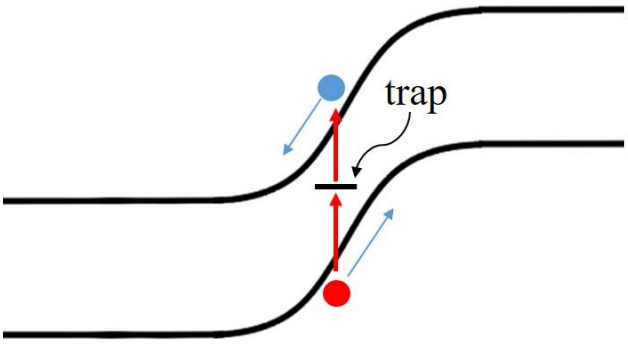

Figure 2.9. G-R dark current mechanism (redrawn from ref. [20]).

In the case of a reverse biased pn junction detector, there is no minority carrier injection into the depletion region. From the SRH rate expression in Eq. (2.15), the net SRH rate for the depletion region can be given as:

$$R_{net}^{SRH} = \frac{-n_i^2}{\tau_{n0}(n_i) + \tau_{p0}(n_i)} = \frac{-n_i}{2\tau} = -G\,, \tag{2.49}$$

where, $E_T = E_i$, $\tau_{n0} = \tau_{p0} = \tau$ and $n, p << n_i$ (for the depletion region).

In reverse bias, the G-R current can be expressed as:

$$I = qG_{dep}V_{dep} = q\frac{n_i W_{dep}}{2\tau}A \tag{2.50}$$

where V_{dep} is the volume of the depletion region, W_{dep} is the thickness of the depletion region, A is the area of the pn junction and τ is the minority carrier lifetime due to the SRH process.

The width of the depletion region can be defined as [2]:

$$W_{dep} = \sqrt{\frac{2\varepsilon_0\varepsilon_r(N_d + N_a)(V_{bi} \pm V)}{qN_dN_a}}\,, \tag{2.51}$$

where N_d and N_a are the donor and acceptor doping densities (cm^{-3}), V is the applied bias voltage and V_{bi} is the built-in potential which is expressed as:

$$V_{bi} = \left(\frac{kT}{q}\right) ln\left(\frac{N_a N_d}{n_i^2}\right) \tag{2.52}$$

As seen above, the G-R current roughly varies with the square root of the applied bias voltage ($V^{1/2}$) since the width of the depletion region changes with the applied voltage in the case of an abrupt junction. For a linearly graded junction, the G-R current changes with the $V^{1/3}$ [2].

When the G-R and diffusion currents are compared to their temperature dependence, the G-R changes proportional to n_i. Therefore, it is less affected by the variation in the temperature. When the temperature is lowered to suppress the dark current, the diffusion current drops faster; thus, the G-R current becomes more effective than the diffusion current at low temperatures.

2.1.1.4 Trap Assisted Tunneling Dark Current

Another trap-aided dark current mechanism is the TAT dark current. In this mechanism, trap levels in and around the depletion region are effective. Here, in the tunneling process, an electron is thermally excited from the valence band to the trap level, and then it tunnels from this level to the conduction band, or the electron is excited from the valence band by tunneling to the trap level, and then from there, it is thermally excited to the conduction band (Figure 2.10). The effect of the TAT current increases as the quality of the pn junction diode material decreases [2].

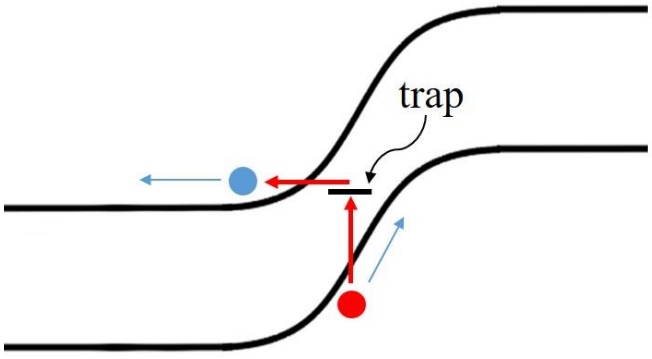

Figure 2.10. TAT dark current mechanism (redrawn from ref. [20]).

The TAT dark current mechanism strongly depends on the energy bandgap and doping level of the semiconductor material. It is not relatively dependent on the temperature and varies exponentially with the electric field. Therefore, the TAT current is generally effective in low bandgap materials (especially LWIR and very LWIR (VLWIR) bands), and at low temperatures, where diffusion and G-R currents are suppressed [2].

The TAT current is expressed as follows:

$$I_{TAT} = qN_t wA\left(\frac{1}{\gamma_p p_1 + \omega_v N_v} + \frac{1}{\omega_c N_c}\right)^{-1}, \tag{2.53}$$

where γ_p and N_t are the hole recombination coefficient and density for the trap center, w and A are the depletion region width and detector area, w_v is the carrier tunneling probability between the trap center and the valence band, w_c is the carrier tunneling probability between the trap center and the conduction band, and N_c and N_v are the effective density of the state of conduction and valence band.

In the case of $w_c N_c << \gamma_p p_1$ and $w_c N_c \sim w_v N_v$, the TAT current can be simplified as,

$$I_{TAT} = qN_t wA\omega_c N_c\,, \tag{2.54}$$

$$\omega_c N_c = \frac{\pi^2 q m^* E M^2}{h^3(E_g - E_t)} exp\left[-\frac{(m^*/2)^{1/2} E_g^{3/2} F(a)}{2qE\hbar}\right], \tag{2.55}$$

$$a = 2\left(\frac{E_t}{E_g}\right) - 1\,, \qquad F(a) = \left(\frac{\pi}{2}\right) - a\left(1 - a^{1/2}\right)^{1/2} - \left(\frac{1}{\sin a}\right)\,, \tag{2.56}$$

where *E* is a uniform electric field (V/cm), M is the matrix element related to trap potential, $w_c N_c$ is the tunneling rate, which is corresponding to from a neutral trap center to the conduction band, and m^* is the effective mass.

As it can be seen from the above equations, as effective mass decreases, the tunneling increases. Therefore, tunneling most probably occurs between the light hole band and the trap level [2].

2.1.1.5 Band to Band Tunneling (BTBT) Dark Current

BTBT dark current occurs by direct tunneling of the electron through the valence band to the conduction band along the junction (Figure2.11). In contrast to G-R and TAT currents, the BTBT dark current is an intrinsic mechanism, since it is not caused by traps. The BTBT dark current is more effective in the case of reverse biased and low bandgap pn junction diodes, which are heavily doped on both sides [2], [8].

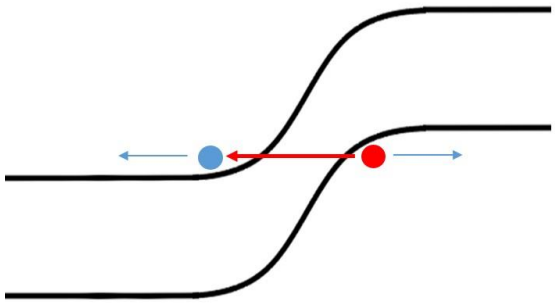

Figure 2.11. BTBT dark current mechanism (redrawn from ref. [20]).

Assuming that the potential barrier is triangular [2], then:

$$I_{BTBT} = AJ_{BTBT} = A\frac{q^2EV_b}{4\pi^2\hbar^2}\left(\frac{2m^*}{E_g}\right)^{1/2} exp\left[-\frac{4(2m^*)^{1/2}E_g^{3/2}}{3q\hbar E}\right], \qquad (2.57)$$

where V_b is the applied bias voltage, m^* is the electron effective mass, E_g is the energy bandgap of semiconductor material (eV) and E is the electric field (V/cm) in the pn junction, which can be given as:

$$E = \left[\frac{2q}{\varepsilon_0\varepsilon_s}\left(\frac{E_g}{q} \pm V_b\right)\frac{np}{n+p}\right]^{1/2}. \qquad (2.58)$$

As can be seen from the above equations, the BTBT dark current strongly depends on the band-gap of the pn junction diode materials, doping concentrations, and applied voltage [2].

2.1.1.6 Surface Leakage Dark Current

Another mechanism that affects the performance of IR detectors is the surface leakage dark current. As previously mentioned, dangling bonds on the surface of the crystal act as SRH trap states. Moreover, these traps can act as donors or acceptors and cause Fermi level pinning on the surface of the material regardless of the bulk doping type. Hence, majority carrier drift, diffusion, tunneling, and G-R dark currents flow on the surface of the semiconductor device [2], [33]. Therefore, surface passivation material is applied to stabilize the surface of the semiconductor devices.

2.2 Dark Current Mechanisms of an nBn Detector

An nBn detector epilayer consists of an n-type absorber, an n-type contact layer and a high bandgap unipolar barrier inserted between them. Since there is no depletion region and valence band offset in this structure, dark current mechanisms such as G-R, TAT, BTBT and surface leakage current can be suppressed without degrading the photocurrent (Figure 2.12). Since the depletion region generated dark current mechanisms are suppressed, the nBn detector dark current is limited by diffusion current that is generated in the absorber region, even under elevated trap concentration conditions [21].

As mentioned above, diffusion dark current based on the minority carrier-lifetime is determined by the dominant G-R processes in the quasi-neutral region. These processes comprise SRH, radiative, and Auger mechanisms for narrow-bandgap semiconductors.

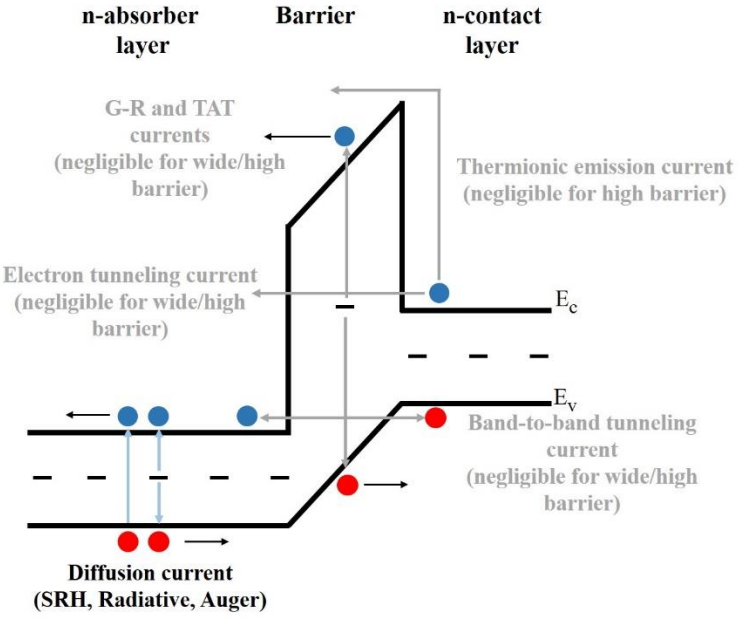

Figure 2.12. An nBn detector band structure (redrawn from ref. [34]).

The diffusion current for the nBn detector can be given as [21]:

$$I_d = qA_d \frac{n_i^2 L_{diff}}{\tau_{mc} N_D} \tanh\left(L_{abs}/L_{diff}\right), \tag{2.59}$$

$$\tanh\left(L_{abs}/L_{diff}\right) \approx \left(L_{abs}/L_{diff}\right), \tag{2.60}$$

$$I_d = qA_d \frac{n_i^2 L_{abs}}{\tau_{mc} N_D}, \tag{2.61}$$

where L_{dif} is the minority carrier diffusion length, L_{dif} is the thickness of the absorbing region, N_{donor} is the donor density, and τ_{mc} is the minority carrier lifetime.

As seen in Eq. (2.61), the dark current of the nBn detector only changes by n_i^2, so the temperature dependence of the nBn detector is stronger than that of the pn detector. Figure 2.13 shows the dark current responses of the pn and nBn detectors according to temperature changes [35].

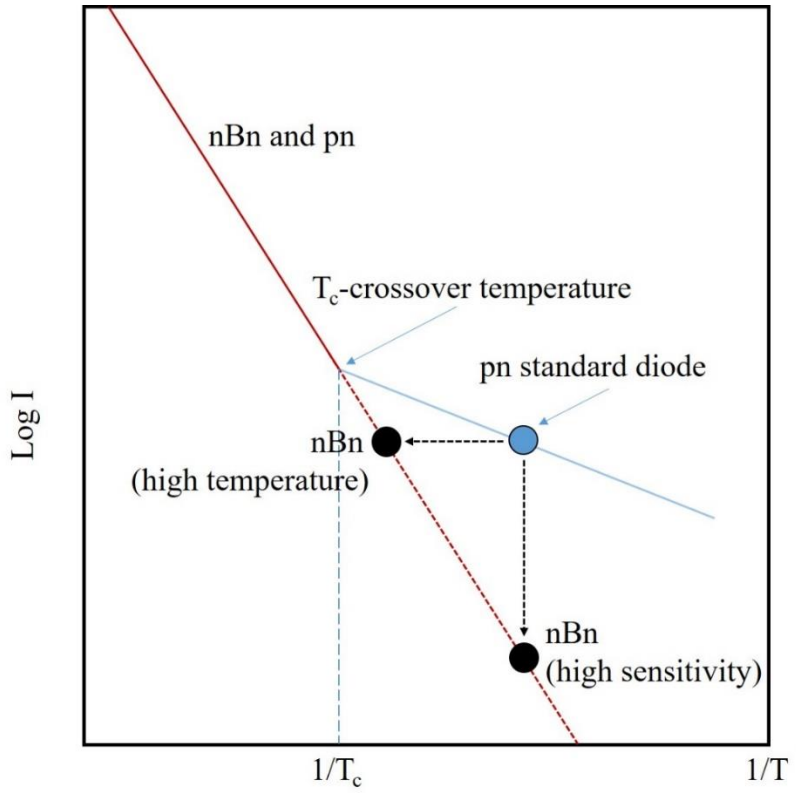

Figure 2.13. Schematic representation of a dark current Arrhenius plot for pn and nBn detectors (redrawn from ref. [35]).

As seen in Figure 2.13, at high temperatures, the dark currents of the pn and nBn detectors change in the same way as the temperature does. This is because the diffusion current is dominant at high temperatures and varies with $T^3\exp(-E_{g0}/kT)$. As the temperature decreases, the dark current of the nBn detector decreases as well, while the dark current of the pn detector decreases more slowly because the G-R current starts to dominate due to the depletion region. Here, the dark current changes with $T^{3/2}\exp(-E_{g0}/2kT)$ in the pn detector after a T_c critical temperature [35]. As is understood from the figure, the nBn detector can give lower dark current at the same temperature as the pn detector or give the same performance at higher temperatures [35].

2.3 Figures of Merit for Infrared Photon Detectors

The parameters that determine the performance of an IR detector will be mentioned below.

2.3.1 Responsivity

The ratio of the signal generated by the detector to the power of the incoming radiation is called responsivity which can be express as:

$$R = \frac{signal\ output}{E.A}, \tag{2.62}$$

where, the signal output can be output current (ampere) or voltage (volt), E is the incidence (W/cm^2), A is the detector area (cm^2).

The spectral responsivity of an ideal detector is given in Figure 2.14, where if the wavelength of incident light is smaller than the cutoff wavelength, the number of photons in 1 Watt radiation decreases, so that the responsivity decreases [8].

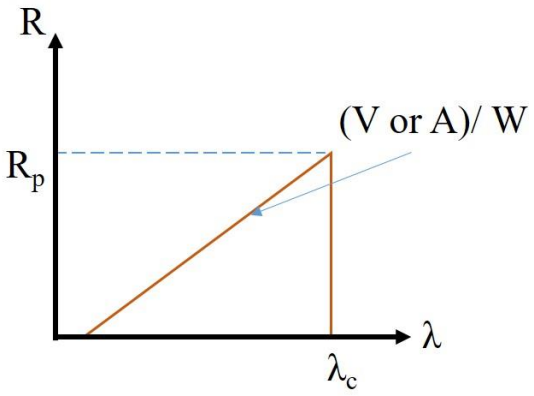

Figure 2.14. Ideal infrared detector spectral responsivity (redrawn from ref. [8]).

Spectral responsivity can be calculated utilizing wavelength and quantum efficiency using Eq. (2.63):

$$R = \eta \times \frac{q\lambda}{hc}. \tag{2.63}$$

When referring to the responsivity of a detector, blackbody responsivity (BR) and peak responsivity measurements are given. BR is a responsivity of the detector exposed to blackbody radiation at a certain temperature, and peak responsivity (R_p) is the highest responsivity at a certain wavelength.

2.3.2 Noise

The noise that reduces the performance of the detectors is a random oscillation in the output signal of the detector. Although it cannot be completely eliminated, it can be suppressed at a certain level. Johnson noise, 1/f noise, G-R, and shot noise are important types of noise components for IR detectors [36].

Johnson (Thermal or Nyquist) Noise: In a material, the thermally-assisted motion of electrons causes a noise which is called Johnson (Thermal or Nyquist) noise [36]. Thermal noise can be expressed in terms of current or voltage:

$$v_{n,Johnson} = \sqrt{4kTR\Delta f}\,, \tag{2.64}$$

$$i_{n,Johnson} = \sqrt{\frac{4kT\Delta f}{R}}\,, \tag{2.65}$$

where R is the resistance of a resistive material, k is the Boltzmann constant, and Δf is the bandwidth. A bias voltage is not needed for the occurrence of thermal noise.

Shot Noise: Shot noise, which is a minimum noise level for a detector, is driven by the discrete nature of detected photons. Shot noise appears in the biased PV detector. Shot noise current is given by this equation:

$$i_n = \sqrt{2qI\Delta f}\ , \tag{2.66}$$

where q is electron charge, Δf is the frequency bandwidth, and I is the average current flowing in the device [36].

Generation-Recombination Noise: G-R noise occurs by the random G-R of free carriers in semiconductor detectors that do not have a potential barrier, such as photoconductors. G-R noise is expressed by:

$$i_n = \sqrt{4qIg\Delta f}\ , \tag{2.67}$$

where q is electron charge, Δf is the frequency bandwidth, I is the current flowing in the device, and g is the gain of the IR detector. G-R noise can be caused by thermal or optical generation [8], [36].

In very low dark current situations, the performance of the IR detector is limited by background radiation, and these types of detectors are called background-limited performance (BLIP) detectors. The G-R noise of a BLIP detector can be expressed by [8]:

$$i_n = \sqrt{4qI_{photo}g\Delta f} \tag{2.68}$$

where the photocurrent is expressed by:

$$I_{photo} = q\eta g\phi_p A \tag{2.69}$$

where A is the cross sectional device area, g is the gain and φ_p is the photon flux density.

1/f (Pink) Noise: Although 1/f noise appears in many semiconductor electronic systems, its physical mechanism is not yet fully understood [9]. It occurs on potential barriers such as semiconductor surfaces and in non-ohmic contacts. If PV detectors are operated in open-circuit voltage mode, 1/f noise can be eliminated in these detectors [36] .

Noise Equivalent Power (NEP): Responsivity is an important parameter for detectors, but since the noise is not considered, responsivity does not give full information about performance. Therefore, the S/N ratio, which is the most important parameter for determining the performance of a detector, must be regarded [36].

NEP is the radiation power received by the detector in the case of S/N = 1.

NEP is given by:

$$NEP = \frac{(\phi) received\ power}{S/N} = \frac{v_{noise}}{R_v} = \frac{i_{noise}}{R_i}, \tag{2.70}$$

where v_{noise} is the noise voltage, i_{noise} is the noise current, and R_v and R_i are the voltage and current responsivity.

Detectivity (D): Detectivity is described 1/NEP:

$$D = \frac{1}{NEP} = \frac{S/N}{(\phi)_{received\ power}}. \tag{2.71}$$

However, since the detectivity depends on the noise measurement bandwidth and detector area, the performance comparison of the detectors cannot be done correctly. Therefore, the specific detectivity (D*), which is independent of these parameters, is defined by [8], [36]:

$$D^* = \frac{R_i\sqrt{A\Delta f}}{i_n} = \frac{R_v\sqrt{A\Delta f}}{v_n} \quad cmHz^{1/2}W^{-1} \tag{2.72}$$

For BLIP conditions, the specific detectivity is expressed by:

$$D^*_{BLIP} = \frac{\lambda}{2hc}\sqrt{\frac{\eta}{\phi_p}}. \tag{2.73}$$

CHAPTER 3

BARRIER INFRARED DETECTORS

Suppressing the dark current mechanisms is a crucial point for reaching higher performance and higher operating temperature conditions for IR detectors. Over the last few decades, barrier-type detectors have been proposed as a way to decrease dark current mechanisms.

A barrier-type detector was first proposed by A.M. White in 1983 [37]. It was then realized by the work of S. Maimon and G. Wicks [38]. Basically, the barrier detector is obtained by placing a high bandgap semiconductor material into the detector structure, and preventing the flow of the majority charge carriers, but allowing minority charge carriers to flow. These types of detectors are also called unipolar barrier IR detectors since they allow only one type of carrier to flow.

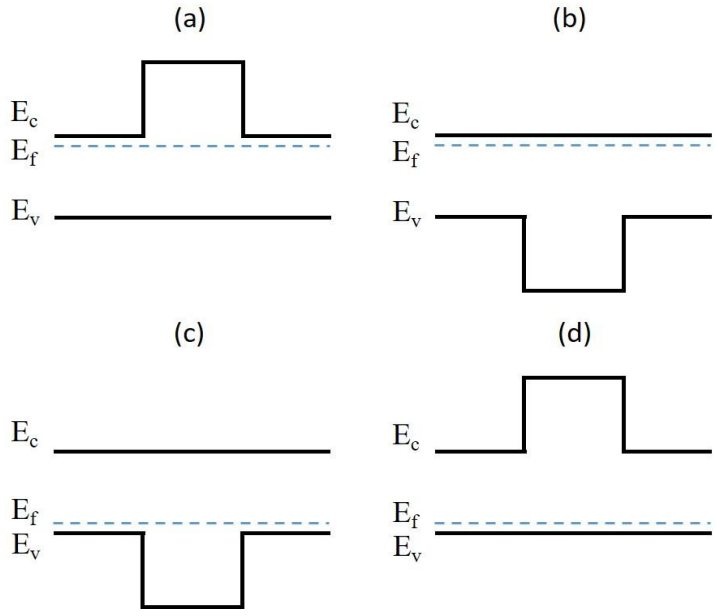

Figure 3.1. Types of unipolar barriers (redrawn from ref. [39]).

Since the majority carriers for n-type material are electrons, the barrier must be in the conduction band, as seen in Figure 3.1 (a). Otherwise, the barrier in the valence band blocks the minority carriers (Figure 3.1 (b)). If the semiconductor material is p-type, the barrier should be in the valence band (Figure. 3.1 (c)), if not, the conduction band barrier (Figure 3.1 (d)) blocks the flow of p-type minority carriers. If the unipolar barrier is properly placed in the pn detector structure (pBn), dark current mechanisms, such as G-R, TAT, BTBT and surface leakage currents, can be suppressed without degrading the photocurrent. Moreover, the barrier detector structure, in which both contact layers are the same type, can be obtained (nBn or pBp). Theoretically, since this detector structure does not have a depletion region, dark currents originating from the depletion region, such as G-R, TAT and BTBT currents, are not generated and the surface leakage current can be prevented without degrading the photocurrent through the barrier. As mentioned above, since the dark current components can be effectively suppressed in the unipolar barrier detector, the cooling requirement is reduced, and the detector can be operated at higher temperatures, or the detector can give lower dark current than pn detectors at low temperatures [35], [41]–[70].

3.1 pBn Photodiode Detector

This detector structure is called a barrier photodiode. In this structure, there are two different configurations according to the location of the unipolar barrier. The first is the structure in which the barrier layer is located between the n-type layer and the junction region. The second configuration is achieved by placing the barrier layer between the p-type layer and the junction region. Since the barrier in both configurations is only in the conduction band (zero valence band offset), only electron flow (the majority carrier for n-type material) is blocked. However, the effect of the barrier on the dark current changes according to its position and height in the detector. If the barrier is on the n-type material side and if it is sufficiently high, it can suppress G-R, TAT, BTBT and surface leakage currents (Figure 3.2).

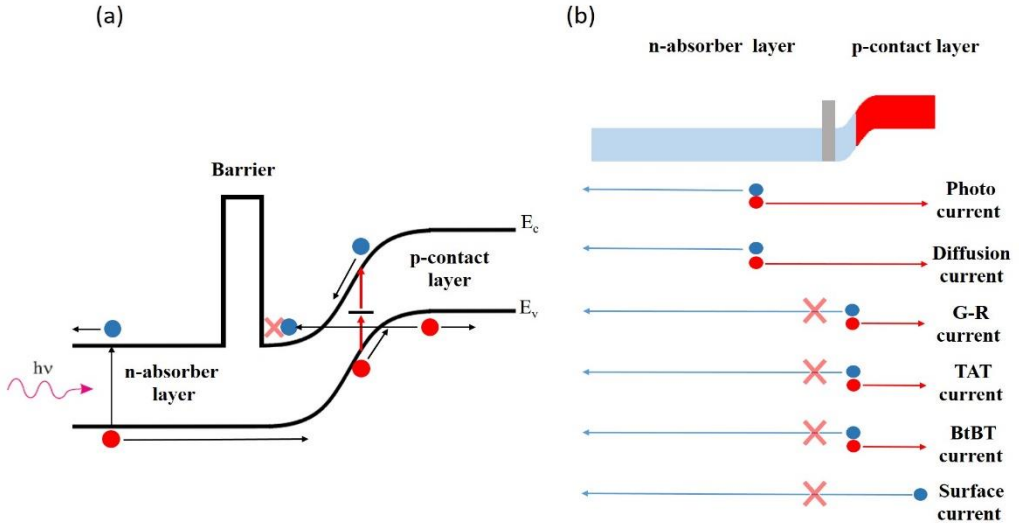

Figure 3.2. Spatial representation of (a) the pBn (barrier in the n-layer) detector band diagram (redrawn from ref. [35]) and (b) charge carriers formed in the detector.

In the case where the barrier layer is located in the p-type region (Figure 3.3), G-R, TAT, and BTBT currents cannot be suppressed, only the leakage current between the contacts can be suppressed.

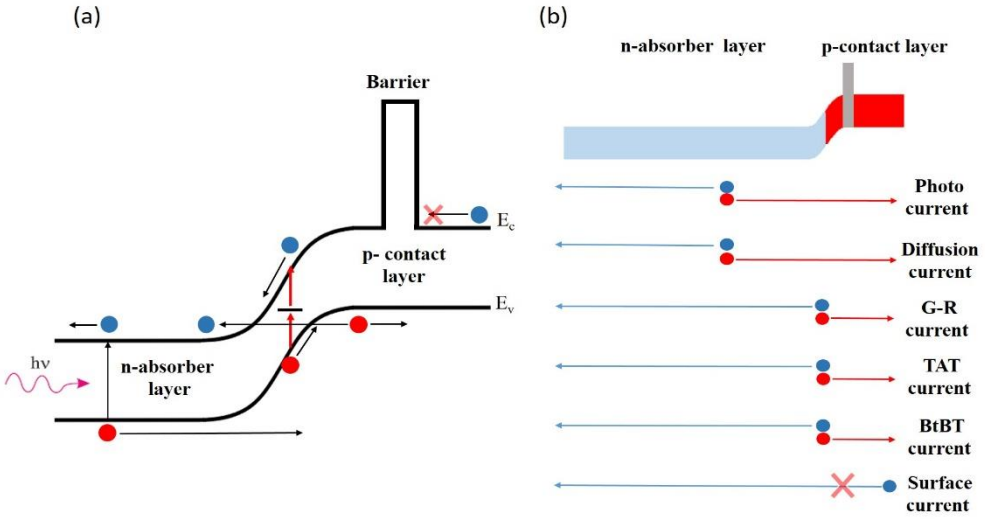

Figure 3.3. Spatial representation of (a) the pBn (barrier in the p-layer) detector band diagram (redrawn from ref. [35]) and (b) charge carriers formed in the detector.

3.2 nBn Photodetector

This detector structure basically consists of an n-type absorber layer, a high bandgap barrier layer, and n-type contact layer. Since there is no depletion region in this structure, there is no PV effect, like in photoconductor detectors. On the other hand, the gain is 1, like in PDs, because the flow of the majority carriers is blocked in the nBn detector (Figure 3.4).

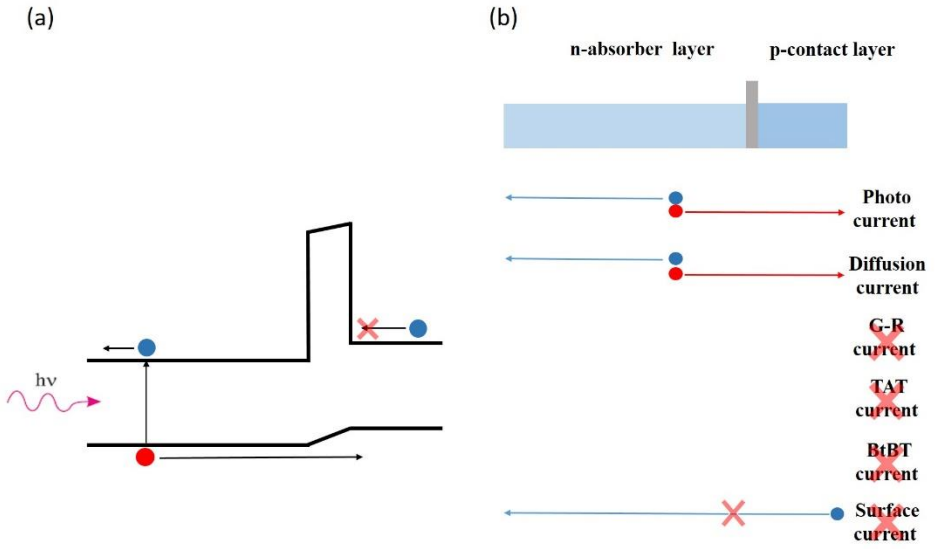

Figure 3.4. (a) nBn detector band diagram and (redrawn from ref. [35]) (b) spatial representation of carriers formed in the detector.

Ideally, the biggest difference between the nBn detector structure and the pn detector is that nBn detector does not have a junction area with a high electric field. In this case, G-R, TAT and BTBT dark current mechanisms in the detector almost do not arise, and the surface leakage current is blocked by the barrier layer. Due to these features, the nBn type detector structure provides a significant advantage in terms of dark current when compared to the pn detector structure [35]. In addition, the nBn architecture can be designed as a dual-band detector because minority carriers can flow, and the majority carries are blocked in both polarity situations.

3.3 General Configurations for Barrier Detectors

The most common configurations for barrier detectors were expressed by Klipstein as XB_nn and XB_pp and are called bariode detectors [62].

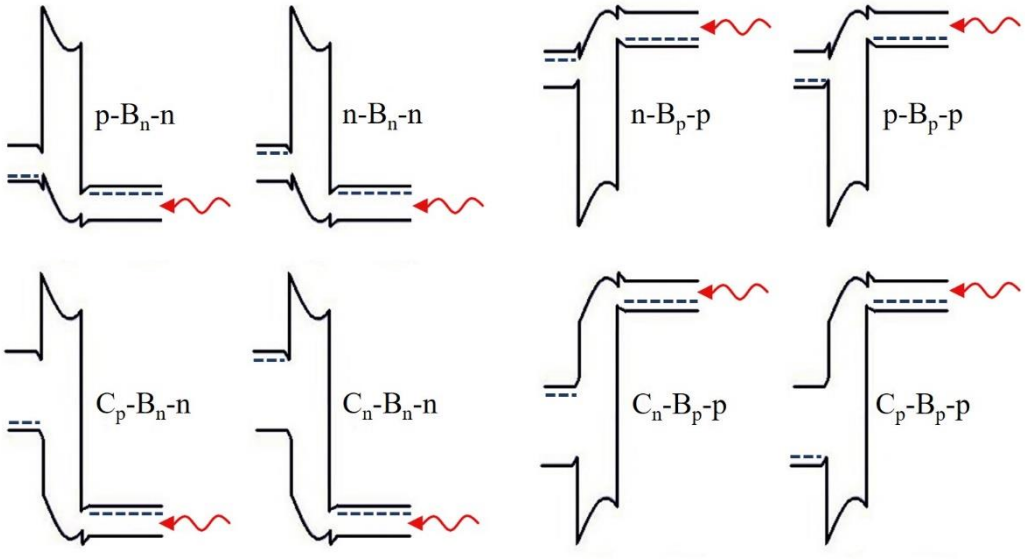

Figure 3.5. Band diagrams of biased barrier detectors for different layer configurations (redrawn from ref. [57]).

Here, X is the contact layer and it can have different doping types and band-gaps (C_p, C_n, n, p) from the absorber. In barrier detectors, if the contact layer and absorber layer have different doping types, the barrier should only prevent the flow of the majority carriers of the absorber material and allow the minority carriers. Moreover, the barrier should be in contact with the absorber to prevent the majority carriers from being produced in the depletion region. If the contact layer has the same doping type as the absorber layer, the barrier layer should only block the majority carriers, and allow the minority carriers to flow. Ideally, the barrier layer should have the same doping type as the absorber. An InAsSb (λ_c ~ 4.1 μm) detector with an AlSbAs barrier layer can be given as an example for an XB_nn, detector, and an InAs/GaSb T2SL (λ_c ~ 9.5 μm) detector with an InAs/AlSb staggered T2SL barrier can be given as an example of an XB_pp detector [58].

3.3.1 Barrier Detectors Limitations

The barrier detector architecture shows higher performance than the conventional pn detector architecture. However, the applicability of this architecture is limited since suitable barrier materials are not easily found for all kinds of detector systems. Ideally, Fermi levels of barrier and absorber layers are expected to be pre-aligned so that a charge transfer across the junction and depletion layer formation is prevented [42], [59] . The barrier should be thick enough to prevent tunneling, and high enough to prevent thermionic emission.

Moreover, the barrier, absorber and contact layers should be lattice-matched. However, these conditions are only possible to be applied in ABCS (or 6.1Å III-V family materials) [35]. Band offsets between antimony-based alloys (binary, ternary and quaternary compounds) materials allow for obtaining bulk barrier detectors and superlattice barrier detectors in various configurations (Figure 3.6) [35], [67], [68].

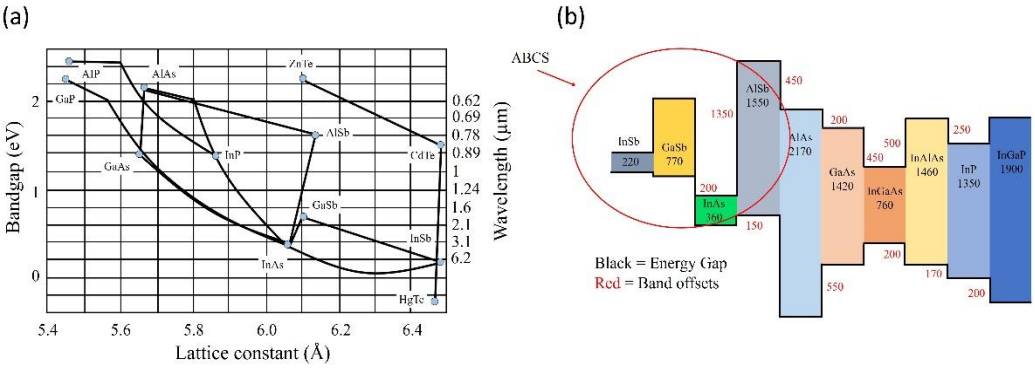

Figure 3.6. (a) Energy gap vs. lattice constant for III-V semiconductors, (b) relative positions of the band offsets of III-V semiconductors (redrawn from ref. [69] and [67]).

3.4 First Studies for Barrier Infrared Detectors

In the first nBn detector, which was fabricated by S. Maimona and G. W. Wicks [38], InAs material (3.4 μm cutoff) was used for the n-type absorber and contact layer. The un-doped $AlAs_{1-x}Sb_x$ (x □ 0.15) material, which was lattice-matched with InAs, was used as barrier material (100 nm) to obtain a zero-valence band offset nBn detector (Figure 3.7). Here, the barrier layer was thick enough to not cause tunneling and high enough to not cause thermionic emission. In their study, it was shown that the G-R and surface leakage current were successfully suppressed by using nBn architecture [38].

G. W. Wicks et al. showed that $AlAs_{1-x}Sb_x$ gave a zero-valence band offset with InAs when the x mole ratio was in the range of $0.14 < x < 0.17$ for the barrier material [70].

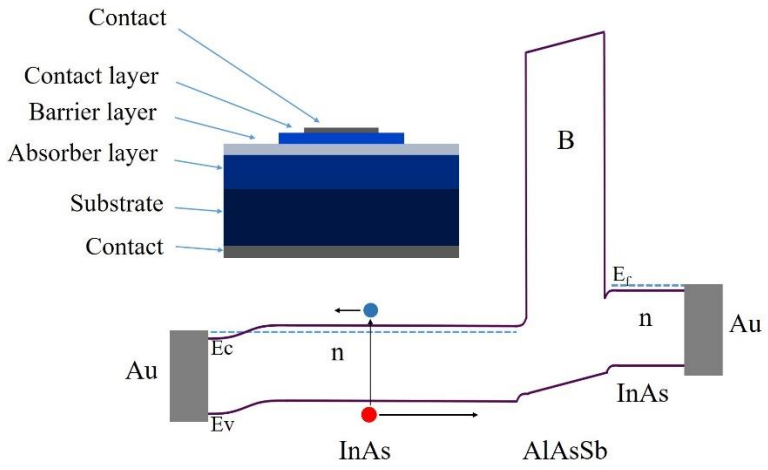

Figure 3.7. Schematic representation of InAs nBn detector pixel and band structure where the barrier material is lattice-matched AlAsSb (redrawn from ref. [70]).

J. B. Rodriguez et al. fabricated the first superlattice base nBn detector [71]. In their study, a type-II InAs/GaSb strained layer superlattice material system was used as the absorber (5.2 μm cutoff) and $Al_{0.4}GaSb$ alloy was used as the barrier material, with a barrier thickness of 50 nm (Figure 3.8). The contact layer was also made of superlattice material as the absorber. Although the superlattice layer was lattice-matched with the substrate, the barrier layer was not lattice-matched. In their study,

the valence band offset was not zero. However, it was not high enough to prevent the flow of holes. All layers of the detector had un-intentionally doping. In this case, although the carrier concentration of the n layers at room temperature was 10^{16} cm^{-3}, the barrier layer acted as slightly p-type.

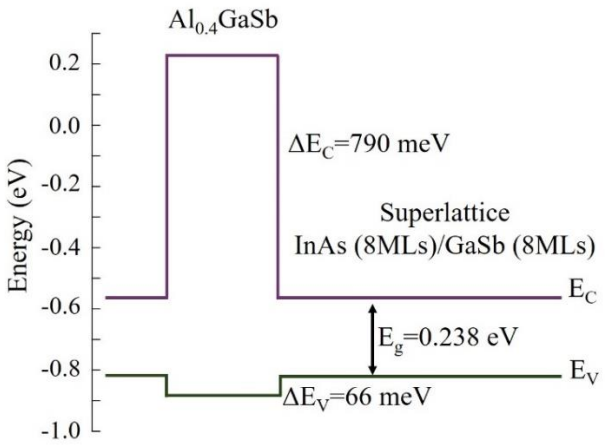

Figure 3.8. Schematic representation of superlattice based nBn detector band diagram (redrawn from ref. [71]).

Binh-Minh Nguyen et al. obtained an nB_pp-type detector by placing a high bandgap superlattice structure called M-structure in the p-π-n superlattice PD structure to form a valence band barrier [72].

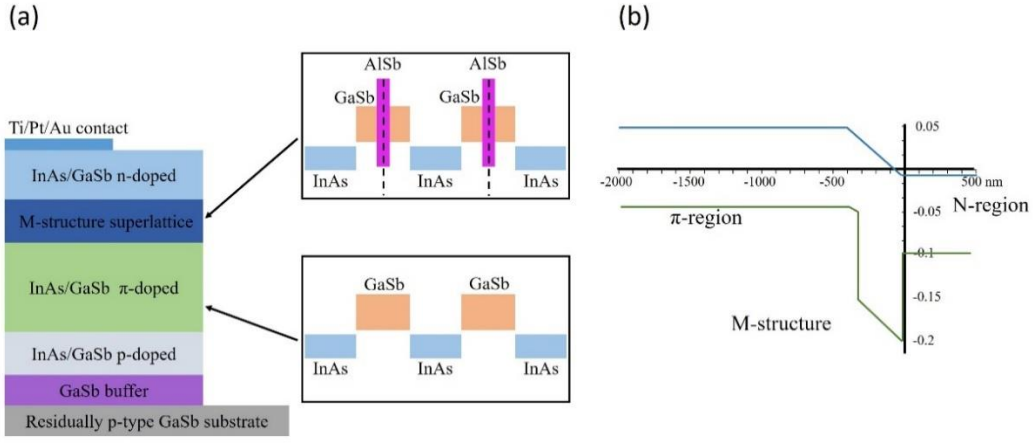

Figure 3.9. (a) Pixel structure of the type-II M-structured barrier superlattice detector, and (b) schematic representation of the band diagram (redrawn from ref. [72]).

In this structure, the cutoff wavelength of the type-II InAs/GaSb superlattice material, which is the absorber layer, is 10.5 μm, while the cutoff wavelength of the M-structure superlattice barrier layer is 6 μm. The M-structure superlattice barrier layer was obtained with the AlSb/GaSb/InAs/GaSb/AlSb periodic material system (Figure 3.9). Since the band alignment of this structure was obtained by inserting AlSb between the GaSb layers in a type-II InAs/GaSb superlattice structure in a manner similar to the M shape, it is called M-structured type-II superlattice (Figure 3.9 (b)).

The barrier detector with both electron and hole unipolar barrier was first produced in 2009 by David Z. Ting et al. [63]. The layer structure of this detector, called complementary barrier IR detector (CBIRD), consists of an InAs/GaSb SL absorber, InAs/AlSb SL hole barrier (hB), InAs/GaSb SL electron barrier (eB) and InAsSb bottom contact layers, where hB also acts as a top contact layer (Figure 3.10). In this structure, absorber and eB layers are p-type doped, hB and bottom contact layers are n-type doped.

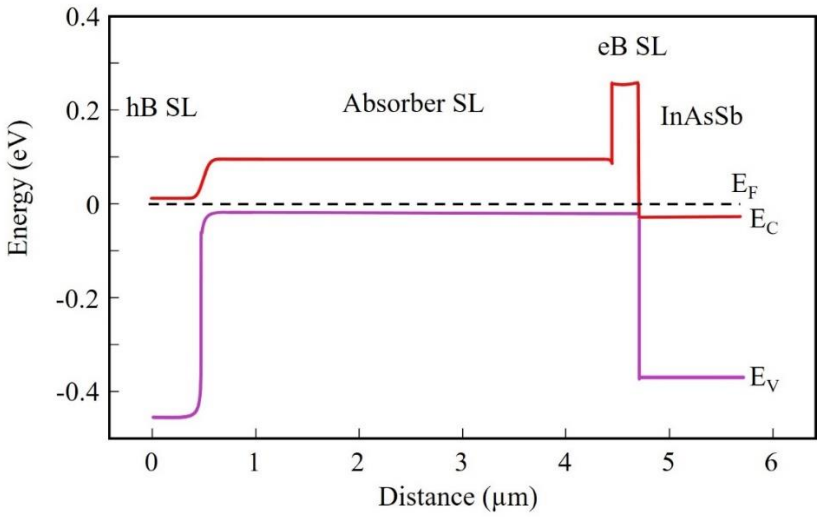

Figure 3.10. Band structure of a CBIRD (redrawn from ref. [63]).

When this detector is operated under zero bias or the upper contact is positive biased, the photogenerated minority carriers (electrons) formed in the absorber are collected

in the upper contact (hB) via diffusion/drift. Excess holes are recombined with electrons injected from the bottom contact (InAsSb).

3.5 Barrier Detectors without Sb

As seen above, ABCS (or 6.1Å III-V family materials) are the most suitable material system to obtain a barrier detector. In particular, for the barrier detector, due to the band offset between them, GaSb/AlSb, InAs/AlSb, and InAs/GaSb material pairs provide very important flexibility in obtaining various alloy and superlattice materials. However, the same conditions do not apply for technologically mature systems, such as HgCdTe and InGaAs. Since these two detector materials form the type-I heterojunction structure with the materials that are lattice-matched, it is not naturally easy to create an ideal unipolar barrier detector with these materials.

In the $Hg_{1-x}Cd_xTe$ material system, the bandgap changes as the x mole fraction changes, but the lattice constant almost does not. Although this situation provides one of the most important conditions for barrier detectors, simultaneously, the barrier layer prevents majority and minority carriers flow due to the type-I band lineup.

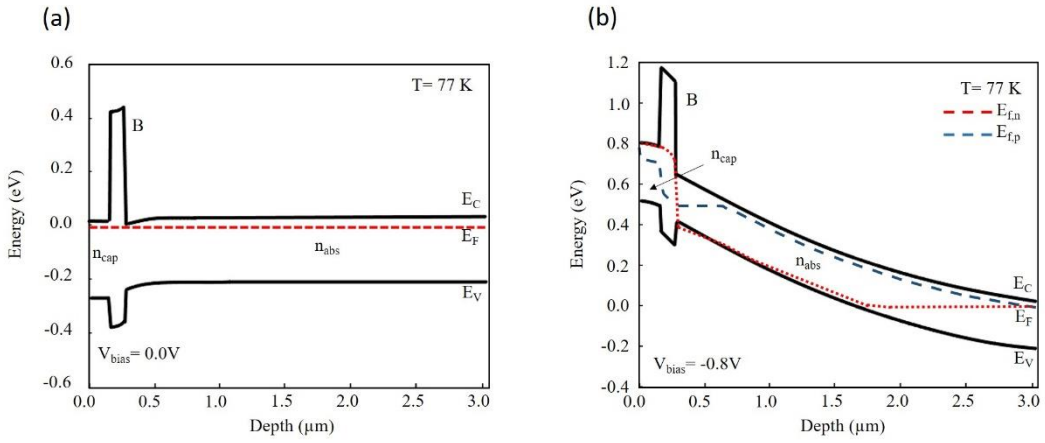

Figure 3.11. Calculated band structures of the MWIR HgCdTe nBn detector (a) at equilibrium and (b) under reverse bias (redrawn from ref. [73]).

Computed band diagrams of the nBn type HgCdTe barrier detector, which was fabricated for the first time by Anne M. Itsuno et al. are shown in Figure 3.11 [73]. While the Cd mole fraction of the absorber material of the detector was x~0.3 (MWIR), the Cd mole fraction of the barrier layer was chosen as x~0.64.

As seen in Figure 3.11 (b), relatively higher bias had to be applied for the holes to overcome the offset in the valence band [73].

However, the high electric field in the absorber causes band bending. This has increased the probability of non-ideal effects, such as tunneling in the created depletion region. If the low Cd mole ratio is used in the barrier layer, the valence band offset can be reduced, but since the conduction band barrier height also decreases, the flow of majority carriers will not be prevented, and dark current increases.

There are also studies of HgCdTe barrier detectors where the valence band-offset was eliminated by doping p-type. In Figure 3.12, the calculated band diagram results of the study of M. Kopytko et al. for p-type barrier HgCdTe nBn are given for MWIR and LWIR bands [49].

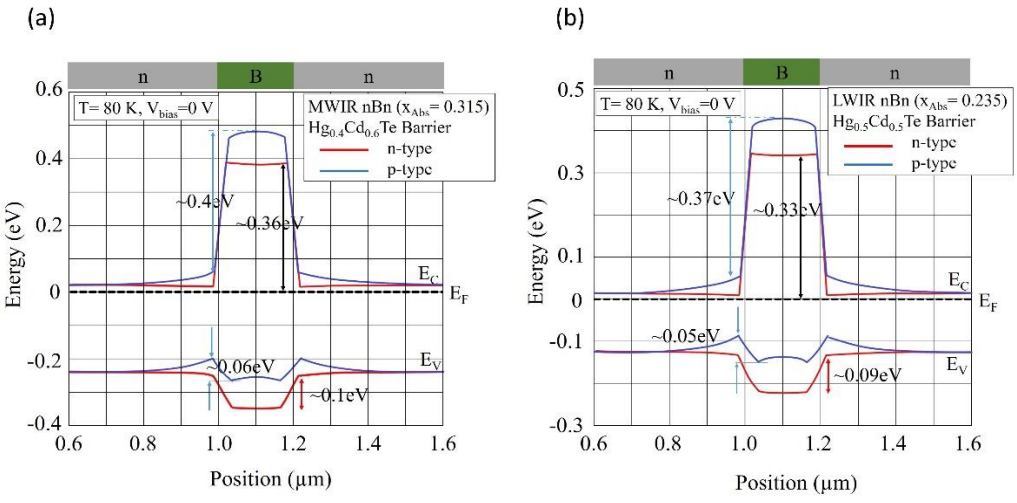

Figure 3.12. Calculated band diagrams for (a) MWIR and (b) LWIR HgCdTe nBn detectors with n-type and p-type doped barrier layer at equilibrium (redrawn from ref. [49]).

In their study, which was conducted in MWIR and LWIR bands, the valence band barrier was suppressed via p-type doping. In this way, the flow of the holes into the contact was ensured. However, since the valence band barrier p-type was doped, the space charge region was formed in the absorber/barrier interface causing the SRH thermal generation.

N. D. Akhavan et al. showed numerically that the valence band offset barrier layer can be removed with simultaneous grading of composition and doping concentration.

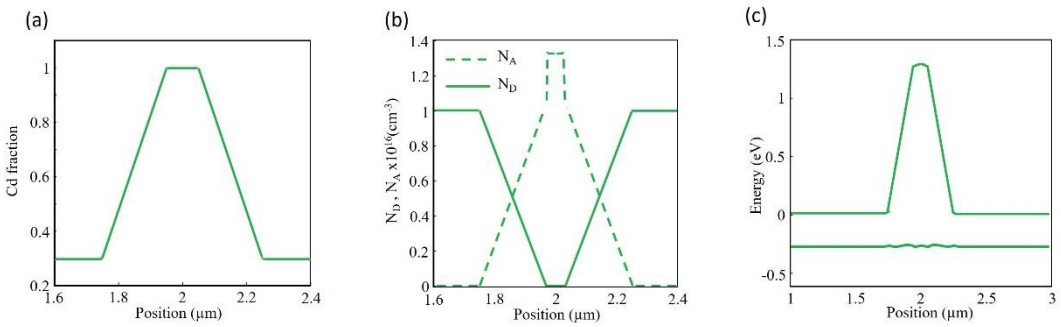

Figure 3.13. (a) Cd mole fraction profile, (b) doping concentration profile and (c) band diagram of valence band compensated HgCdTe nBn detector (redrawn from ref. [48]).

As seen in Figure 3.13, in this method, after the n-type absorber layer, the Cd mole ratio of the n-type $Hg_{1-x}Cd_xTe$ material was increased linearly with increasing the thickness, while the n-type doping concentration was reduced and the p-type doping concentration was increased simultaneously, and the barrier region became p-doped. In this case, after keeping the barrier thick enough, the Cd mole ratio was decreased, while this time p-type doping concentration was decreased, n-type concentration was increased simultaneously, and as a result, a zero-valence band barrier layer was obtained. However, as can be easily understood, since the barrier was p-type doped in this structure, a pn junction region was formed between the absorber and barrier layers [48].

There are also studies where the barrier layer was designed as a superlattice to remove the valence band-offset for the HgCdTe nBn detectors. In these studies, it

was theoretically shown that the unipolar barrier layer could be obtained using the type-III HgTe/CdTe superlattice (SL) material system (Figure 3.14) [49], [50], [74].

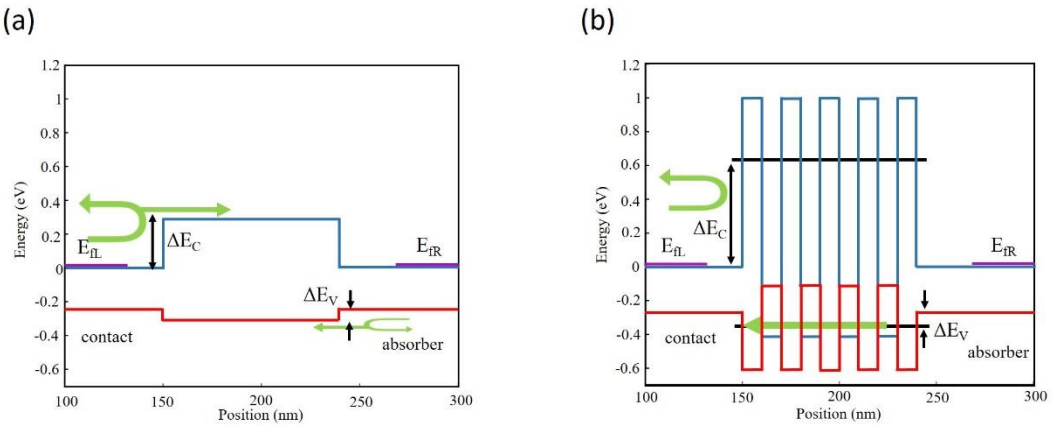

Figure 3.14. Calculated band diagrams of (a) an alloy barrier nBn detector and (b) superlattice barrier HgCdTe nBn detector (redrawn from ref. [74]).

The first Sb-free pBn-type InGaAs barrier detector was produced by J. F. Klem et al. As seen in Figure 3.15, lattice-matched un-doped InAlAs material was used as the barrier layer [75].

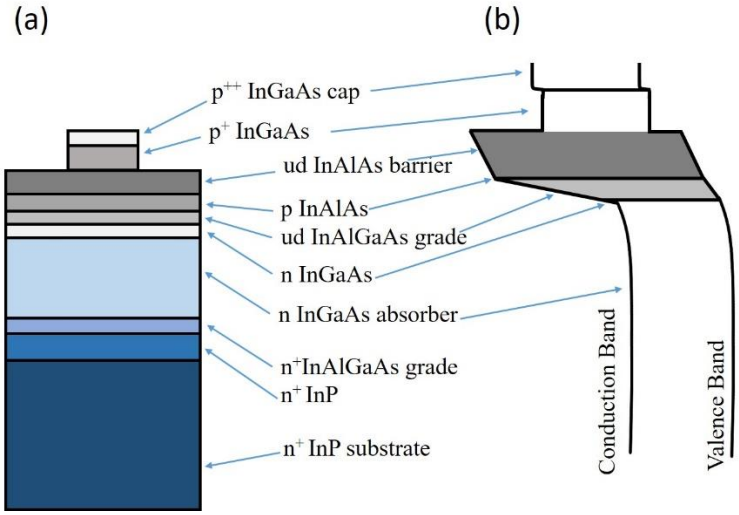

Figure 3.15. (a) Pixel structure and (b) band structure of a pBn InGaAs barrier detector (redrawn from ref. [75]).

In their study, a InAlGaAs lattice-matched graded layer was inserted between the InGaAs absorber and InAlAs barrier layers. Moreover, n and p delta-doping layers were placed on both sides of the graded layer to remove the valence band offset. Although the dark current was sufficiently suppressed, SRH generation would still occur because this structure contained the depletion region [59], [76].

In this thesis study, the graded layers with delta-dopings used by J. F. Klem to obtain a pBn detector was used to obtain InGaAs and HgCdTe nBn detector structures with different cutoffs and configurations. In the next section, this method will be elaborated.

CHAPTER 4

THE APPLIED DESIGN AND SIMULATION METHODOLOGY

In this section, first, the method to solve the valence band-offset problem that occurs in InGaAs and HgCdTe nBn detectors will be mentioned, and then the methodology of the numerical simulation used in the thesis will be explained.

4.1 Valence Band Suppressing in Graded Barrier Layer for nBn Detectors

As mentioned in the previous chapter, obtaining a unipolar barrier using heterojunction structures with type-I band alignment is not as easy as in type-II band alignment material systems. However, the valence band offset can be removed using compositional grading and delta-doping layers in nBn detectors with type-I band alignment. This method was used for the first time in a study by C. Nguyen at al. [77]. In their study, the conduction band offset between the base and collector was removed using linear compositional graded (using a chirped superlattice) and dipole delta-doping layers for an AlInAs/GaInAs/InP double heterojunction bipolar transistor (DHBT) (Figure 4.1). In this structure, the conduction band quasi-electric field resulting from the graded layer was suppressed by inserting a p-type delta-doping layer on the base side and an n-type delta-doping layer on the collector side. In this way, the conduction band difference was transferred to the valence band, so the conduction band barrier was eliminated.

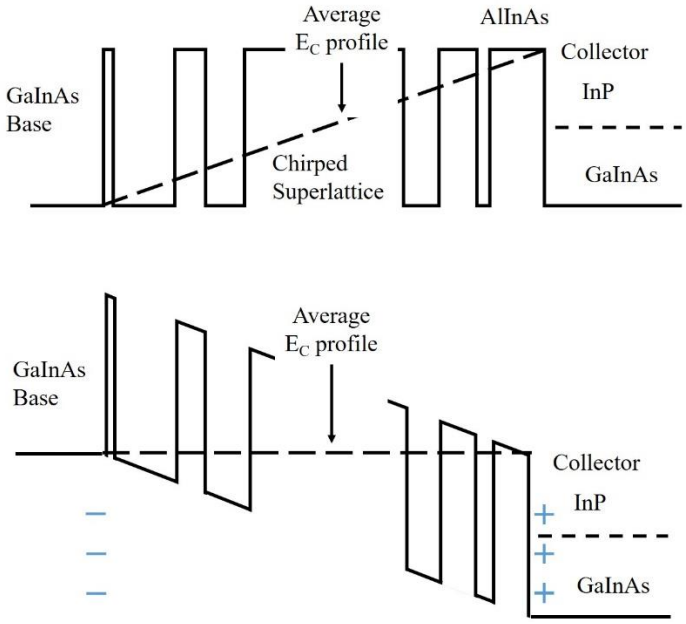

Figure 4.1. Schematic representation of conduction band suppressing for an AlInAs/GaInAs/InP (redrawn from ref. [77]).

In this thesis, the method which had been firstly used by C. Nguyen to suppress the conduction band offset was used to suppress the valence band offset in InGaAs and HgCdTe nBn detectors with different cutoffs and configurations [77].

The architecture of the graded unipolar barrier nBn detector, in which the valence band barrier is suppressed using dipole delta-doping layers, will be described below.

4.1.1 Compositional Grading

The bandgap of many binary and multiple compound semiconductors depends on the composition. If the mole fraction ratio of the compound semiconductors is changed depending on the position, the bandgap will change depending on the position. The semiconductor layers obtained by this method are called compositionally graded semiconductors (CGSs), and were first introduced by Kroemer in 1957 [78].

Suppose that A_xB_{1-x} is a binary semiconductor alloy, where A and B are chemically miscible semiconductor materials. The bandgap of the A_xB_{1-x} alloy is expressed by:

$$E_g^{AB} = xE_g^A + (1-x)E_g^B + x(1-x)E_b \qquad (4.1)$$

where E_g^A and E_g^B are the bandgap energies of the A and B semiconductors. Coefficient E_b is called the bowing parameter. This parameter is too small for compounds like $(AlAs)_x(GaAs)_{1-x}$ [79] .

The schematic representation of the band diagram of a linearly graded semiconductor compound is shown in Figure 4.2. Here, A is the low bandgap and B is the high bandgap semiconductor.

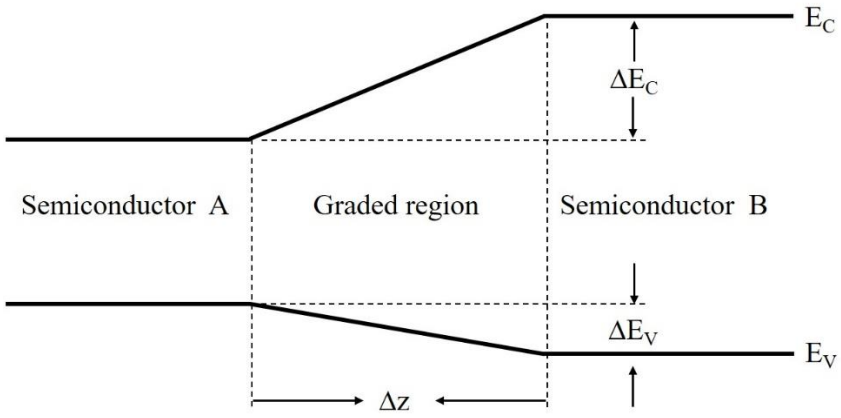

Figure 4.2. Schematic representation of the band diagram of a linearly graded intrinsic semiconductor compound (redrawn from ref. [79]).

As seen in Fig 4.2, the A and B semiconductor conduction and valence band edges are parallel to each other. However, the conduction and valence band edges of the compositionally graded region have different slopes and the bandgap changes with Δz thickness. ΔE_C, ΔE_V, and ΔE_G depend on the x mole fraction of the A_xB_{1-x} alloy.

The band diagram of the semiconductor can be bent with an applied electric field, as seen in Figure 4.3 (a). As it appears here, since the conduction and valence bands

edges are parallel, electrons and holes are exposed to electric force in opposite directions due to the external electric field.

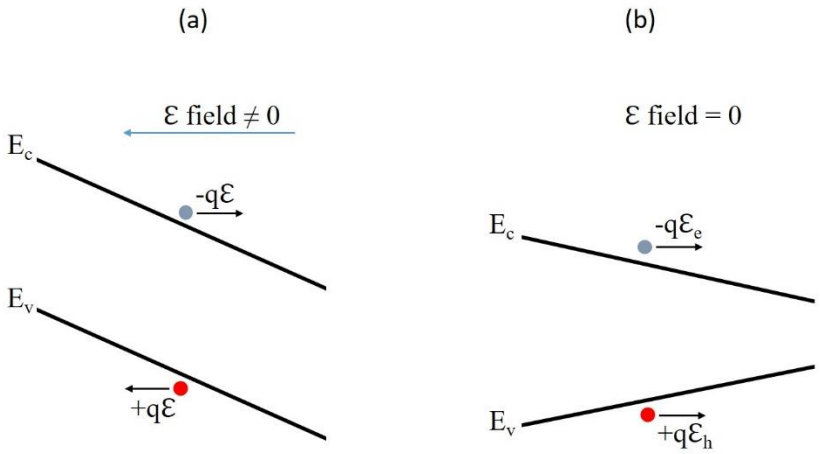

Figure 4.3. Schematic representation of band diagrams of (a) homogenous intrinsic semiconductor under electric field and (b) compositional graded intrinsic semiconductor under zero electric field (redrawn from ref. [78]).

However, the situation is different for an intrinsic CGS. Although no electric field is applied to an intrinsic CGS, the electrons and the holes move in the same direction as if they are exposed to different direction electric fields. (Figure 4.3 (b)). In an electric field applied homogeneous semiconductor, it is not possible for electrons and holes to move in the same direction. This mechanism, which was noticed by Kroemer for the first time, was named as the quasi-electric field by himself [78].

The conduction and valence band quasi-electric fields for the graded region shown in Figure 4.2 can be given by:

$$|\mathcal{E}_C| = \Delta E_C/(q\Delta z) \tag{4.2}$$

$$|\mathcal{E}_V| = \Delta E_V/(q\Delta z) \tag{4.3}$$

where $\mathcal{E}_C$ and $\mathcal{E}_V$ are the quasi-electric fields in the conduction and valence bands.

The band structures of p-type and n-type CGSs are given in Figure 4.4.

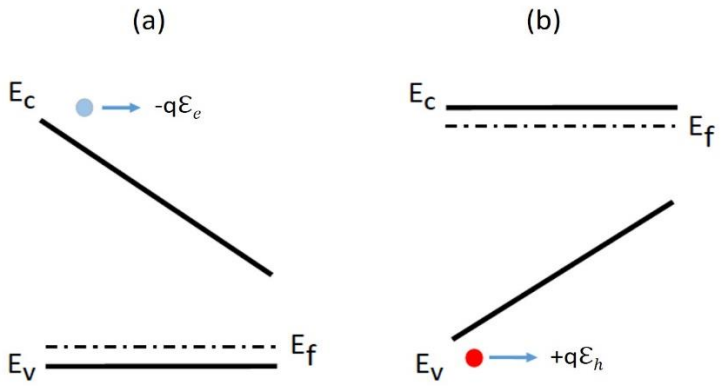

Figure 4.4. Schematic representation of band diagrams of (a) p-type doped and (b) n-type doped compositional graded compounds (redrawn from ref. [80]).

The band structure for a p-type doped graded compound is shown in Figure 4.4 (a). Due to the flat valence band, there is no quasi-electric field on the holes. However, conduction band electrons feel more force when compared to the intrinsic case, since the valence band offset is transferred to the conduction band. In Figure 4.4 (b), the same effect is illustrated for the n-type doped graded compound.

F. Capasso interpreted the doped graded semiconductor band structure as follows: in the graded structure with acceptor dopant, the holes accumulate towards the low bandgap part due to the quasi-electric field in the valence band and the high bandgap part remains negative due to ionized acceptor atoms [80]. Therefore, an electrostatic field emerges between the holes in the low bandgap part and the ionized acceptors in the large bandgap part. The flow of holes continues until the valence band quasi-electric field is equal to the electrostatic field. When these two fields are equal to each other, thermodynamic equilibrium is reached, and the valence band is flattened. (Figure 4.4 (a)). As a result, in the case of thermodynamic equilibrium, there is no net force on the holes since there is no net electric field on the valence band of the

p-type doped CGS. However, the same situation is not valid for electrons because the quasi-electric and the electrostatic field in the conduction band are in the same direction and the sum of these two causes a higher slope in the conduction band. The same argument can be applied for n-type graded semiconductor material. Therefore, the electric fields in the conduction and valence bands for p-type and n-type graded semiconductors in the thermodynamic equilibrium are expressed as follows:

$$\mathcal{E}_e = -\frac{1}{q}\frac{dE_g}{dz} \ (for\ p-type\ \text{CGS}), \tag{4.4}$$

$$\mathcal{E}_h = +\frac{1}{q}\frac{dE_g}{dz} \ (for\ n-type\ \text{CGS}). \tag{4.5}$$

The existence of the quasi-electric field was experimentally demonstrated by Levine et al. [81], [82]. In their study, it was observed that the quasi-electric field formed in the graded layer had the same effect on regular carriers and fit the drift velocity relation v = μE (E is the quasi-electric field).

4.1.2 Compositional Graded Barrier nBn Detector

As mentioned in the previous section, both types of carrier flow are prevented in the barrier layers obtained using material systems with type-I band alignment, since both bands (conduction and valence) have band-offset. Although a unipolar barrier is obtained with a uniform doped compositionally graded layer (Figure 4.5), it prevents photocurrent formation since the barrier prevents minority carrier flow in an nBn structure.

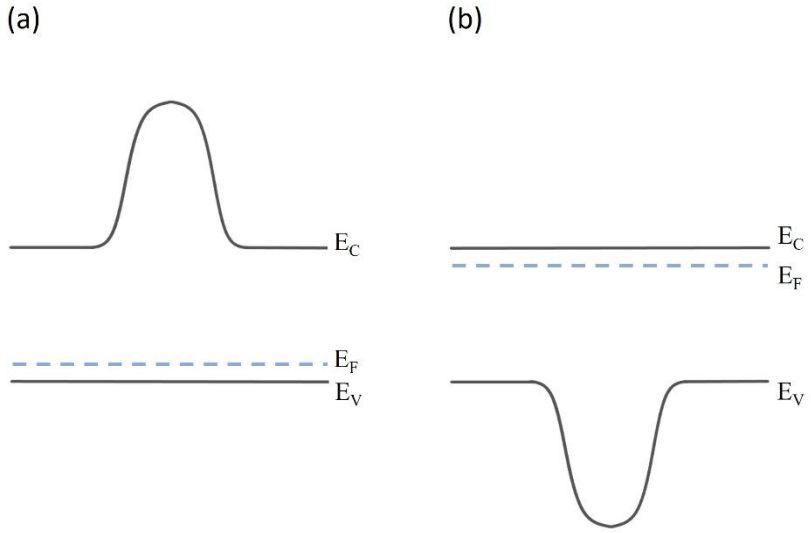

Figure 4.5. Schematic representation minority carrier unipolar barrier in (a) n-type and (b) p-type CGS (redrawn from ref. [39]).

In order to achieve a useful barrier case, the graded layer doping type should be different from the absorber layer, but it would effectively lead to a pn junction with a depletion region, and the dark current mechanisms would not be satisfactorily eliminated [39]. Therefore, additional band diagram engineering methods are necessary for the desired characteristics.

As mentioned previously, the quasi-electric field formed in compositionally graded layers can be suppressed with delta-doping layers [75], [77]. In this thesis study, two graded layers and two pairs (n-type and p-type) of delta-doping layers were used to obtain valence band free nBn detector architecture. As seen in Figure 4.6, in the nBn structure obtained with the compositionally graded barrier of the $A_xB_{1-x}C$ ternary compound, band offset is formed in both bands. However, since the quasi-electric field can be suppressed in the desired band with the delta-doping layer assist, using an un-doped compositionally graded layer in the nBn detector structure is a great advantage to achieve zero valence band offset.

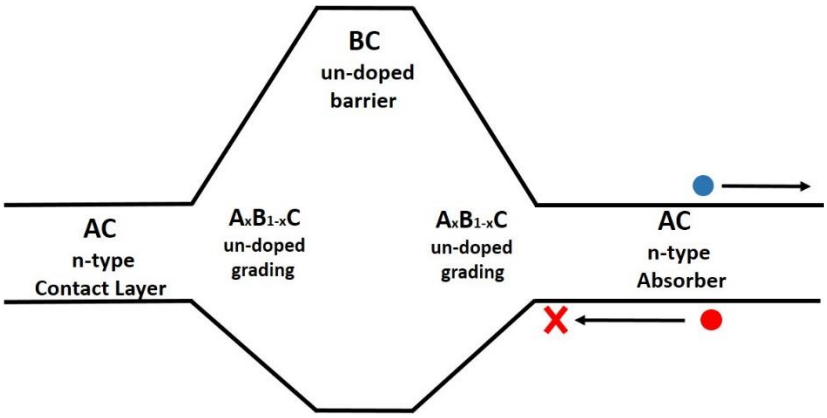

Figure 4.6. Schematic representation of a compositionally graded barrier nBn detector band structure with a valence band offset [83].

As seen in Figure 4.7, when n-type delta-doping is inserted in the low bandgap part of the un-doped bandgap graded layer, and p-type delta-doping is inserted in the high bandgap part, the donor and acceptor ions form an electric field that is in the opposite direction to the quasi-electric field in the valence band. When the magnitude of the electric field is equal to the quasi-electric field in the valence band, the valence band flattens, and the conduction band slope increases since the effective electric field in the conduction band increases.

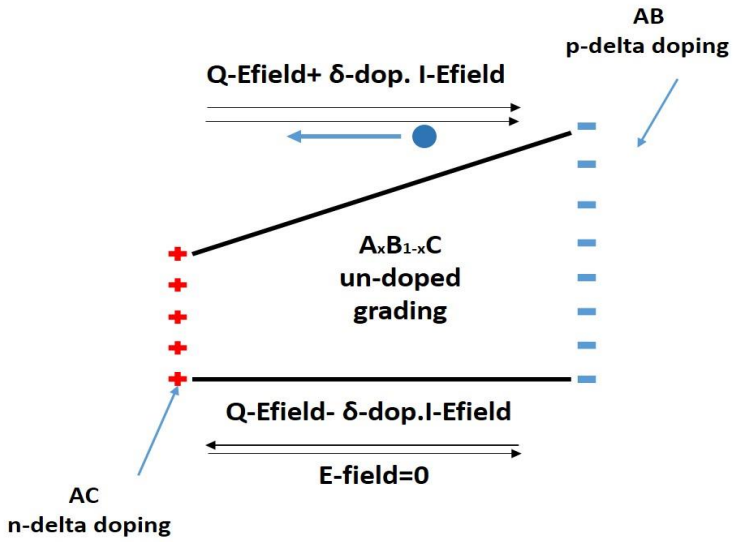

Figure 4.7. Schematic band diagram of a valence band compensated CGS using delta-doping layers [83].

As shown in Figure 4.8, in order to suppress the minority carrier barrier in an nBn detector, n-type and p-type delta-doped layers are placed at the sides of both graded layers. Consequently, the valence band quasi-electric field is canceled, and the valence band offset is suppressed.

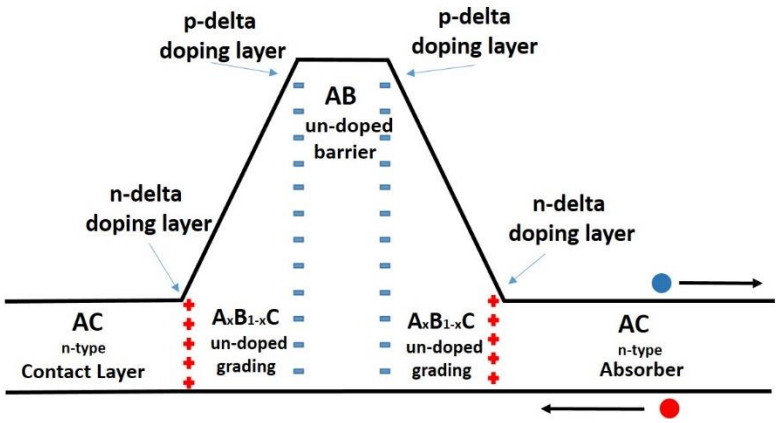

Figure 4.8. Schematic band diagram of the valence band compensated compositionally graded barrier nBn detector structure [83].

This structure effectively blocks only majority carriers and allows the flow of minority carriers. Therefore, dark current suppression is obtained without any compromise in the photoresponse. Moreover, the barrier thickness, height, and valence offset are tuned by changing the barrier material thickness, composition, and delta-doped layer doping concentration [83].

4.2 Technology Computer-Aided Design (TCAD)-Based Simulation

In this thesis study, numerical calculations of the applied nBn architecture and the conventional heterojunction architecture were performed using Synopsys TCAD Sentaurus Device simulator. Sentaurus TCAD simulator is an advanced multi-dimensional computational tool to simulate electrical, optical, thermal characteristics and manufacturing process of semiconductor devices. In the device simulator, voltages, currents and charges are calculated using equations describing the conduction mechanisms and carrier distribution. The physical properties of the device are simulated as a uniform discrete grid (mesh) [84]. Sentaurus TCAD simulator is used in the development of a wide range of semiconductor devices such as CMOS, analog/RF, memory, power, image sensors, and solar cell devices [85].

Sentaurus TCAD consists of many modules and simulation tools. The complete simulation flow chart is given in Figure 4.9.

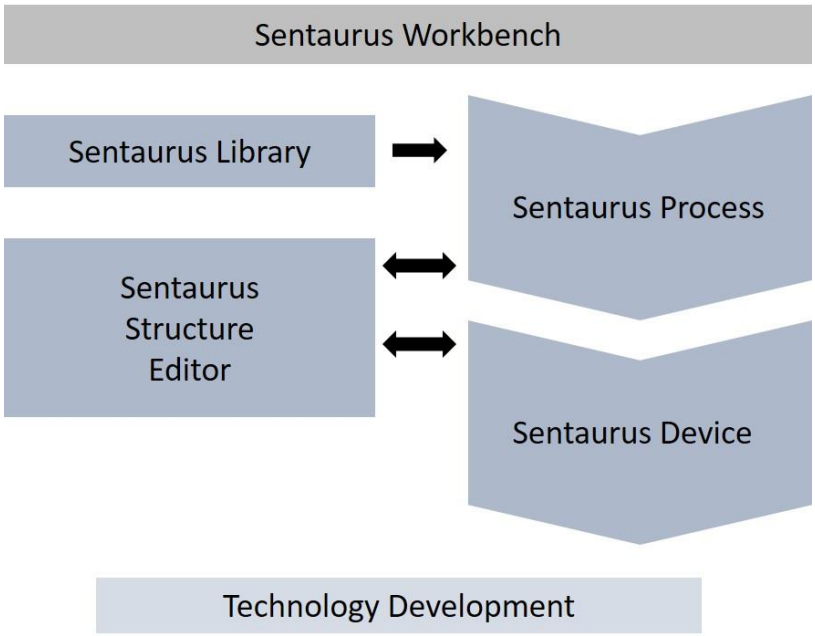

Figure 4.9. The flowchart of a typical device simulation using Sentaurus TCAD [85].

4.2.1 Sentaurus Structure Editor

The Sentaurus Structure Editor is a structure tool, which can be used to simulate two-dimensional (2D) or three-dimensional (3D) device structures. The geometry of the structures, doping profiles, and meshing strategies can be defined interactively or using scripts. Here, the Scheme language is used for the scripting. The Sentaurus Structure Editor has an interface for configuring and calling the Synopsys meshing engines. Additionally, it generates the TDR boundary and mesh command input files for the meshing engines, which generate data file and the TDR grid file for the device structure [84].

4.2.2 Sentaurus Device

The Sentaurus Device (SD) numerically simulates the electrical, thermal and optical behavior of a single semiconductor or several combined devices in a circuit. Terminal currents, voltages, and charges are calculated using a set of device equations that depicts the conduction mechanisms and carrier distribution [84]. The equations are solved for each discrete point in the grid (mesh). Direct current (DC), alternative current (AC) and transient simulations can be performed using the SD module. Additionally, it generates output files containing information about energy levels, fields, potentials, carrier densities and temperatures within the device at various time points during the simulation [86].

A typical SD input command file consists of several command sections in which each section executes a relatively independent function. These sections are:

- **File section:** In the file section, the input and output files of the simulation are defined. The structure of the device is defined with input files such as regions of the device, the mesh, and the doping profiles. Output files contain the results of the simulations. There are 3 output files: Current, Plot and Output (output log or protocol file). The Current output file includes electrical output data such as voltages, currents, and charges at electrodes.

The Plot output file includes final spatial solution variables on the structure mesh. The Output log file includes the redirected standard output about the simulation [84].

- **Electrode section:** In this file section, all of the contacts used in simulation are defined together with the initial bias voltages and barrier. Here, the barrier is the metal-semiconductor work function difference [84].
- **Physics section:** In this file section, physical models to be used in device simulation are determined. Examples of these physical models are the carrier generation and recombination model, carrier mobility model, impact ionization model, bandgap narrowing model, and gate leakage model. Here, physical models can be determined globally, per region or material, per interface, or per electrode. Again in this section, mole fractions and trap specifications can be determined [84].
- **Math section:** In the simulation calculations, a set of partial differential equations is solved self-consistently, on the discrete mesh, in an iterative way. For each iteration, an error is calculated and the iteration continues until a solution with an acceptably small error is obtained [84].
- **Solve section:** In the simulation, user defines a sequence of solutions and specifies types of simulations, such as transient, quasistationary, small signal, and harmonic balance [87].
- **Plot section:** In this file section, solution variables that are saved in the output plot files (.tdr) are determined. Some variables include electron and hole quasi Fermi levels, space-charge, potential, electron and hole densities, doping concentrations, carrier concentrations, current densities, electric field distributions, and electron temperature [84], [87].

In the numerical calculations, the drift-diffusion model is used for the simulation of carrier transport in the virtual device. Drift-diffusion is the most suitable model for low-power density devices with long active regions, low electric field and low carrier density, which were studied in this work.

In this model, the Poisson's and continuity equations for the electrons and holes are calculated self-consistently using an approximate Newton method with Gaussian elimination [24].

The analytical expression, Poisson's equation, electron continuity and hole continuity equations are given by:

$$\varepsilon \nabla \phi = -q(p - n + N_D - N_A) - \rho_{trap}\,, \tag{4.6}$$

$$\nabla . \overrightarrow{J_n} = qR_{net} + q\frac{\partial n}{\partial t}\,, \tag{4.7}$$

$$-\nabla . \overrightarrow{J_p} = qR_{net} + q\frac{\partial p}{\partial t}\,, \tag{4.8}$$

where ϕ is the electrostatic potential (V), ε is the electrical permittivity (F/m), n and p are the electron and hole carrier concentrations (cm^{-3}), N_D and N_A are the ionized donor and acceptor concentrations (cm^{-3}), ρ_{trap} is the trap density, J_n and J_p are the electron and hole current density (A/cm^2) and R_{net} is the net carrier recombination rate.

Electron and hole current densities are expressed by:

$$\overrightarrow{J_n} = -qn\mu_n\vec{\nabla}\Phi_n \tag{4.9}$$

$$\overrightarrow{J_p} = -qn\mu_p\vec{\nabla}\Phi_p \tag{4.10}$$

where μ_n and μ_p are the electron and hole mobility ($cm^2/V.s$), and Φ_n and Φ_p are the electron and hole quasi-Fermi potential (V).

In the SD, the partial differential equations (PDEs) are discretized based on the box discretization method. In this model, the PDEs are integrated over a test volume, such as that given in Figure 4.9.

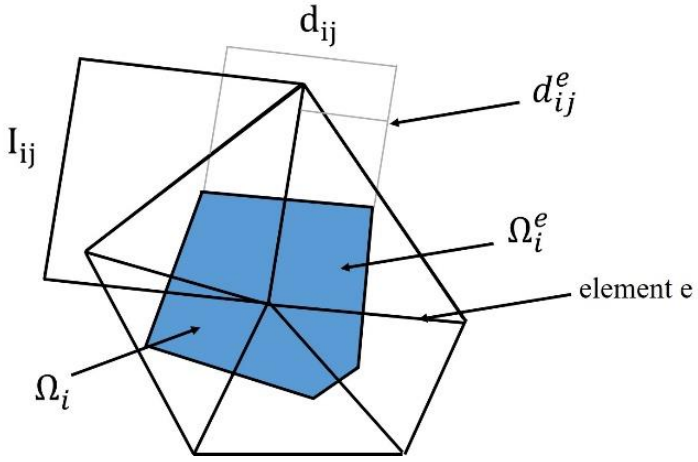

Figure 4.10. Schematic representation of a triangular box discretization mesh in 2 dimensions (redrawn from ref. [84]).

Each PDE is discretized from:

$$\nabla.\vec{J} + R = 0 \tag{4.11}$$

in to:

$$\sum_{j\neq i} \kappa_{ij}.j_{ij} + \mu(\Omega_i).r_i = 0 \tag{4.12}$$

where the κ_{ij} and $\mu(\Omega_i)$ parameters are below listed below for all 3 dimensions.

Table 4.1 κij and μ(Ωi) Parameters

Dimension	κ_{ij}	$\mu(\Omega_i)$
1D	$1/l_{ij}$	Box length
2D	d_{ij}/l_{ij}	Box area
3D	D_{ij}/l_{ij}	Box volume

Table 4.2 Discretized Equations

Equations	j_{ij}	r_i
Poisson	$\varepsilon(u_i - u_j)$	$-\rho_i$
Electron continuity	$\mu^n\,(n_i B(u_i - u_j) - n_j B(u_j - u_i))$	$R_i - G_i + \frac{d}{dt} n_i$
Hole continuity	$\mu^p\,(p_j B(u_j - u_i) - p_i B(u_i - u_j))$	$R_i - G_i + \frac{d}{dt} p_i$

Here, the j_{ij} and r_i physical parameters are above listed for the Poisson's, electron continuity, hole continuity and temperature equations ($B(x) = x/(e^x - 1)$, Bernoulli function). Table 4.2 gives the discretized form of the Poisson', electron continuity and hole continuity equations [84].

4.2.3 Material Parameters Used in the Simulations

The material parameters used in the simulation were taken from the library of Sentaurus TCAD [84] in accordance with the literature. They have also been entered manually when necessary. The material parameters manually used in the simulations are given in Table 4.3 and Table 4.4 for InGaAs and HgCdTe respectively.

Table 4.3 $In_{0.53}Ga_{0.47}As$ Material Parameters

Parameter	*Value*	*Reference*
Absorption coefficient at 1.55 μm (at 300 K).	7000 cm^{-1}	[2]
Surface recombination velocity	4.5×10^{4} cm/s	[88]
SRH lifetime	4.74×10^{-5} s	[89]
Calculated surface trap density for pn detector	6×10^{11} cm^{-2} for InGaAs 6×10^{11} cm^{-2} for InP	[90]
Calculated surface trap density for nBn detector	4.7×10^{11} cm^{-2} for n-InGaAs Absorber 4.7×10^{11} cm^{-2} for Delta doping layers 9.2×10^{8} cm^{-2} for InGaAs Barrier 1×10^{9} cm^{-2} for Grading Layers 5.64×10^{11} cm^{-2} for n-InGaAs Contact	[90]
Capture cross-section values for electrons and holes	10^{-14} cm^{2}	[27]

Table 4.4 HgCdTe Material Parameters

Parameter	*Value*	*Reference*
SRH Lifetime for the alternative substrate detectors	3×10^{-6} s for SWIR band 1×10^{-6} s for MWIR band 1×10^{-6} s for LWIR band	[91]
SRH Lifetime for CdZnTe substrate detectors	10×10^{-6} s for MWIR band 10×10^{-6} s for LWIR band	[91]
Trap energy levels	0.25Eg eV for SWIR band 0.25Eg eV for MWIR band 0.25Eg eV for LWIR band	[46]
Concentration	10^{13} cm^{-3} for SWIR band 10^{13} cm^{-3} for MWIR band 10^{13} cm^{-3} for LWIR band	[46]

4.2.4 Limitations in the Sentaurus TCAD

To obtain robust simulation results with Sentaurus TCAD, understanding the physics of the device and adjust the proper meshing accordingly is crucial. Furthermore, by understanding the device physics, it is possible to select more realistic models from the broad model library of Sentaurus TCAD so that more realistic models lead to better convergence of the simulation since some of the divergence issues are related to contradictory models. Additionally, parameter files of the materials that are going to be used in the device should be well-defined.

However, even if everything about grid sizes, physical models, and material parameters is well adjusted, some convergence problems might still occur. This is generally related with problems due to the numeric challenges during performance of floating-point operations with extremely small and extremely large numbers. For

example intrinsic carrier concentration of a wide-bandgap semiconductor at cryogenic temperatures is an example of extremely low number.

In addition, the drift-diffusion model may not give correct results in submicron devices and high electric field regimes, but these situations are outside this thesis study area, and also the electric field in the simulated devices here is too low to cause velocity-saturation of the carriers [92].

CHAPTER 5

InGaAs SHORT WAVE INFRARED (SWIR) PHOTODETECTORS

Short Wavelength Infrared (SWIR) detector technology, which has very important applications in military and civilian fields, produces images accustomed to the human eye by working with the principle of reflecting visible light from objects. Moreover, SWIR detectors are able to receive high-resolution images under nighttime conditions, even when there is no moonlight, due to a radiation source called the night glow. Since the operating temperature of SWIR detectors is much higher than that of thermal detectors, SWIR detectors can operate at room temperature or, if necessary, can be cooled with thermoelectric coolers (TEC). The fact that glass lenses can be used in the IR cameras operating in the SWIR band is also a cost-reducing factor. Therefore, SWIR detector technology is quite different from other IR technologies in terms of cost and system portability, and thanks to these differences, its applications (especially in the civil area) are increasing day-by-day. For example, due to their low cost and ability to take images even in fog, these SWIR detector cameras can be used to provide a much safer driving in cars. In addition, due to the LIDAR application in the SWIR band, unmanned aerial vehicles (UAV) and autonomous vehicles can determine the route without the need for GPS 3D mapping. Quality analysis of materials or foodstuffs produced in industrial area by SWIR imaging, inspection of vegetation coverings, monitoring of agricultural and forest areas, sub-surface imaging, and reading of deleted or tarnished documents are among the other applications that are not possible with thermal area (MWIR and LWIR) cameras.

Material technologies used for detectors operating in SWIR band are InGaAs, HgCdTe, and type-II superlattice. Among different material determinants, InGaAs is the most common material system due to its high quantum efficiency and relatively low-cost advantages. HgCdTe detectors use quite expensive CdZnTe material as the

substrate, and the alternative base HgCdTe detectors are still in the development stage. Type-II superlattice technology is not fully matured and has not reached the level of InGaAs in terms of production and process technologies and quantum efficiency.

5.1 Application Areas of Short Wave Infrared (SWIR) Detectors

SWIR covers 1 to 3 μm of the EM spectrum. A comparison of an image taken with a SWIR camera and an image taken with a thermal camera is given in Figure 5.1. As mentioned above, the SWIR images are similar to the image that the human eye is familiar with.

Figure 5.1. Comparison of LWIR (left) [10] and SWIR camera (right) [93] images.

The essential features of SWIR can be listed as follows;

- lower scattering than short wavelengths,
- contain spectroscopic information,
- active lighting using an invisible light source (active by laser or passive by nightglow)
- objects with a temperature above 150 degrees also radiate at this wavelength.

In many studies, InP lattice-matched InGaAs (operating between 0.9 μm and 1.7 μm) has been shown to be the most suitable material for imaging in the SWIR band (Figure 5.2) [94].

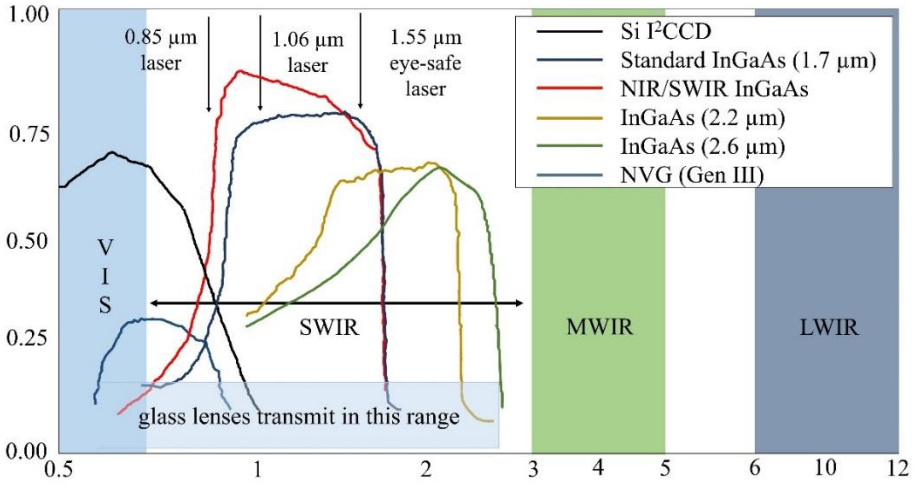

Figure 5.2. IR radiation spectrum with InGaAs detectors quantum efficiency (redrawn from ref.[95]).

Since some overtones of molecular vibrations of moister, proteins, esters, lipids, and other chemicals with C-H, N-H and O-H molecules are in the SWIR band range, spectroscopic information can be obtained by detection in the SWIR band in such substances. O-H molecules in the upper layers of the atmosphere radiate during the night, causing an illumination called nightglow. Since nightglow emission overlaps with the SWIR band, this band enables night viewing in the open air [94].

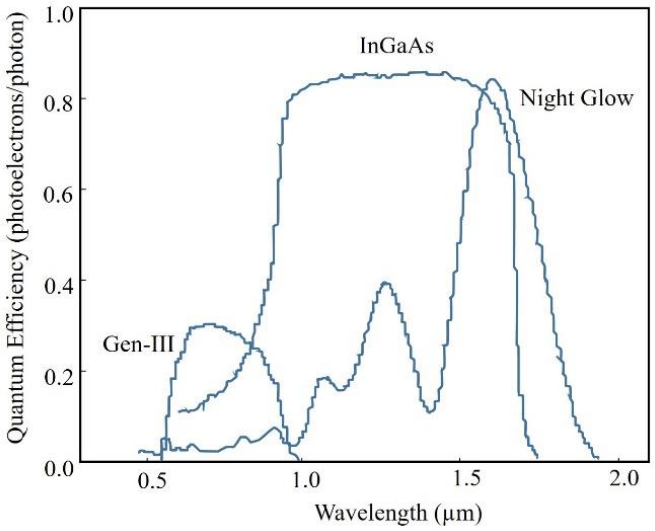

Figure 5.3. Lattice-matched InGaAs IR detector quantum efficiency and night glow radiance (redrawn from ref. [94]).

Figure 5.3 also shows that there are areas where the lattice-matched InGaAs SWIR detector quantum efficiency and night glow radiance spectrums overlap [94].

The radiance spectrum of the nightglow emission for different conditions is given in Figure 5.4.

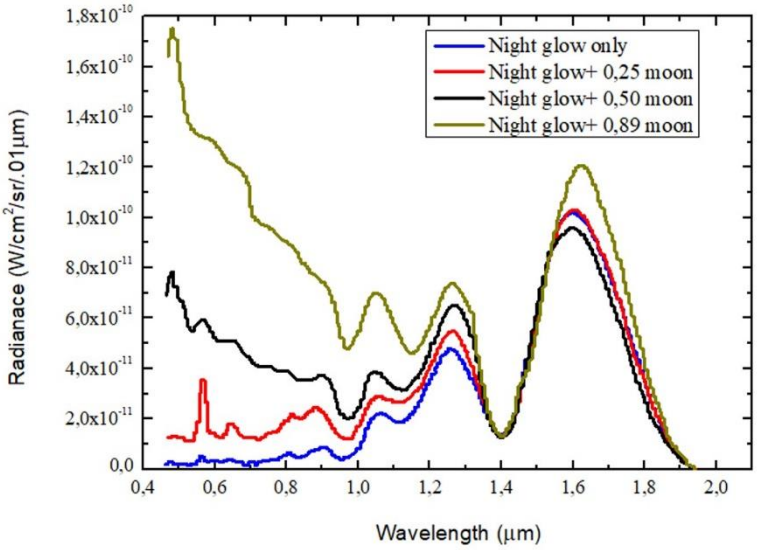

Figure 5.4. Spectral radiance of night glow under various conditions (redrawn from ref. [95]).

The ability to see behind the haze is a very important advantage of SWIR cameras. Due to Rayleigh scattering, the probability of scattering in the atmosphere decreases as the wavelength increases, so a better view is obtained with the SWIR camera in hazy weather than the visible camera.

SWIR imaging has important application areas in medicine. The optical coherence tomography (OCT) technique is used for 2D or 3D imaging of opaque or semi-transparent biological tissues. In this technique, using the SWIR wavelength, it can capture a deeper image due to Rayleigh scattering [94].

Another medical practice with SWIR detectors is that the veins on the arms and legs can be displayed by external illumination. This method can especially be applied to the elderly and infants whose veins are difficult to locate [94].

SWIR imaging has many applications in industry. For example, SWIR cameras can be used to determine the filling levels of bottles with liquids, water concentrations in liquids), and to see if food is fresh.

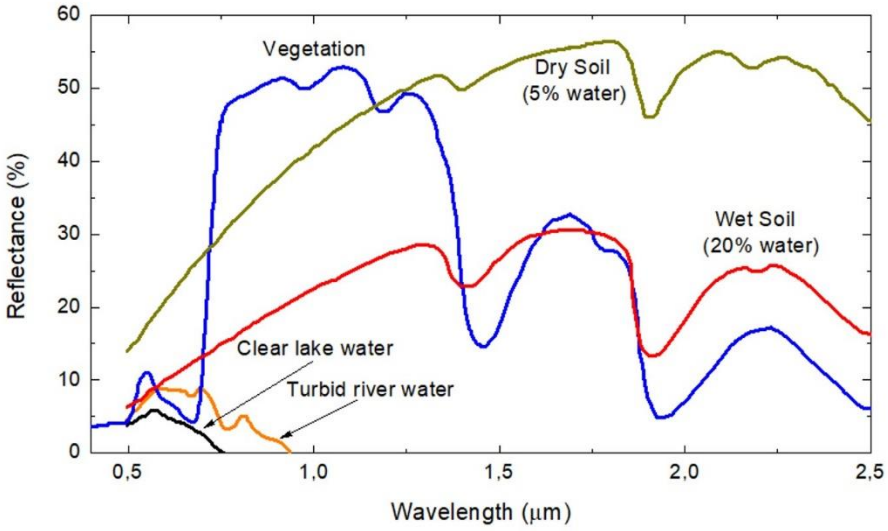

Figure 5.5. Spectral reflectance of some materials on the ground (redrawn from ref. [96]).

Another application area of the SWIR band is hyperspectral imaging. Hyperspectral imaging is created by obtaining data in adjacent wavelengths. This method, also called chemical imaging, is used in areas such as geosciences, agriculture, biomedical imaging, molecular biology, astronomy, physics, and surveillance. In this method, materials containing O-H, N-H and C-H molecules can be detected using the SWIR band. In addition, as seen in Figure 5.5, in the SWIR band range, the materials have different reflectance at different wavelengths. In this way, the materials are identified and distinguished.

5.2 InGaAs Material Properties

$In_xGa_{1-x}As$ is a variable bandgap semiconductor alloy. It is used extensively in electronic and optoelectronic technologies such as MOSFETs, HBTs, HEMTs, photodetectors and lasers due to its superior electrical and optical properties.

$In_xGa_{1-x}As$ is composed of indium arsenide (InAs) and gallium arsenide (GaAs) semiconductor compounds. The crystal structure of $In_xGa_{1-x}As$ is zinc-blende because InAs and GaAs compounds are perfectly miscible and both are zinc-blende.

The bandgap of $In_xGa_{1-x}As$ varies with the x mole fraction and it is given with an empirical formula, shown in Eq. (5.1), depending on the temperature [17]. For the 300 K bandgap of $In_xGa_{1-x}As$ changes from 1.435 eV (x=0, GaAs) to 0.35 eV (x=1, InAs).

$$E_g(x,T) = 0.42 + 0.625\,(1-x) - \left(\frac{5.8}{T+300} - \frac{4.19}{T+271}\right)10^{-4}T^2(1-x) - \frac{0.000419}{T+271}T^2 + 0.475(1-x)^2 \quad (5.1)$$

Here, T (K) is the temperature.

The bandgap energy and cutoff wavelength value of $In_xGa_{1-x}As$ material for the different In mole fraction (x) at 300 K are shown in Figure 5.6. In $In_xGa_{1-x}As$ material system, $In_{0.53}Ga_{0.47}As$ material with an In mole fraction x = 0.53 is InP a lattice-matched. This material, which has a bandgap of 0.74 eV at room temperature, has features such as high electron mobility, high electron velocity, and a large intervalley separation, making it a very useful material in electronic and optical fields. In particular, the wavelength range (SWIR band) corresponding to the bandgap of the $In_{0.53}Ga_{0.47}As$ material is subjected to very little loss and dispersion in the optic fiber.

These properties make InGaAs and its hetero structures a very suitable material for optoelectronic integrated circuit devices (OICD). Heterostructures with InP lattice-matched can be given as follows: $In_{0.53}Ga_{0.47}As/InP$, $In_{0.53}Ga_{0.47}As/In_{0.52}Al_{0.48}As$, $In_{0.53}Ga_{0.47}As/In_{1-x}Ga_xAs_yP_{1-y}$, and $In_{0.53}Ga_{0.47}As/In_xGa_yAl_{1-x-y}As$ [97].

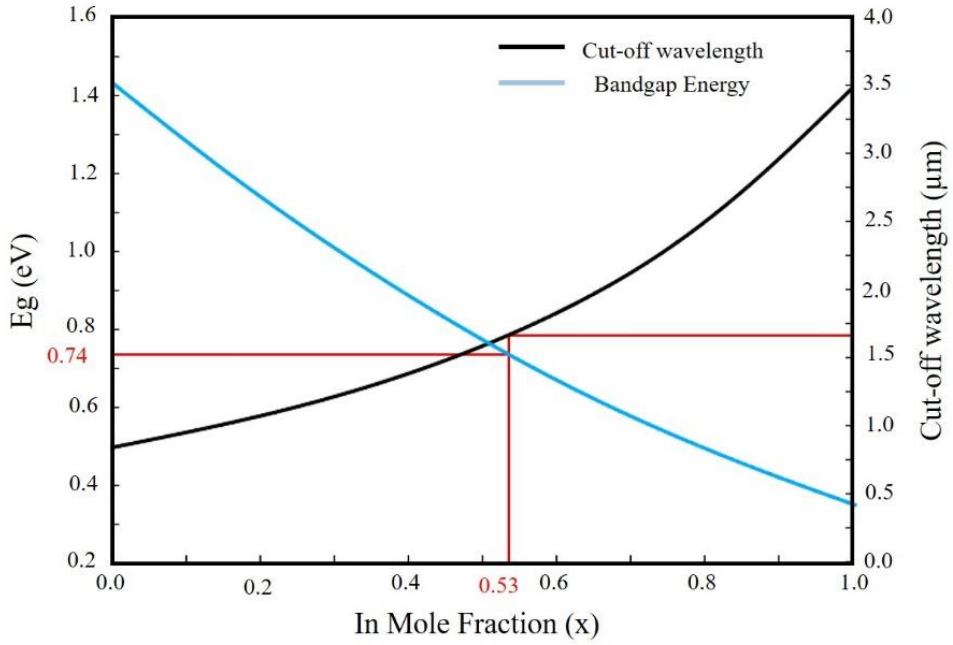

Figure 5.6. Variation of the band-gap of $In_xGa_{1-x}As$ ternary semiconductor with In mole fraction (x) (redrawn from ref. [17]).

$In_xGa_{1-x}As$ materials with In mole ratio other than x = 0.53 are lattice mismatch with InP substrates.

Two different lattice mismatch structures are obtained as relaxed, or strained-relieved and pseudomorphic using different In mole fractions. In this way, heterostructures obtained by changing the x mole fraction in $In_xGa_{1-x}As$ material system enable the development of quantum devices, high performance electronic and optoelectronic devices [97].

5.3 InGaAs Shortwave Infrared Detectors

As mentioned previously, $In_xGa_{1-x}As$ is in many ways the most suitable material system for SWIR detection. Lattice-matched $In_{0.53}Ga_{0.47}As$ material with a 1.7 μm cutoff wavelength from at room temperature does not cover the entire SWIR band, although it is used very intensively. However, since the atmosphere is still permeable in this region where wavelengths greater than 1.7 μm in the SWIR band are not

detected with a lattice-matched InGaAs, many applications need detection. For this, by increasing the In mole ratio, detectors with a larger cutoff of up to 3.6 µm can be obtained. In these structures, called extended wavelength SWIR InGaAs detector, since there is no substrate suitable for the absorber lattice constant, the absorber is grown as a lattice-mismatch on InP; however, this degrades the performance of the detector. This is because dislocations behave like G-R centers in mid-gap, thus increasing the dark current due to the G-R current. In this thesis, it has been shown that with the applied nBn structure, the dark current caused by dislocations can be reduced efficiently. In Figure 5.7, the quantum efficiency responses of InGaAs detectors with wavelengths of 1.7 µm, 2.2 µm, and 2.5 µm are given.

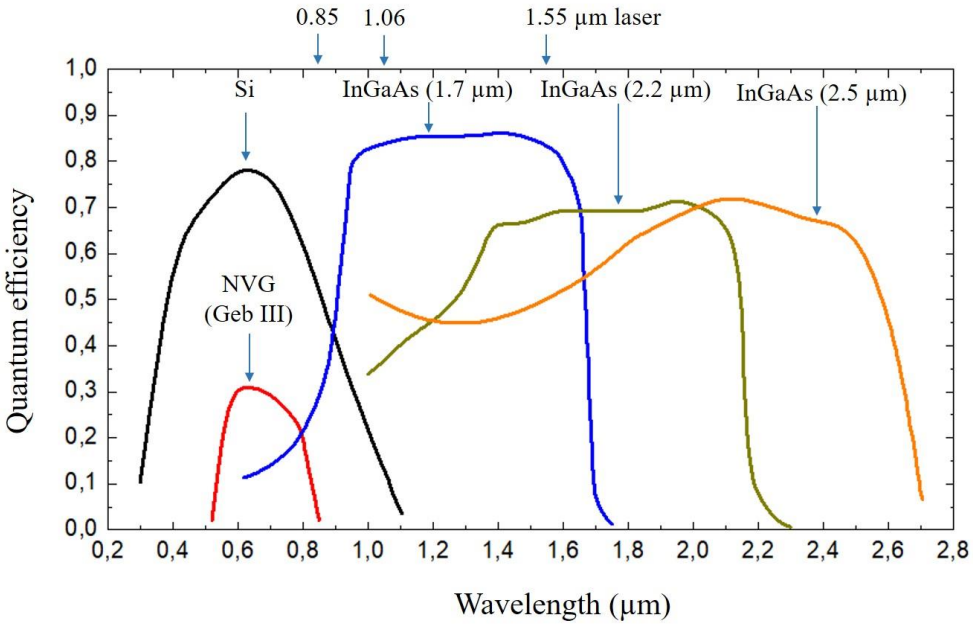

Figure 5.7. Quantum efficiency spectrum of $In_xGa_{1-x}As$ with wavelengths of 1,7 µm, 2.2 µm, and 2.5 µm (redrawn from ref. [2]).

5.3.1 InGaAs Shortwave Infrared Detector Structure

Two different detector structures are used: PD and avalanche photodiode (APD) for SWIR detection using InGaAs material. Although APDs can detect more precisely

than PDs, they are less preferred for SWIR imaging due to reasons such as avalanche noise, higher bias voltage, and higher dark current.

As it is known, PD detectors are obtained by a metallurgical junction (homojunction or heterojunction) of n- and p-type semiconductor materials. Pin (p-type, intrinsic, n-type) is a commonly used diode structure for InGaAs SWIR detectors (Figure 5.8). This structure is designed by placing an un-doped (or lightly doped) intrinsic layer between layers of highly doped n- and p-type material.

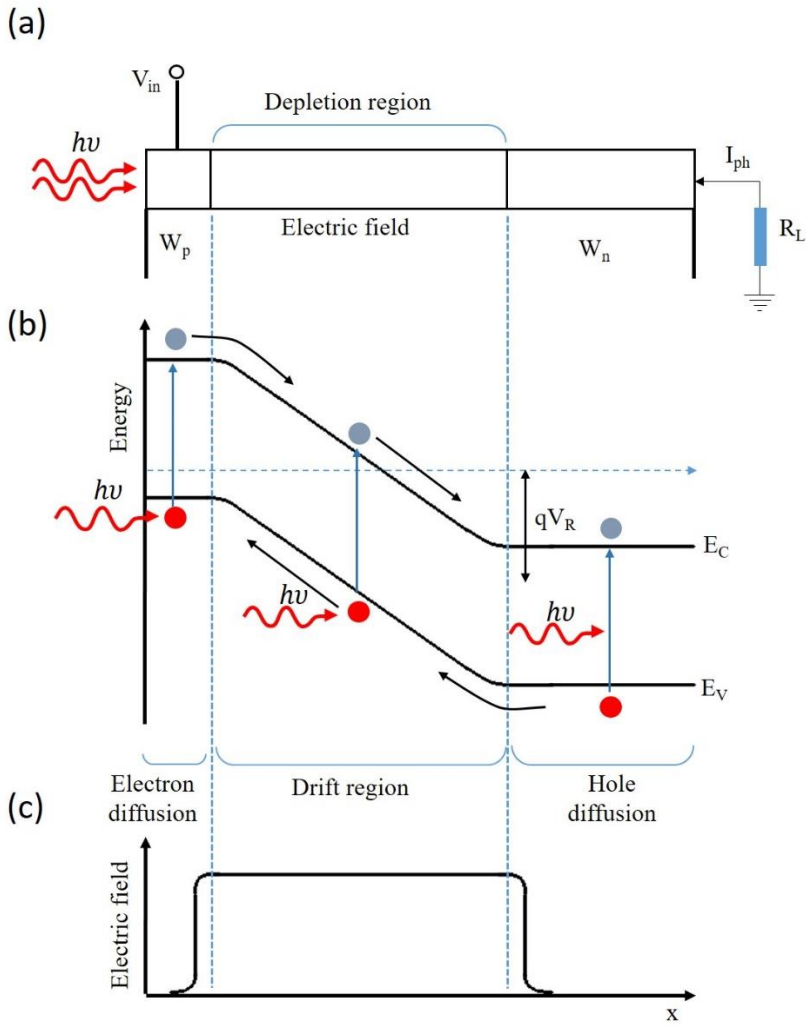

Figure 5.8. Pin diode detector structure (redrawn from ref. [2]).

The absorber layer in the pin detector structure is intrinsic or lightly doped. The constant electric field created by fix charges in the region, where the intrinsic

absorber layer contacts with the p- and n- layers, sweeps the photo-generated carriers with saturation velocity to the contacts, and therefore the absorber layer remains completely depleted. Due to the high electric field in the absorber region, this detector structure has higher quantum efficiency and higher speed than the basic pn junction [2], [17].

As mentioned below, in terms of pixel fabrication, there are two different structures: planar and mesa.

5.3.2 Planar Pixel Structure

In a planner pixel fabrication, the p-type doped region in the pixel structure is created by diffusion after the epilayer growth (Figure 5.9). This method contains fewer steps when compared to the mesa structure in terms of fabrication, and since there are no sidewalls of the pixels in this structure, surface recombination and surface leakage current are not generated. Therefore, the dark current in this structure is very low. However, since there is no physical gap separating the pixels, the crosstalk mechanism reduces the image quality and prevents the production of FPA with a small pitch size. In addition, planar architecture is not a suitable pixel structure for dual or multi-band detectors [17].

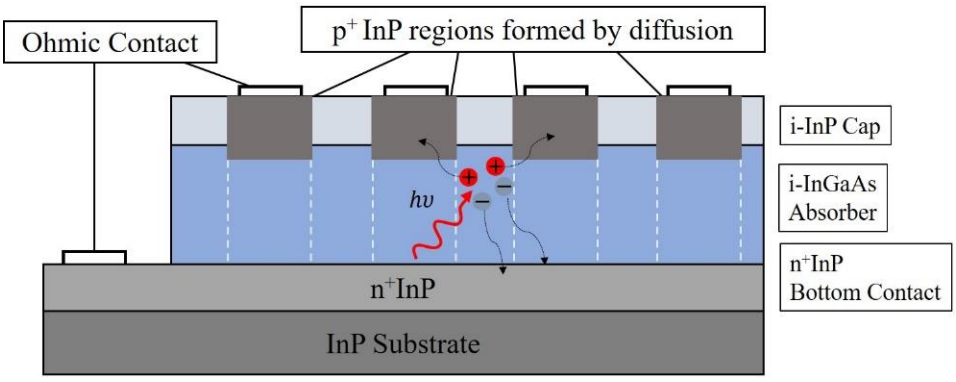

Figure 5.9. Planar pixel structure (redrawn from ref. [17]).

5.3.3 Mesa Pixel Structure

In this structure, the p-type and n-type layers are obtained epitaxially during crystal growth. Pixel structures are created via lithography and etching; however, due to the etching process, dangling bonds that appear on the sidewalls of the pixel cause recombination and surface leakage currents (Figure 5.10). Dielectric passivation is applied to suppress the surface dark current. The crosstalk effect is suppressed because isolation between the pixels is achieved in this structure. Thus, better quality images, smaller pitch size FPAs and dual-band detectors can be obtained with the mesa pixel structure. In this thesis, it has been shown that surface leakage current can be suppressed, and a dual-band detector structure can be achieved with the applied nBn structure.

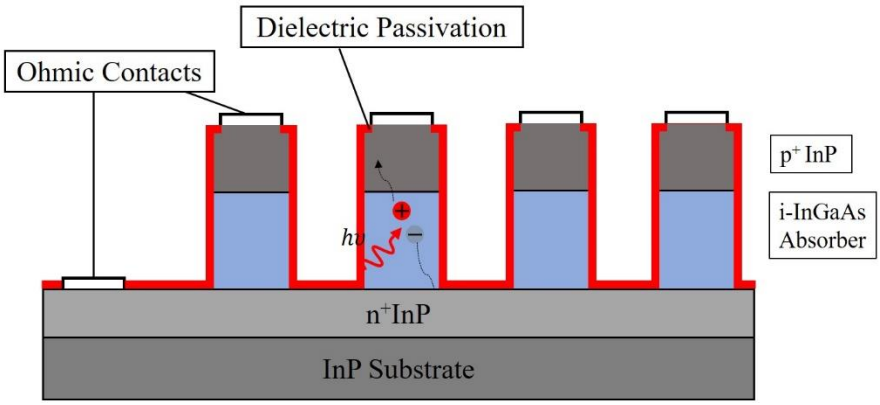

Figure 5.10. Mesa pixel structure (redrawn from ref. [17]).

5.4 InGaAs Unipolar Barrier Infrared Detectors

5.4.1 All InGaAs Unipolar Barrier Infrared Detectors

In this study, Al/Sb free all InGaAs unipolar barrier nBn detectors have been numerically designed by using the graded layers with delta-dopings. Comparison with conventional heterojunction detectors results that there is at least one order of magnitude improvement in dark current without compromising any photoresponse performance. Detailed simulation characterization studies, including sensitivity analysis with respect to the design parameters, verify the robustness of these structures.

5.4.1.1 Method

The main purpose here is to construct an Al/Sb free nBn structure via changing the mole fractions in the $In_xGa_{1-x}As$ material system and obtain superior characteristics compared to the traditional pn junction. Figure 5.11 (a) and (b) show the conventional pn heterojunction schematic and epilayer structure where $In_xGa_{1-x}As$ is lattice-matched to InP substrates at x = 0.53 and p layer is InP in order to take advantage of high bandgap material [98]. As mentioned above, even though this structure is commonly used, the passivation of depleted InGaAs is a big challenge [99] and a structure with no depletion region will be highly desired.

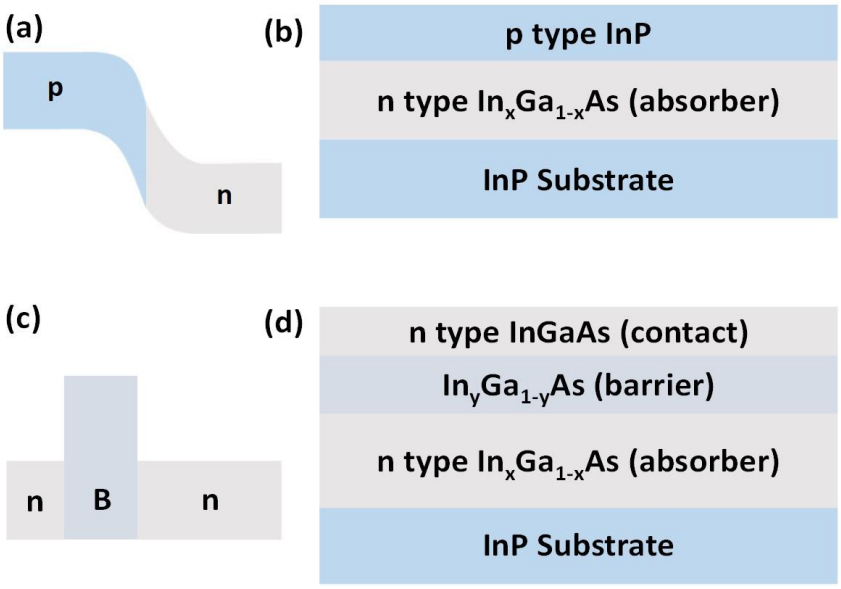

Figure 5.11. (a) and (b) Schematic representation and epilayer structure of InGaAs/InP heterojunction detector design. (c) and (d) Schematic representation and epilayer structure of hypothetical all InGaAs nBn detector design.

Furthermore, Figure 5.11 (c) and (d) illustrate the hypothetical band diagram and the corresponding epilayers for an nBn design. Since there is almost no depletion region, the G-R rate will be low and surface leakage for the majority carriers will be prevented due to the barrier in the conduction band. Therefore, dark current can be minimized and high signal-to-noise and detectivity values can be obtained. Design in Figure 5.11 (c) and (d) is indeed ideal; however, it is not practical due to the fact that inserting a wide bandgap InGaAs barrier immediately after the absorber layer is practically not possible. There will be lattice mismatch between the absorber/contact InGaAs and the barrier InGaAs. In addition, an un-doped barrier will not be placed directly on the conduction band and will exist in the valence band as well, which will lead to minority carrier blocking and affect the responsivity of the detector severely. The solution for these issues is discussed below with the help of numerical calculations performed by using Synopsys Sentaurus TCAD device simulator [84].

5.4.1.2 Device Structure

In order to minimize the effects of lattice mismatch introduced by the high bandgap barrier, InGaAs grading layers need to be inserted for a smoother transition, as shown in Figure 5.12 (a). This method is quite a common way to extend the cutoff wavelengths of SWIR detectors [100]. The band diagram for the structure in Figure 5.12 (a) is presented in Figure 5.12 (b) where the mole fraction is varied without any extra adjustment.

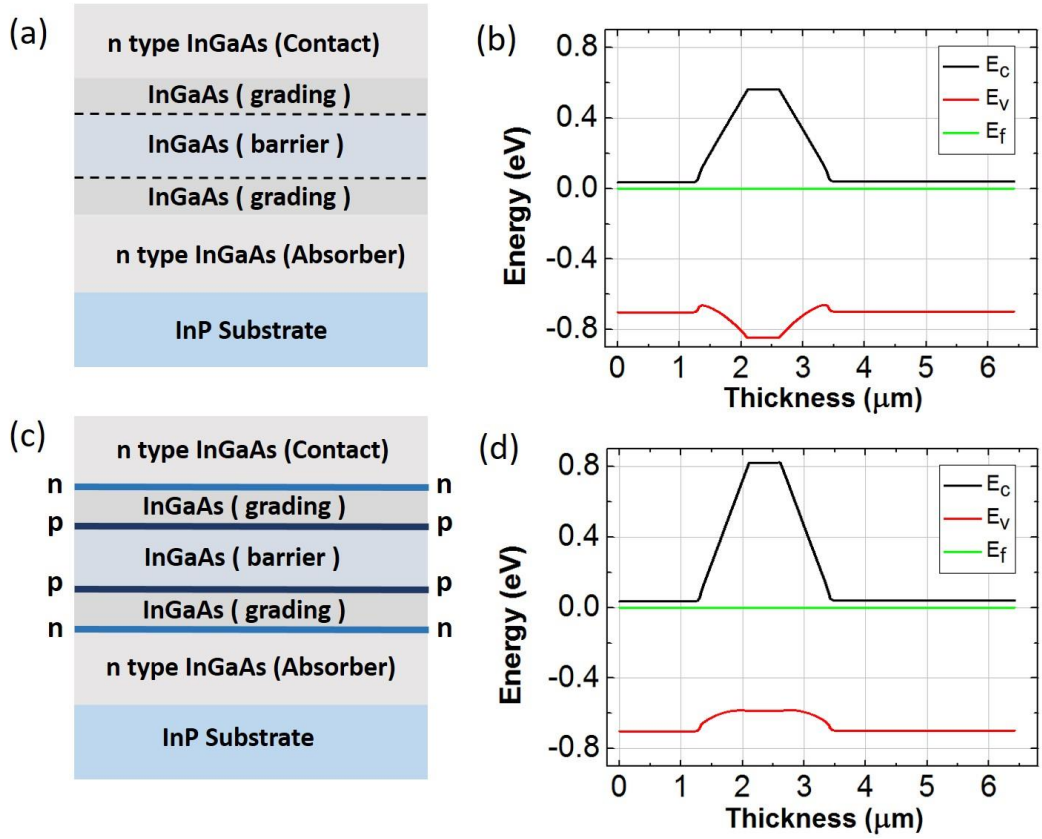

Figure 5.12. (a) and (b) epilayer structure and band diagram of a graded barrier InGaAs nBn structure with valence band barrier. (c) and (d) epilayer structure and band diagram of InGaAs nBn structure with additional delta-doped layers for fixing the valence band offset.

The resulting structure is not useful in this form, as it will block both majority and minority carriers simultaneously due to the barriers in both conduction and the

valence bands. If the graded layers are n-type doped, a unipolar barrier layer can be constructed by only varying the bandgap of the material. However, this barrier layer will block minority carriers [39]. In addition, the p-type barrier does not produce a complete solution, as explained above. As an alternative, the same method that was used for the elimination of conduction band offset in a double heterojunction bipolar transistor study [77] can be utilized. In particular, two pairs of opposite delta-doped layers which form electric fields suppressing the quasi-electric field generated from the bandgap variation can be placed together with the graded layers so that the valence band discontinuity is removed. This method was also used in a pn junction with a barrier structure by using InAlGaAs graded layer and proved to be successful in decreasing the dark current [75]. However, the depletion region still exists in that structure and generation–recombination mechanisms are active. Moreover, maintaining Al source and quaternary structures for the growth can be challenging, similar to the case mention above [51]. Therefore, an nBn design consisting of all InGaAs layers can lead to further improvement.

The Al/Sb free InGaAs nBn detector pixel structure and the corresponding band diagram are shown in Figure 5.12 (c) and (d) [101]. As can be seen, there is almost no depletion region and band bending. The design mainly includes InP lattice-matched absorber ($N_d = 5\times10^{16}$ cm^{-3}), contact ($N_d = 6\times10^{16}$ cm^{-3}), high bandgap barrier (un-doped), linearly compositional graded (un-doped), and dipole delta-doped ($N_d = N_a = 5\times10^{16}$ cm^{-3}) layers. The quasi-electric field that emerged from the compositional grading is balanced with ionized impurities of delta doping layers in order to remove the valence band discontinuity [75], [77], [80].

In terms of the practical considerations, the barrier and compositionally graded layers can be assumed to be lightly doped with a particular background doping concentration. In that case, the delta-doping concentrations can be adjusted such that valence band discontinuity is again eliminated, which indicates the flexibility of this method.

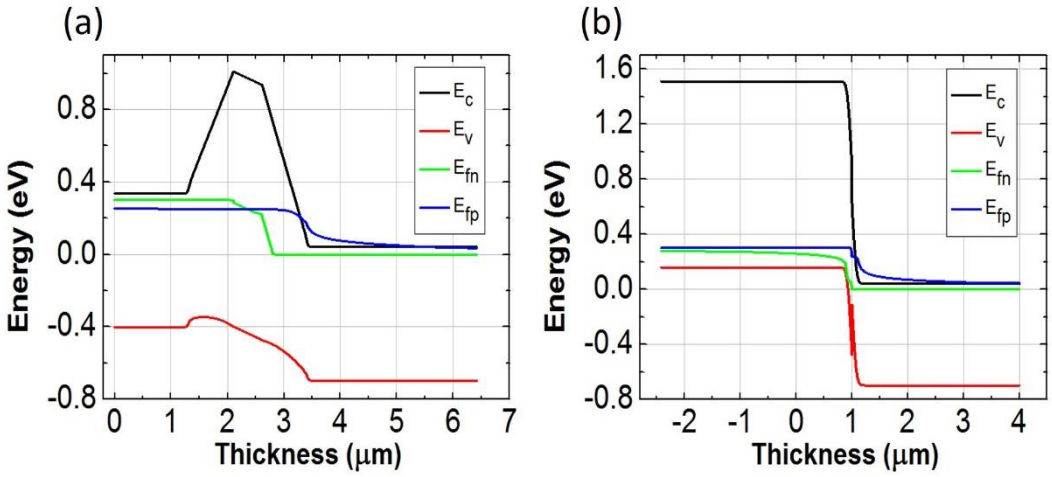

Figure 5.13. The reverse-biased band diagram for both the valence band suppressed nBn design and the traditional pn heterojunction structures.

As seen in Figure 5.13, reverse-biased InGaAs nBn only has conduction band barrier and valence band offset was eliminated by properly inserting delta-doped layers in graded region. On the contrary to InP/InGaAs detector, InGaAs nBn detector has minimal depletion region, which is crucial for suppressing generation–recombination currents.

5.4.1.3 Results and Discussions

As the main purpose of the nBn unipolar barrier detectors are to reduce the dark current density without disrupting the photogenerated carriers, both the designed InGaAs nBn detector composing of only InGaAs material and the conventional InP/InGaAs pn heterojunction were simulated under the same conditions. In terms of the dark current components, Auger, SRH, and surface recombination mechanisms were taken into consideration for both configurations.

The tunneling current is not included since it is negligible at low doping and low bias voltages in lattice-matched InGaAs pn detectors [102]. Surface leakage current was modeled by surface recombination velocity, which specifies the recombination rate at the surface of the structure.

Typically, the surface recombination velocity is less than 10^6 cm/s in $In_{0.53}Ga_{0.47}As$ [88]. Here, both the valence band suppressed nBn structure and the conventional pn heterojunction are analyzed under various surface velocity values in order to observe the dark current characteristics of the devices under different surface conditions. Furthermore, photocurrent analysis is crucial in order to make sure there is no deterioration in the responsivity of nBn detector compared to the heterojunction detector. The absorption coefficient of $In_{0.53}Ga_{0.47}As$ at 1.55 μm is known as 7000 cm^{-1} [2]. The optical simulations were mainly performed at 1.55 μm under 0.01 W/cm^2 optical power per unit area in the parallel direction to the epitaxial structure normal. Then, wavelength sweep has also been applied in order to compare the spectral responsivity of the devices.

5.4.1.3.1 Space Charge, Electric Field, and SRH Rate Comparison

Figure 5.14 (a) and (b) show the schematics of the devices compared and in Figure 5.14 (c) and (d), numerical simulation for space-charge regions in reverse biased nBn and pn detectors are presented. At the interfaces between graded regions and n-type layers, a depleted space-charge region is formed due to the depletion of the n-dopants in the un-doped graded region at the interface. As the doping levels are similar, charge densities for both structures are on the same order as expected.

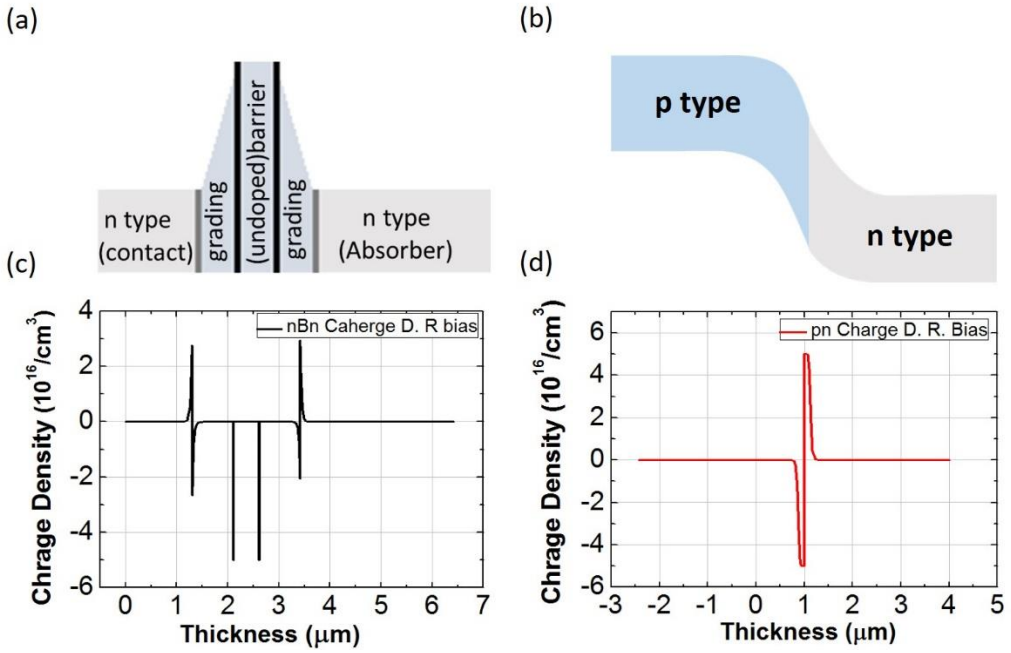

Figure 5.14. Schematic representations of band structure of (a) InGaAs nBn and (b) InP/InGaAs pn. Space-charge density distribution of (c) InGaAs nBn and (d) InP/InGaAs pn.

Furthermore, Figure 5.15 (a) and (b) illustrate the calculation of electric field distribution of reverse biased nBn and pn detectors.

The electric field in the simulated devices here is too low to cause velocity-saturation of the carriers [92]. This result shows that the drift-diffusion model is suitable for this study.

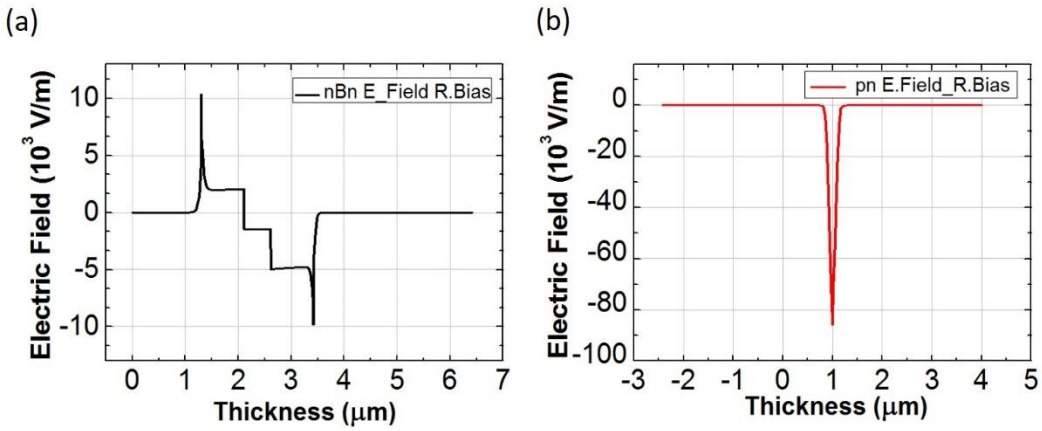

Figure 5.15. Electric field distribution of (a) InGaAs nBn and (b) InP/InGaAs pn.

The electric field for the pn junction is much higher than for the nBn detector due to the nature of the reverse-biased diode and these results in higher rates of SRH thermal generation. Consequently, a higher dark current is expected to be experienced.

When SRH generation and recombination rates for nBn and pn heterojunction photodiode are analyzed (Figure 5.16 (a) and (b)), SRH rate in the nBn detector is much smaller than SRH rate of conventional InP/InGaAs pn detector. These results suggest that the applied nBn design can provide smaller dark current and has an important potential to improve the noise characteristics of the SRH limited detectors.

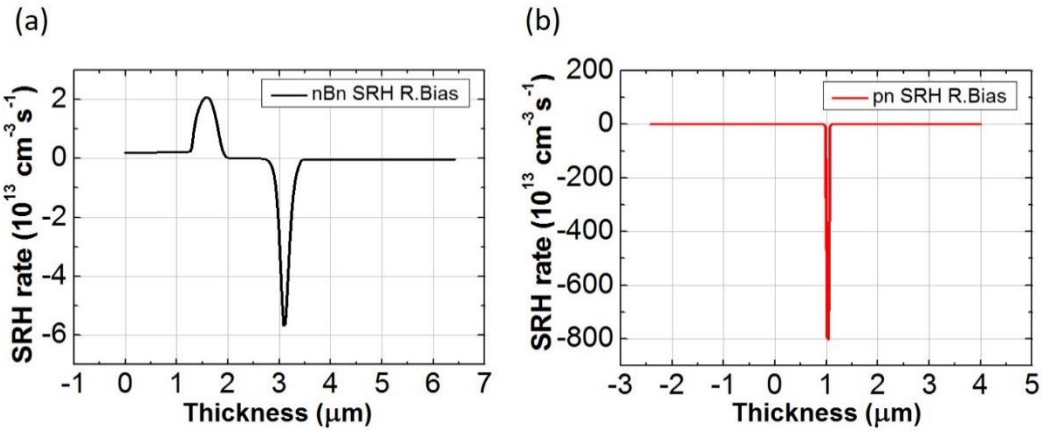

Figure 5.16. SRH rate distribution of (a) InGaAs nBn and (b) InP/InGaAs pn. There is more than one order of magnitude difference between the two designs indicating the importance of avoiding the depletion layer.

5.4.1.3.2 Dark Current Characterization

In Figure 5.17 (a), total dark current values with respect to changes in surface recombination velocity up to 10^6 cm/s with 10 μs SRH lifetime are presented for both structures with 25×25 μm^2 detector size under −0.1 V bias voltage. As can be seen, even though the total dark current is approximately the same under 10 cm/s surface velocity (no surface current), increasing surface velocity increases the dark current in pn heterojunction structure significantly due to the high electric field.

However, the barrier located at the conduction band for the nBn detector does not easily allow the electrons created at the surface to reach the contact. Hence, only the holes flowing through the surface contribute to the dark current, which yields around two order of magnitude less dark current compare to the pn heterojunction case. Surface velocity values here are chosen from the variety of studies in [88] and results clearly indicate the elimination of the need for surface passivation.

Furthermore, in Figure 5.17 (b), the result of the surface velocity scan calculations under 1 ns SRH lifetime is presented and the substantial dark current suppression for the nBn case is again observed. For the pn heterojunction, the dark current values are more than one order of magnitude higher. The major difference between the two structures this time comes from the generation-recombination components until the surface velocity reaches to 10^6 cm/s. This considerable decrease in the dark current is due to the minimal depletion region and the lower magnitude of the electric field for the nBn structure.

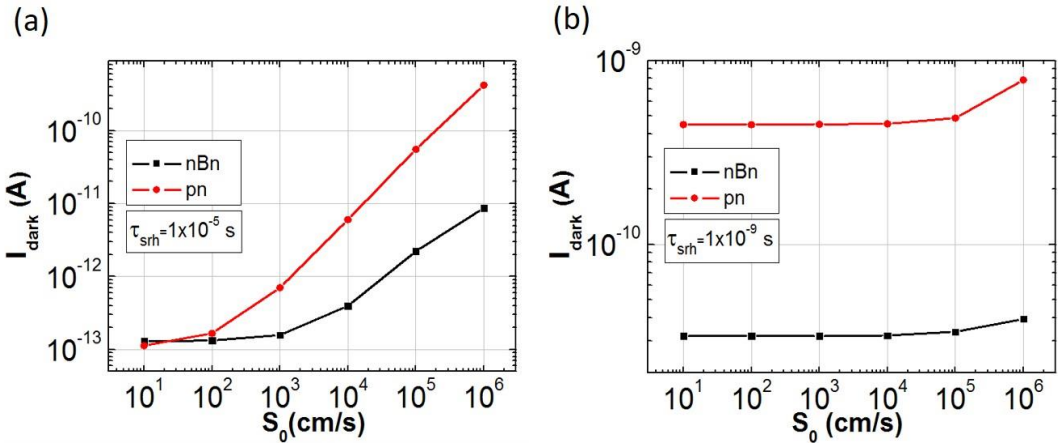

Figure 5.17. (a) and (b) Calculation of total dark current with respect to the change in surface recombination velocity at $\tau_{srh} = 1\times10^{-5}$s and $\tau_{srh} = 1\times10^{-9}$s for both nBn and pn structures.

As a result of the analysis in Figure 5.17 (a) and (b), the applied nBn structure is expected to provide superior results compared to the traditional pn heterojunction

detectors except for the very high-quality material and extremely good passivation in which case, they have the same performance.

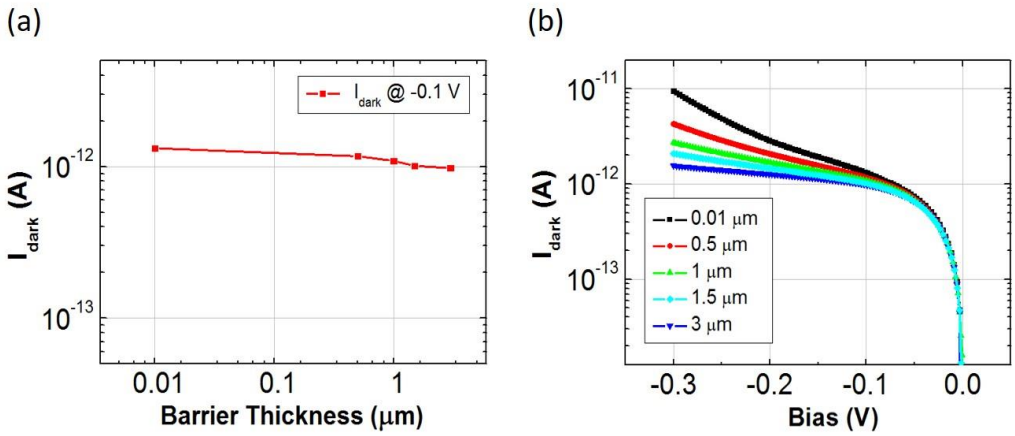

Figure 5.18. (a) Dark current versus un-doped InGaAs barrier thickness at 0.1 V. (b) I-V characteristics of the nBn detector at difference un-doped InGaAs barrier thickness.

Moreover, the variation in total dark current at −0.1 V coming from the barrier thickness has been summarized in Figure 5.18 (a) with SRH lifetime and surface velocity values taken from previous studies ($\tau_{srh} = 4.74\times10^{-5}$ s [89] and $s_0 = 4.5\times 10^4$ cm/s [88]). As a result, the dark current is decreasing with the increasing thickness of the barrier as expected. When the same analysis has been performed for increasing reverse bias voltages, the results in Figure 5.18 (b) have been observed. Higher bias voltages increase dark current, especially for smaller barrier thickness. Barrier thickness may be the most critical layer in the material growth and based on these results, 0.5 μm barrier thickness seems to be a good value for −0.1 V operating point.

5.4.1.3.3 Dark Versus Photocurrent I–V

In Figure 5.19 (a) and (b), total dark current and photocurrent of nBn and pn type detectors were presented. Calculated dark current for the conventional pn heterojunction is similar to the recently reported experimental values for the mesa-type detectors [103].

Comparison in Figure 5.19 (a) shows that nBn detector provides 21 times lower dark current at the target bias point of −0.1 V. As explained above, this improvement is due to the superior performance nBn on suppressing surface currents and almost nonexistence of inherent G-R current.

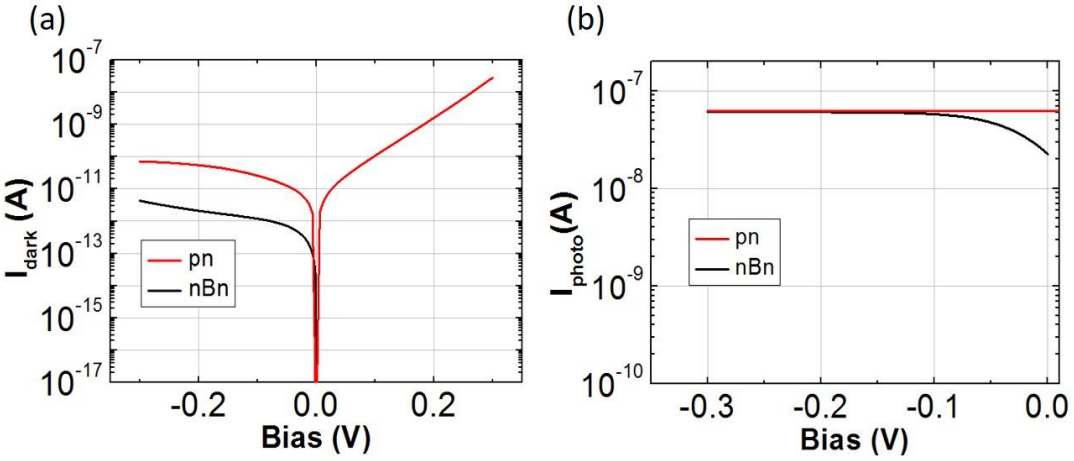

Figure 5.19. Dark (a) and photocurrent (b) comparison of nBn and pn detectors at 500 nm barrier thickness and s_0 = 4. 5×10^4 cm/s, τ_{srh} = 4. 74×10^{-5}s.

As an alternative way to model the surface leakage current, the surface trap characteristics of each layer has been defined instead of surface velocity values as well. In this method, by following the experimental studies, InGaAs surfaces were treated to have As vacancies which behave like acceptor-like trap states and tend to be occupied with electrons (charged negatively) [27], [104]–[106]. Trap densities at the material surfaces have been obtained using the space-charge densities at the interfaces by following the methodology used for conventional pn junctions [90], [107] and assuming that background doping concentration of un-doped regions will be 10^{14} cm^{-3}. Capture cross-sectional values for electrons and holes are chosen as 10^{-14} cm^2 for both InP and InGaAs [105]. The surface Fermi level is generally pinned to the midgap in InP [108] whereas it is pinned at around 0.5 eV above from the valence band for n-InGaAs material with high In mole fractions (absorber here) and at midgap with low mole In fractions (barrier here), [27], [105], [106]. As a result of the calculations with these parameters, both types of detectors (the applied nBn

design here and conventional pn heterojunction) showed an increase in the total dark current by ~ 1.5 times resulting in a total dark current suppression of 25 times in the advantage of the all InGaAs nBn detector. In the next section, Fermi level pinning will be covered more comprehensively for InGaAs nBn and InP/InGaAs pn structures.

As dark current suppression alone is not enough for better overall performance without making sure that the photoresponse is not degraded, responsivity and quantum efficiency of the detectors are also compared. The light source here has 0.01 W/cm^2 radiation at 1.55 μm wavelength with 7000 cm^{-1} absorption coefficient [2].

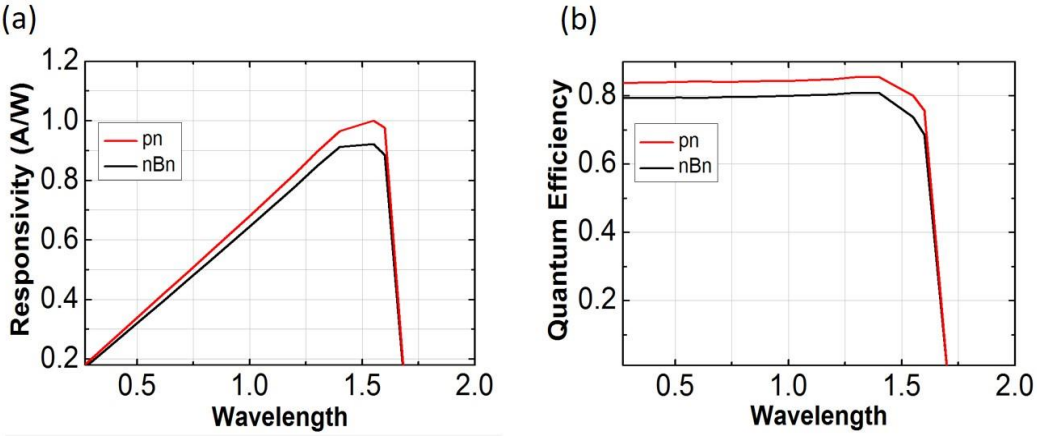

Figure 5.20. (a) Responsivity of nBn and pn detectors. (b) Quantum efficiency of nBn and pn detectors at −0.1 V.

Results are presented in Figure 5.20 where both structures have almost the same photocurrent. From the calculated photocurrent values in Figure 5.20 (a), the quantum efficiency is calculated to be more than 80% for both structures. Furthermore, spectral responsivities are also simulated by varying the input source wavelength and the obtained results are still quite similar, as seen from Figure 5.20 (b). Finally, the same photocurrent analysis has been performed at very low optical powers imitating the nighttime imaging conditions (around 4×10^{-7} W/cm^2 radiance [109]) as well. In the analysis where the operating point for

the detectors has been cooled down in order to suppress the dark current completely for both cases and isolate the photocurrent, the calculated photocurrents were still almost the same.

5.4.1.4 Fermi Level Pining Effect Calculations

Generally, InGaAs surface has been reported to have As vacancies which behave as acceptor-like trap centers [27], [105]. Acceptor-like states tend to be occupied with electron and charged negatively [104], [106]. Therefore, negative surface charges are accumulated at InGaAs surfaces, which indicates the n-type inversion of the surfaces. In the initial calculations, it was used as a mathematical model included in the Synopsys Sentaurus TCAD software that directly formulizes the surface SRH recombination rate as the following equation and does not take traps' behavior into consideration.

$$R_{net}^{SRH\ surf} = \frac{np - n_i^2}{(n + n_1)/s_0 + (p + p_1)/s_0} \tag{5.1}$$

this equation, s_0 is the surface recombination velocity, n and p represent the carrier concentrations and n_1 and p_1 are taken equal to intrinsic carrier distribution, which means the energy trap level is in the middle of the bandgap. Thus, in these simulations, it was assumed that there occurs a channel allowing the flow of carriers at the surfaces, and modelled the surface current by using the equation above. Various surface leakage current levels were obtained by directly inserting the surface recombination velocity value into the formula, which is actually the product of the density of traps (cm^{-2}), thermal velocity (cm/s) and capture-cross section (cm^2). However, this method does not model the behavior of the surface traps physically, and the surface generation-recombination rate is linked to the traps implicitly.

Alternatively, Synopsys Sentaurus TCAD software also allows to model the surface traps instead of defining a surface recombination velocity and it was implemented this modelling as well for further investigation. In this method, it can be

characterized the surface traps in terms of trap type (donor-like or acceptor-like behavior), trap energy level position in the bandgap (eV), trap density (cm^{-2}), hole and electron capture cross sections (cm^{-2}). As stated in [106] and [104], donor-like traps are positively charged when unoccupied and they become neutral by capturing an electron, and acceptor-like traps are neutral when unoccupied and they are negatively charged when filled with an electron. Table 5.1 summarizes the interface trap behaviors that are found to exist in InGaAs and InP materials experimentally [27].

Table 5.1 Missing Atoms at InGaAs and InP Surfaces

Deficiency	Trap Behavior
In in InGaAs	Donor-like
Ga in InGaAs	Donor-like
As in InGaAs	Acceptor-like
In in InP	Donor-like
P in InP	Acceptor-like

Trap density at the material surface depends on the donor or acceptor density in the depletion width, as stated in [27], [90]. By making use of the surface trap density vs. doping concentration plot and calculation procedure in [90], it was calculated the surface trap density of both pn and nBn detectors by determining the depletion width in each device from the space charge density distribution graph provided in Figure 5.14 (c)-(d) and assuming that background doping concentration of un-doped regions will be 10^{14} cm^{-3}. The resulting surface trap densities are provided in Table 5.2.

Table 5.2 Calculated Surface Trap Density of each Layer of each Device

pn Heterojunction Detector	Surface Trap Density (cm^{-2})	nBn Detector	Surface Trap Density (cm^{-2})
n-InGaAs Absorber	6×10^{11}	n-InGaAs Absorber	4.7×10^{11}
p-InP	6×10^{11}	Delta Doped Layers	4.7×10^{11}
-	-	InGaAs Barrier	9.2×10^{8}
-	-	Grading Layers	1×10^{9}
--	-	n-InGaAs Contact	5.64×10^{11}

Also, capture cross-section values for electrons and holes are chosen as 10^{-14} cm^2 for both InP and InGaAs [27] . The surface Fermi level is generally pinned to the mid of the bandgap in InP, as reported in [107]. In experimental observations about the pinned Fermi level position of InGaAs, it is almost a common finding that the Fermi level pinning occurs due to As vacancy, and trap energy level is located at around 0.5 eV above from the valence band [107]. In addition, a recent study also shares experimental results that report the located trap energy level as 4.8±0.1 eV from the vacuum level and depict the pinning energy level with respect to the mole fraction of gallium as in Figure 5.21 [107].

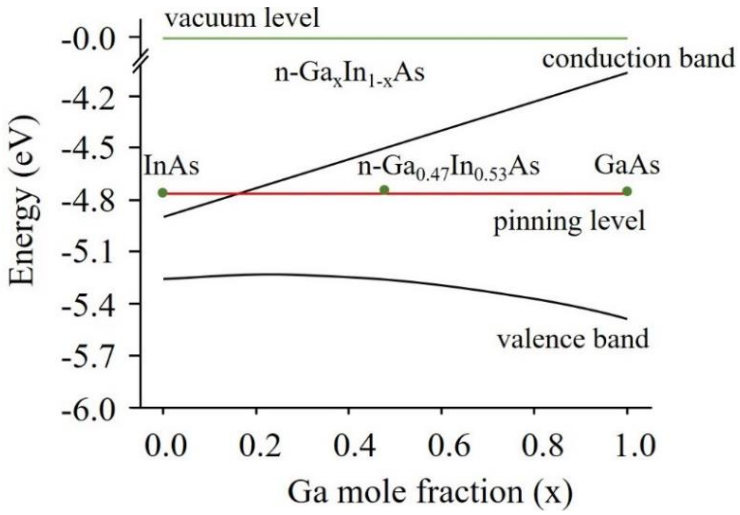

Figure 5.21. Fermi Level Pinning of n type $In_{1-x}Ga_xAs$ Surfaces (redrawn from ref. [107]).

Figure 5.21 states that for n-$In_{0.53}Ga_{0.47}As$ surfaces, surface energy level is pinned around 0.5 eV above from the valence band, and for n-GaAs surfaces, Fermi level pinning starts to occur at the midpoint of the bandgap as the In mole fraction decreases, which almost corresponds to barrier surface considering our case.

According to the mentioned trap parameters above, it was re-simulated both InP/InGaAs pn and InGaAs nBn detectors by defining the trap behavior acceptor-like (As vacancy). The energy band diagrams at the surfaces of InGaAs layers in nBn detector are plotted in Figure 5.22 for the illustration of surface Fermi level pinning.

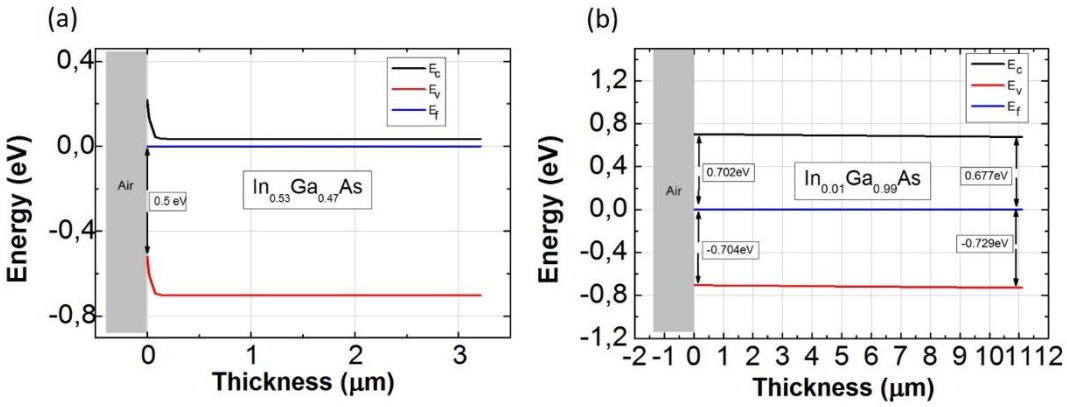

Figure 5.22. Surface Fermi Level Pinning Observation at InGaAs Surfaces of nBn detector.

Figure 5.23 summarizes the dark current values obtained by using the applied surface trap model in comparison with the surface recombination velocity model used in Figure 5.19 (s_0=4.5×10^4 cm/s and τ_{SRH} = 4.74×10^{-5} s). In both detectors, a little bit of increase in dark current was observed at the target bias point of −0.1 V. However, the reduction coefficient in dark current (21 times with surface recombination model) did not really change and it reached to 25 with surface trap density modelling. Furthermore, it was swept the energy trap levels in grading layers from −0.6 eV to +0.6 eV around the mid-gap since the linear variation of mole fraction in these layers prevents us from defining certain energy trap levels. It is observed no difference in dark current with the energy trap level sweep in grading layers as the surface current dominated by the absorber layer due to the high doping concentration (Figure 5.23).

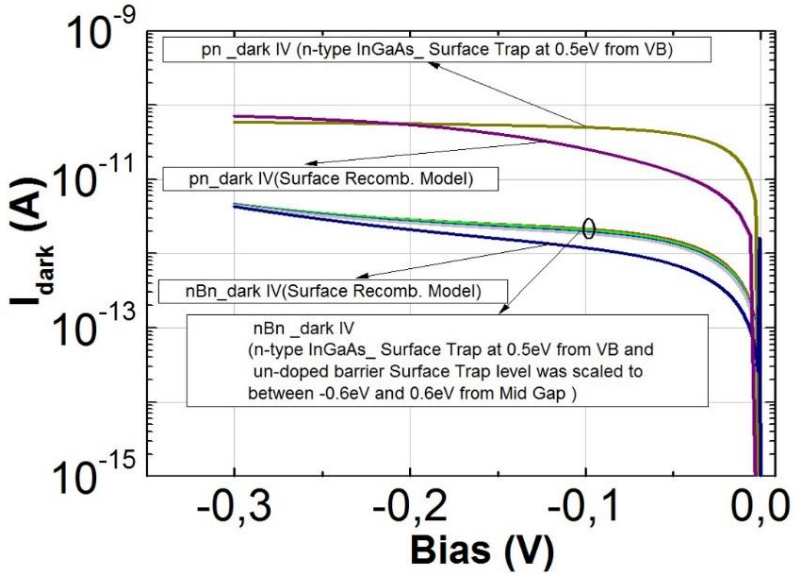

Figure 5.23. pn and nBn Detector Dark Current Level Comparison for both Surface Recombination Velocity Model and Surface Trap Model.

In summary, it has been concluded that modelling of the surface pinning does not materially change the results as it would be expected from an nBn design.

5.4.2 InGaAs nBn SWIR Detector Design with Lattice-matched InAlGaAs Barrier

In this work, InGaAs nBn detector design has been realized by utilizing lattice-matched un-doped InAlGaAs grading layers with delta-dopings. Here, un-doped InAlGaAs grading layers are used in constructing the barrier and dipole delta-doped layers are placed in both sides of the graded layers for eliminating valence band offset. As a result, the high bandgap barrier layer blocks the majority carriers and allows minority carrier flow while minimizing various dark current components, as expected from an nBn detector. Substantial improvement has been shown in the dark current level without compromising any photoresponse compared to the conventional pn junction and all InGaAs nBn type photodetector which was shown in section 5.4.1.

5.4.2.1 Method

In order to construct a high bandgap barrier layer, $In_{1-x-y}Al_xGa_yAs$ quaternary compound graded from InGaAs to InAlAs is utilized while maintaining x+y=0.47 to preserve the lattice constant [110]. Figure 5.24 represents the band diagram of this structure with no additional adjustment where there are both conduction and valence band barriers leading to a minority barrier in addition to the desired majority carrier barrier.

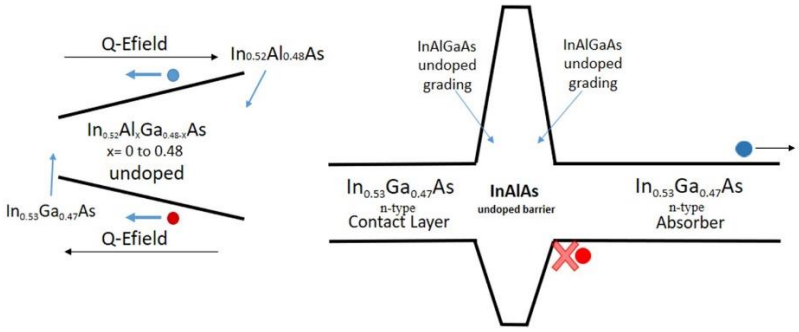

Figure 5.24. Schematic band diagram of the valence band for uncompensated graded InAlGaAs barrier InGaAs nBn detector.

In order to fix the minority carrier barrier, n-type and p-type delta-doped layers are placed at the sides of the graded layers. Consequently, the valence band quasi-electric field has been canceled and the valence band offset is suppressed, resulting in an almost ideal nBn detector profile, as shown in Figure 5.25.

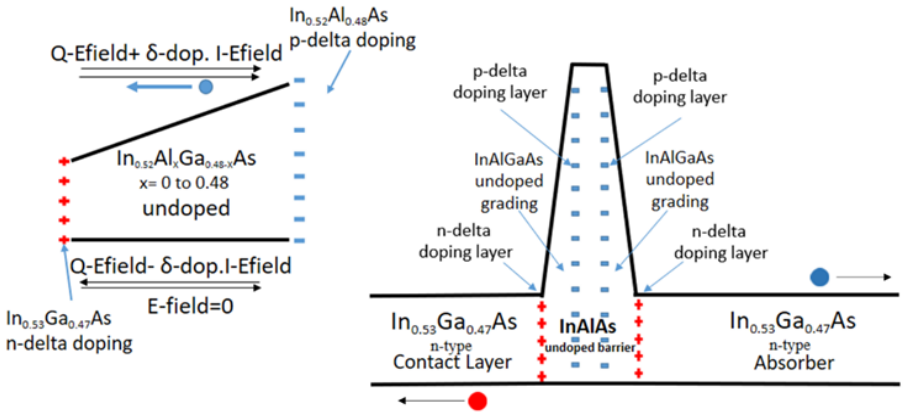

Figure 5.25. Schematic band diagram of the valence band for uncompensated graded InAlGaAs barrier InGaAs nBn detector.

5.4.2.2 Device Structure

This methodology is the same as that for section 5.4.1. However, as illustrated in Figure 5.26, having lattice-matched layers will result in better quality material with a shorter material growth time by removing the need for relatively longer grading layers that are necessary to minimize the effects from lattice-mismatch.

As shown in Figures 5.26 (a) and 5.26 (b), the regular pn junction has a depletion region and various dark current mechanisms are maximized at the depletion region. Figures 5.26 (c) and 5.26 (d) represents the all InGaAs nBn structure where relatively thicker grading structures are required due to the lattice-mismatch coming from the InGaAs compositional grading. However, a similar barrier structure can be achieved without introducing lattice-mismatch in the case of InAlAs barrier layer and InAlGaAs grading layers, as seen in Figures 5.26 (e) and 5.26 (f).

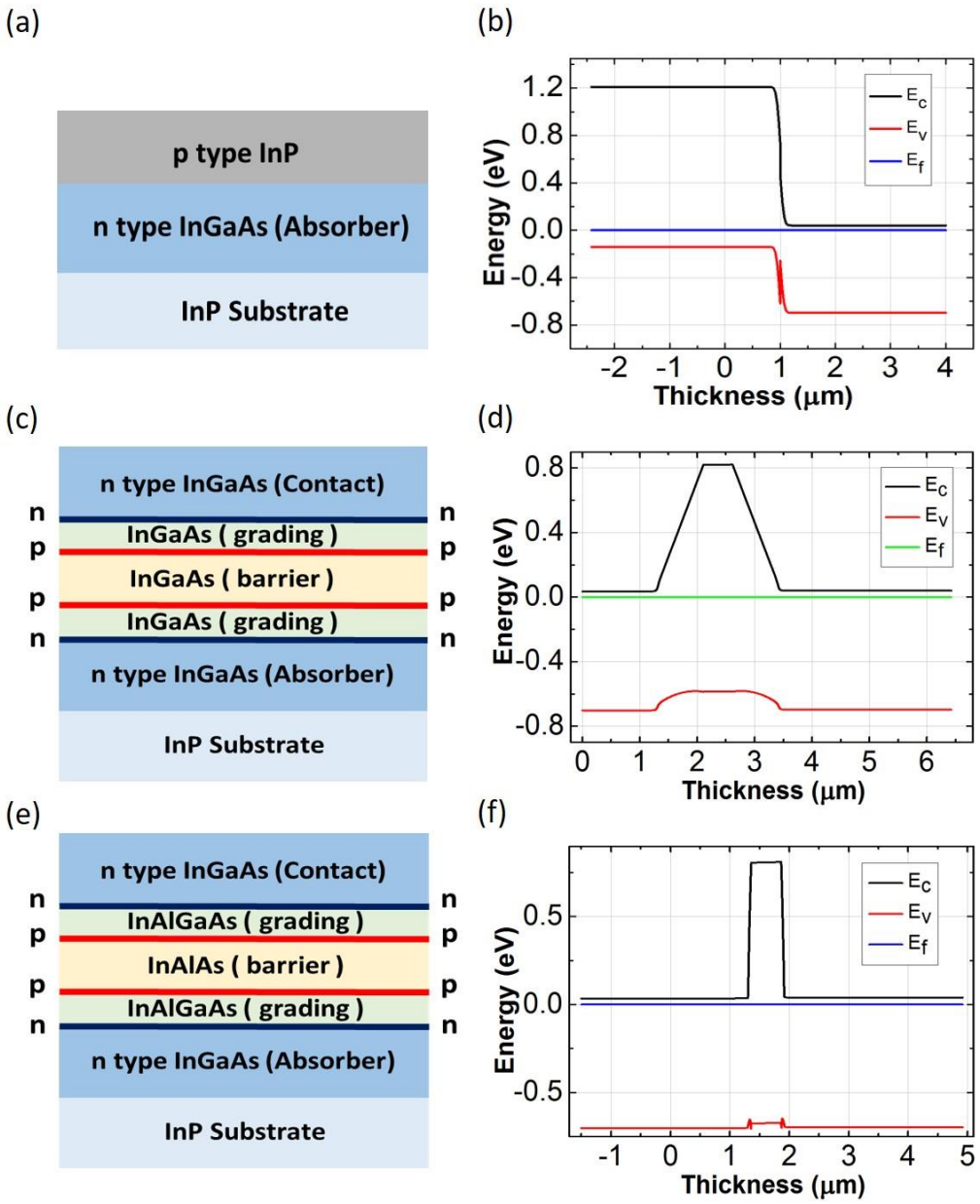

Figure 5.26. Pixel structure and calculated band diagram for ((a), (b)) a pn junction, ((c), (d)) nBn detector with all InGaAs epilayers [110], and ((e), (f)) nBn detectors with lattice-matched graded and delta-doping layers. Absorber layers are 3 μm and detector size is 25×25 μm^2 for all cases.

Barrier layers are 500 nm and delta-dopings are 5 nm for both nBn structures. Grading layer is around 800 nm for the lattice-mismatched case and 50 nm for the lattice-matched case.

Reverse biased band diagram characteristics for the structures shown in Figure 5.26 are presented in Figure 5.27, where Figure 5.27 (a) shows the pn junction ($N_d = 5\times10^{16}$ cm^{-3}, $N_a = 5\times10^{16}$ cm^{-3}) and Figures 5.27 (b) and 5.27 (c) illustrate the nBn structures discussed above. The nBn designs both include an InGaAs lattice-matched absorber ($N_d = 5\times10^{16}$ cm^{-3}), contact layer ($N_d = 6\times10^{16}$ cm^{-3}), high bandgap barrier (un-doped), and linearly compositional graded (un-doped) and dipole delta-doped ($N_d = N_a = 1.1\times10^{18}$ cm^{-3}) layers where the valence band offset is removed with the help of delta-dopings [59], [79], [77], [101], [112]. Doping levels are chosen considering the case where absorber doping up to low 10^{17} cm^{-3} levels has been shown to lower the dark current [113].

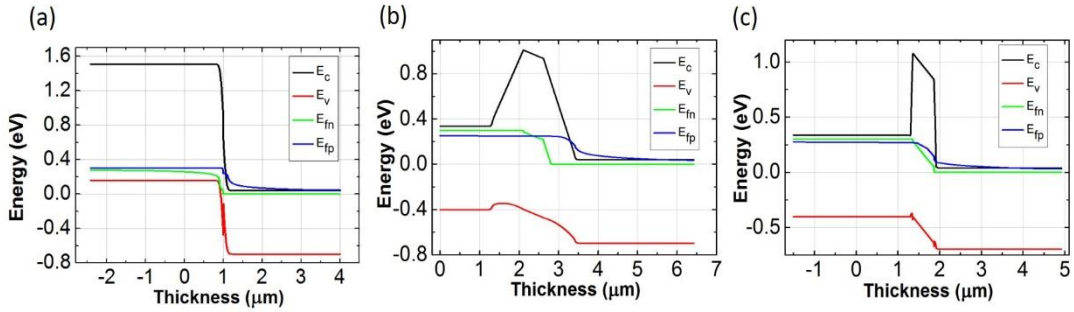

Figure 5.27. Reverse biased band diagrams for the structures shown in Figure 5.26 with a reverse bias of 0.3 V: (a) pn heterojunction, (b) all InGaAs nBn structure, (c) lattice-matched nBn structure.

5.4.2.3 Results and Discussions

Next, dark and photocurrent calculations, including sensitivity analysis with respect to different delta-doping concentrations and various barrier heights adjusted by Al-Ga mole fraction ratio, are discussed for the designed nBn detector. In the simulations, optical calculations were done at 1.55 μm under 0.01 W/cm^2 optical power per unit area in the normal direction to the epitaxial structure from the substrate side (back-illuminated) while the absorption coefficient of $In_{0.53}Ga_{0.47}As$ at 1.55 μm was considered as 7000 cm^{-1} [2], [59].

5.4.2.3.1 Effects of Different Delta-Doping Layer Doping Concentrations

Figure 5.28 (a) shows the dark and photocurrent densities versus delta-doping layer concentrations and Figure 5.28 (b) illustrates the adjustable valence and conduction band offsets with delta-doping layer doping concentrations. At the lower delta-doping concentrations, the valence band barrier blocks the minority carriers; therefore, the detector exhibits lower photocurrent and the dark current is higher since the electrons can flow over the barrier to the absorber with the thermionic emission. When the doping concentrations are increased, the flow of minority carriers is getting easier (photocurrent density increases) due to lowered valence band offset. Simultaneously, the dark current density decreases because of the more efficient blocking of the majority carriers (Figure 5.28 (b)). When delta-doping concentrations are increased to 1.1×10^{18} cm^{-3}, valence band offset is almost completely eliminated and conduction band offset becomes high enough to block majority carrier electrons effectively, leading to the optimum nBn performance characteristics. Furthermore, if the delta-doping concentrations are increased even more, the high electric field causes higher thermal SRH generation and increases the dark current (Figure 5.28 (a)).

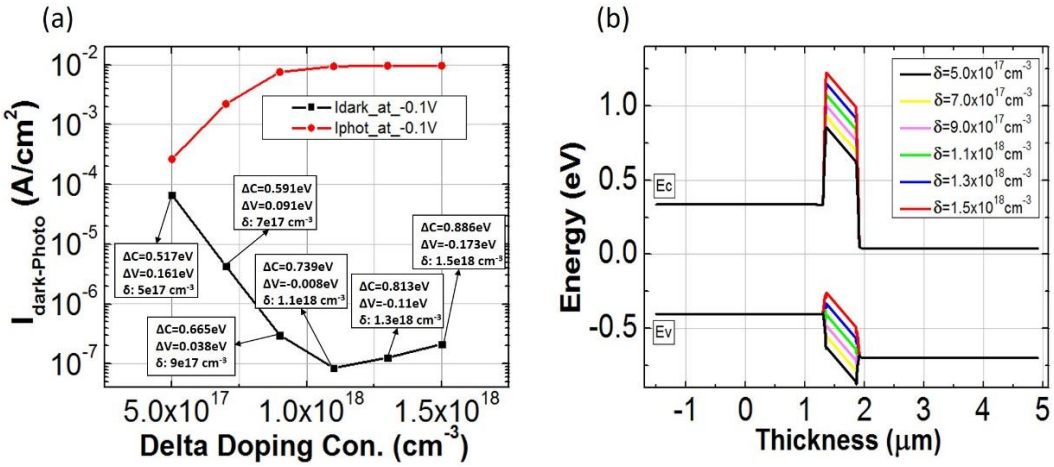

Figure 5.28. Effects of different delta-doping layer doping concentration on (a) photocurrent and dark current densities and (b) band diagram of the nBn detector.

5.4.2.3.2 Effects of The Barrier Height

Figure 5.29 (a) shows the effects of the barrier height coming from the Al-Ga mole fraction ratio change on the dark and photocurrent density characteristics of the designed nBn detectors. Here, the barrier layer is constructed by the compositional grading of InAlGaAs material from InGaAs to various Al-Ga ratios together with the optimized delta-doping concentrations, providing zero valence band offset for each barrier height (Figure 5.29 (b)). At the lower barrier heights (low Al-Ga ratios), majority carriers can overcome the barrier by thermionic emission, so that the dark current becomes higher and the photocurrent is suppressed by the high dark current. When the Al-Ga ratio of the barrier increases, the barrier height increases and the majority carriers are consequently blocked, resulting in a reduced dark current density.

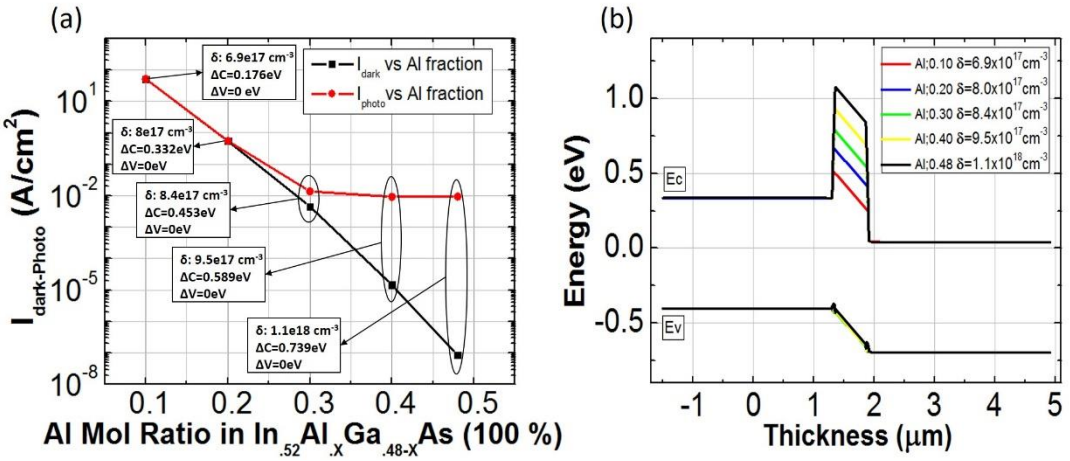

Figure 5.29. Effects of different barrier heights with optimized delta-doping concentrations on (a) photocurrent and dark current densities and (b) band diagram of the nBn detector. ΔV (ΔC) represents the valence (conduction) band offsets.

5.4.2.3.3 Dark Versus Photocurrent I-V

Moreover, in order to visualize the relative performance of the nBn structure, total dark and photocurrent densities of the two nBn designs and the pn heterojunctions

are comparatively analyzed. Results are summarized in Figure 5.30, where Figure 5.30 (a) shows the dark current density comparison and the photoresponse characteristics are seen in Figures 5.30 (b) and 5.30 (c). The bandgap engineered lattice-matched InGaAs nBn detector clearly and conclusively exhibits lower dark current without photocurrent degradation, as expected from an ideal nBn detector. The calculated dark current density for the conventional pn heterojunction is similar to the recently reported experimental values for the mesa type detectors [103].

As a result, around 50 and 2.5 times improvement has been shown in the dark current density level compared to the conventional pn junction and all InGaAs nBn type photodetector, respectively.

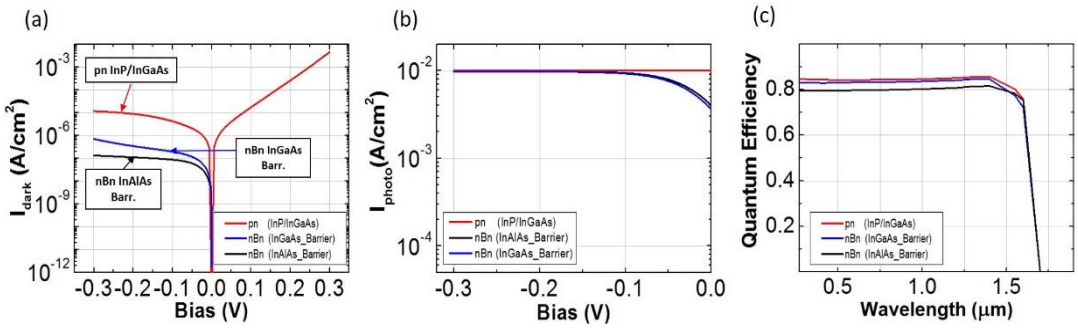

Figure 5.30. Dark and photocurrent density results together with the quantum efficiency values at −0.2 V of lattice-matched barrier InGaAs nBn detector in comparison with conventional InGaAs pn heterojunction detector and lattice-mismatched barrier nBn structure.

The same carrier lifetime and surface recombination velocity values have been used for all structures in the comparison in Figure 5.30 and the calculated dark current density of lattice-matched barrier InGaAs nBn detector structure is getting closer to the record values reported for planar type detectors [114], [115]. Considering the effects of lattice-mismatch on the carrier lifetime, the improvement for the all lattice-matched case compared to the lattice-mismatched case would be even stronger.

5.4.3 InGaAs Shortwave Infrared Dual-Band nBn Detector

The nBn detector architecture can also be designed as dual-band detectors in a variety of different band ranges by utilizing the graded layers with delta-dopings. A schematic representation for an nBn type of barrier detector structure operating in a dual-band configuration is shown in Figure 5.31. When the absorber layer with the cutoff wavelength of λ_1 is positively biased (Figure 5.31 (a)), both the photoelectrons and photo-holes generated in this layer are able to reach contacts and form the photocurrent [11], [61], [116].

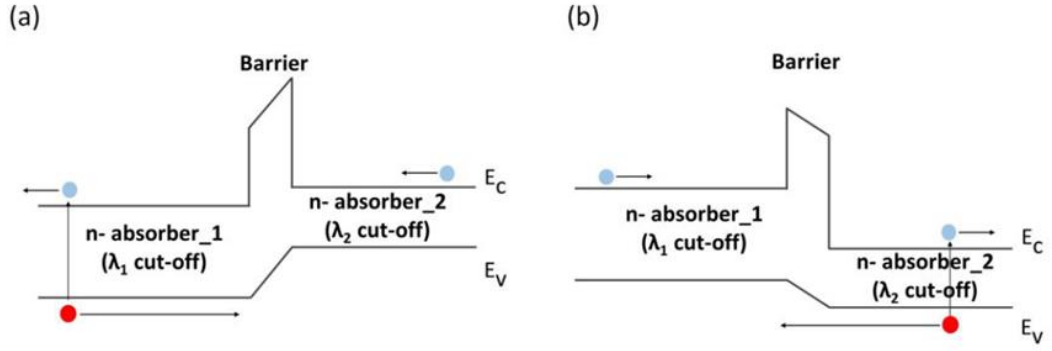

Figure 5.31. Schematic representation of band diagrams of a dual-band nBn detector where (a) the first absorber (λ_1) is under positive bias and (b) the second absorber (λ_2) is under positive bias.

Moreover, if the λ_2 cutoff wavelength absorber layer is positively biased, electrons and holes generated in the λ_2 cutoff wavelength absorber layer contribute to the photocurrent (Figure 5.31 (b)). Therefore, this structure can be used as a dual-band detector in a polarity switchable bias configuration, and the absence of the depletion region may make this dual-band nBn design more advantageous in terms of dark current suppression when compared to the previously demonstrated dual-band structures [117]–[126].

5.4.3.1 Method

The barrier layer of the SWIR dual-band nBn detector is obtained by grading from the low bandgap ($In_{0.53}Ga_{0.47}As$) to the high bandgap ($In_{0.53}Ga_{0.47}As$) of the $In_{0.53}(GaAl)_{0.47}As$ material in accordance with InGaAs (Figure 5.32). One of the n-type absorber layers will be InP lattice match $In_{0.53}Ga_{0.47}As$ (cutoff wavelength of 1.7 µm) material and the other n-type absorber layer will be used $In_{0.83}Ga_{0.17}As$ material with a cutoff wavelength of 2.5 µm.

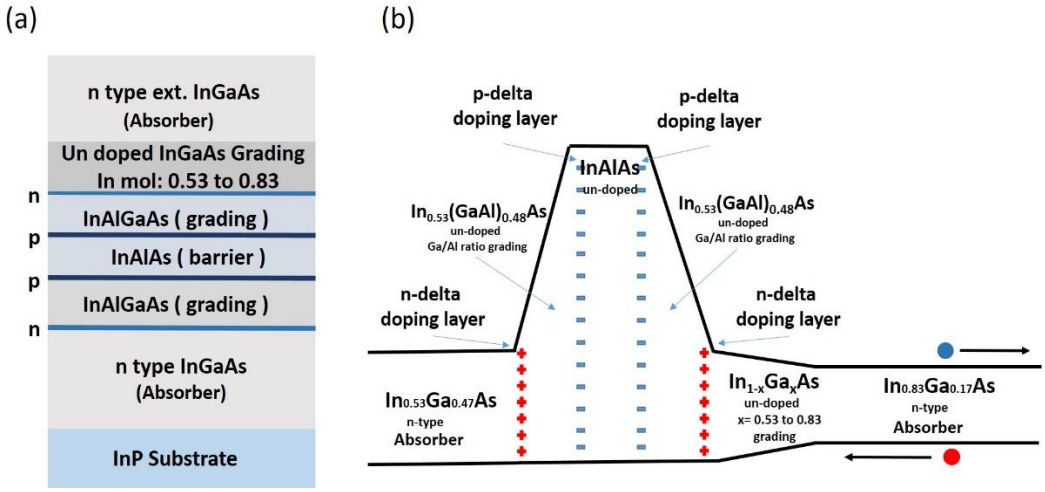

Figure 5.32. The InGaAs dual-band SWIR nBn detector; (a) pixel and (b) schematic band structure.

As seen in Figure 5.32, the $In_{0.83}Ga_{0.17}As$ absorber layer is obtained by grading the In mol ratio of the InGaAs material from 0.53 to 0.83 immediately after the barrier.

5.4.3.2 Results and Discussions

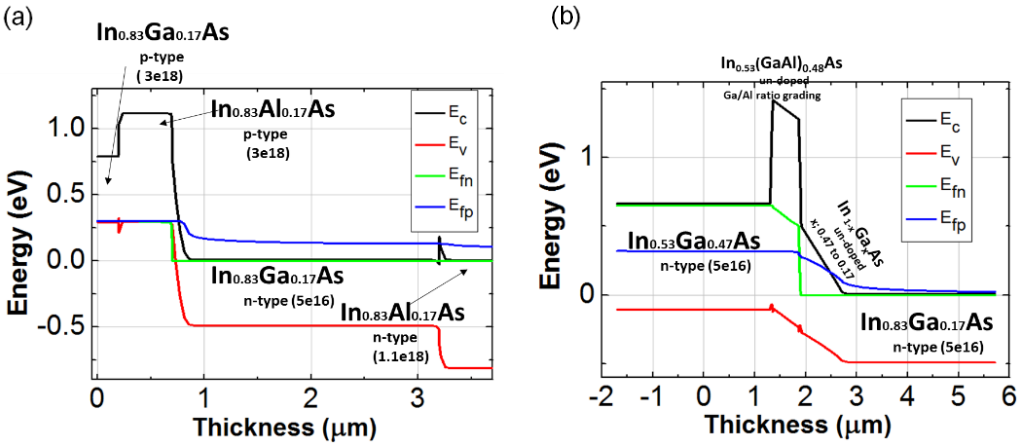

Figure 5.33. eSWIR InGaAs (a) pn and (b) dual-band nBn detector band structures.

The band structures under reverse biased conventional eSWIR InGaAs pn detector and SWIR dual-band nBn detectors are given in Figure 5.33. As can be understood from the band structure of the nBn detector, only the electrons and holes generated in the absorber layer of $In_{0.83}$ $Ga_{0.17}As$ are contributed to the current. The detector will only detect at the eSWIR wavelength under this bias, as the electron flow in the $In_{0.53}Ga_{0.47}As$ absorber layer will be blocked by the barrier. Since the bandgap of the $In_{0.83}Ga_{0.17}As$ material is lower, eSWIR detectors are usually operated around 200 K. Because the temperature is lowered, the diffusion dark current of both detectors is suppressed, but in this case, the G-R dark current and tunnel currents that change less with the temperature will limit the performance of the detector. As seen in Figure 5.34, since the nBn detector suppresses G-R and tunneling currents, it gives 25 times less dark current than the pn detector.

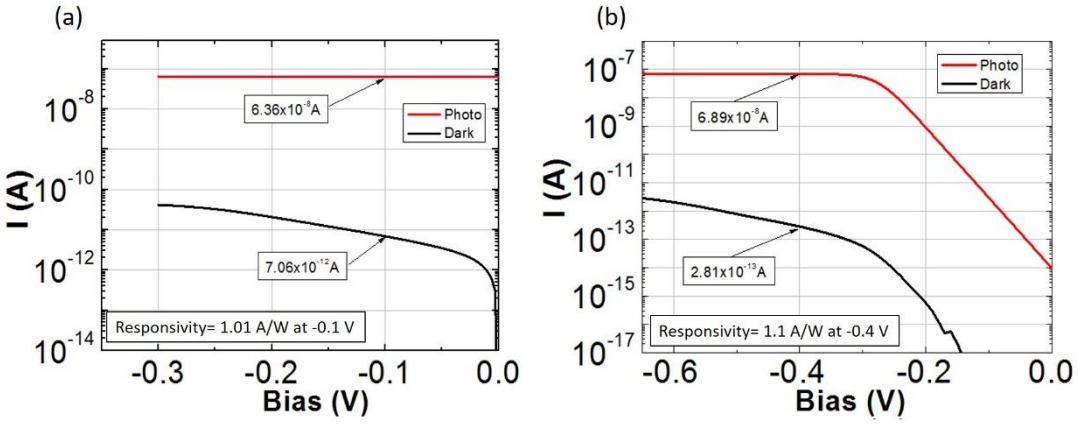

Figure 5.34. eSWIR (cutoff wavelength of 2.5µm) InGaAs (a) pn and (b) dual-band nBn detector dark current and photocurrent graphics.

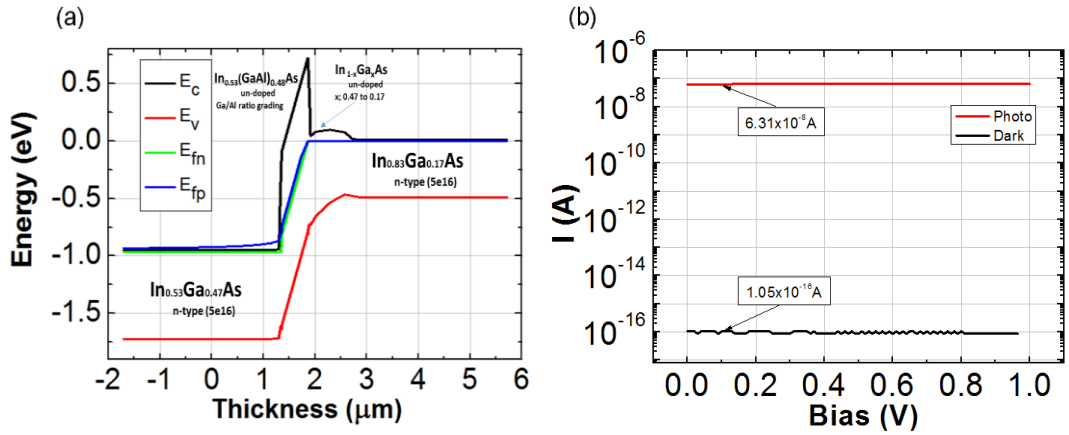

Figure 5.35. (a) InGaAs dual-band SWIR (cutoff wavelength of 1.7µm) band diagram under reverse biased nBn detector and (b) InGaAs dual-band SWIR nBn detector reverse biased (cutoff wavelength of 1.7µm) dark and photocurrent graph under polarity.

In Figure 5.35, the band diagram of the SWIR dual-band nBn detector is kept in reverse polarity bias according to the previous situation. In this case, only the electrons and holes formed in $In_{0.53}Ga_{0.47}As$ absorber layer contribute to the flow. Since the electrons formed in the $In_{0.83}Ga_{0.17}As$ absorber layer will be blocked by the barrier, the electrons and holes produced here do not contribute to the current. Therefore, in this bias situation, the detector will only detect in the SWIR band. In Figure 5.35 (b), the current-voltage curves at the SWIR wavelength of the detector

at 200 K are given. The dark current at 10^{-16} levels indicates that if the detector is in reverse polarity when compared to the previous case, only the electrons and holes formed in the absorber layer of $In_{0.53}Ga_{0.47}As$ contribute to the current.

CHAPTER 6

HgCdTe (MCT) INFRARED PHOTODETECTORS

Mercury cadmium telluride (MCT, $Hg_{1-x}Cd_xTe$) is a material system that has been studied for more than 50 years and its alternative has not yet been developed due to its superior material properties for detector technology. MCT is a direct bandgap material that is a mixture of HgTe and CdTe compounds and has a crystal structure in zinc-blende. In this material system, by changing the Cd mole fraction, MCT material with bandgap can be obtained from minimum –0.2608 eV (HgTe) at 77 K and maximum 1.6088 eV (CdTe) values [127].

The factors that make the MCT material system the most preferred material in the IR detector area in the spectrum range from SWIR to VLWIR (1-30μm) are;

- little change of the lattice constant as the Cd mole rate changes,
- direct bandgap property,
- wide range of the bandgap tune,
- high quantum efficiency and
- reasonable inherent recombination mechanisms.

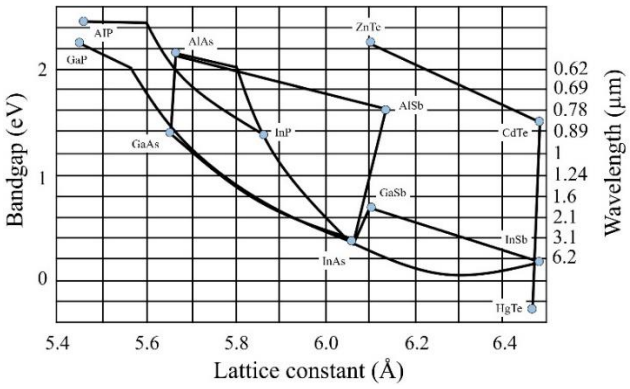

Figure 6.1. Comparison of the III-V and II-VI semiconductor compounds in terms of the energy bandgap, the lattice constant and cutoff wavelength (redrawn from ref. [69]).

As seen in Figure 6.1, compared with group III-V material systems, $Hg_{1-x}Cd_xTe$ is a highly advantageous material system in terms of the lattice constant and cutoff wavelength.

The energy bandgap equation for $Hg_{1-x}Cd_xTe$ is given as [127]:

$$E_g = -0.302 + 1.93x - 0.18x^2 + 0.832x^3 + 5.35\text{x}10^{-4}(1 - 2x)(-1882 + T^3)/(255.2 + T^2) \quad (7.1)$$

where E_g is the energy bandgap (eV), x is Cd mole fraction, and T is the temperature (K).

The relationship between the Cd mole fraction, energy bandgap, cutoff wavelength and lattice constant for $Hg_{1-x}Cd_xTe$ at 300 K and 77 K is given in more detail in Figure 6.2.

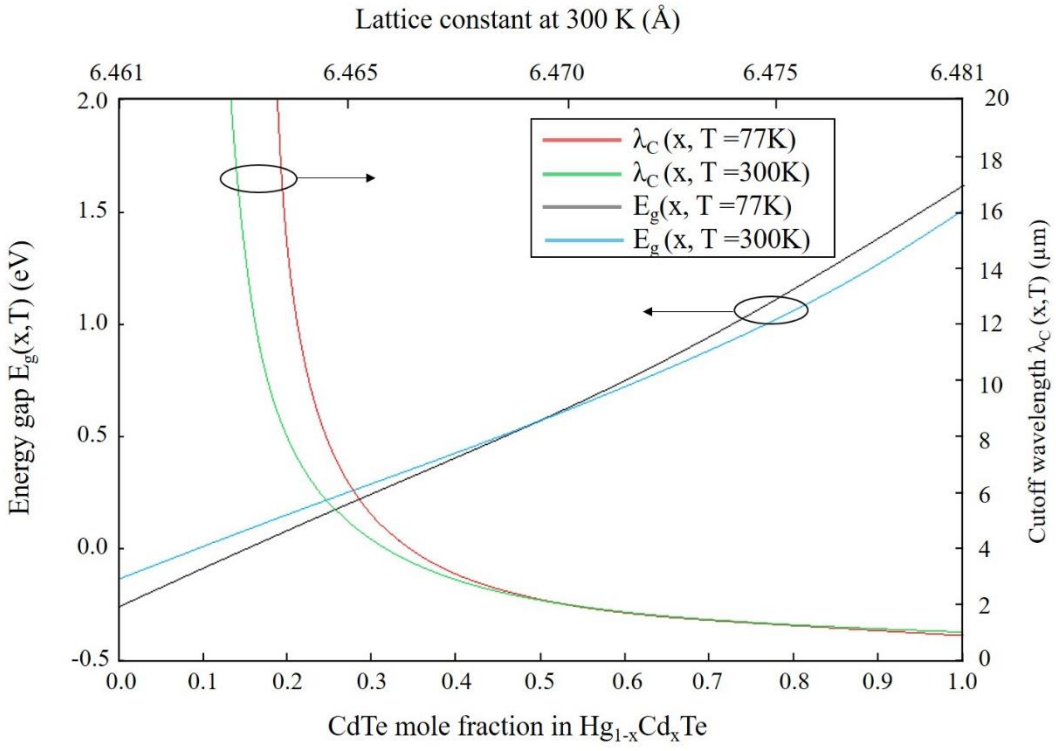

Figure 6.2. Bandgap energy, cutoff wavelength and lattice constant for HgCdTe for each Cd mole fraction (redrawn from ref. [2]).

Due to the very small change in the lattice constant, each composition of the $Hg_{1-x}Cd_xTe$ material system can be grown on CdZnTe substrate without lattice mismatch. In this way, hetero and superlattice structures can be obtained.

The relationship between the lattice constant (a) and Cd mole fraction (x) for MCT is given as [127]:

$$a = 6.4614 + 0.0084x + 0.01168x^2 - 0.0057x^3. \qquad (6.2)$$

The absorption coefficient corresponding to some Cd mole fractions for the different energy photons at room temperature is given in Figure 6.3. A high absorption coefficient indicates that most of the incoming light can be absorbed in a short distance in the absorber material. This enables the thickness of the detector to be short (~10 μm for the LWIR band) while reducing cost, noise and excess thermal generation.

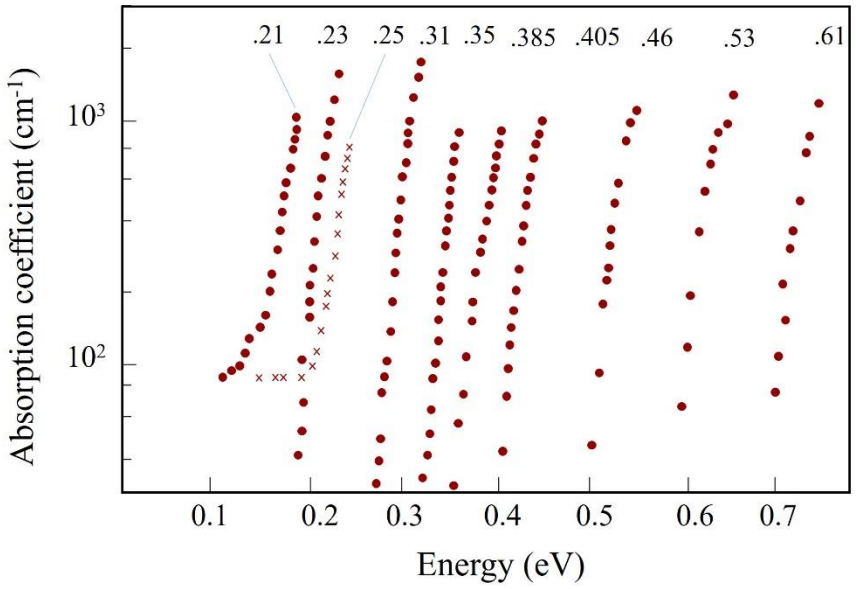

Figure 6.3. Absorption coefficient for $Hg_{1-x}Cd_xTe$ corresponding to some Cd mole fractions at room temperature (redrawn from ref. [69]).

In the HgCdTe detector, while the minority carrier lifetime is limited by the SRH mechanism under conditions of low carrier concentration (~ <10^{15} cm^{-3}), the Auger1 mechanism limits the minority carrier lifetime for high-quality n-type material under the high carrier concentration (~ > 10^{15} cm^{-3}) [10].

Since the electron effective mass of MCT material is small (~ 0.01m_0), electron mobility is high (10^4-10^5 $cm^2V^{-1}s^{-1}$). Electron mobility is mostly determined by mechanisms such as optical phonon scattering and alloy scattering [10]. The hole mobility is about two orders smaller than the electron mobility. Likewise, this is determined by the hole effective mass (~ 0.55 m_0) [10].

6.1 HgCdTe Photodetector Structures

The schematic representation of homo (n+-on-p) and heterojunction (p-on-n) band diagrams of commonly used MCT detectors is given in Figure 6.4. To reduce the tunneling current, the absorber doping amount is kept below 10^{16} cm^{-3}.

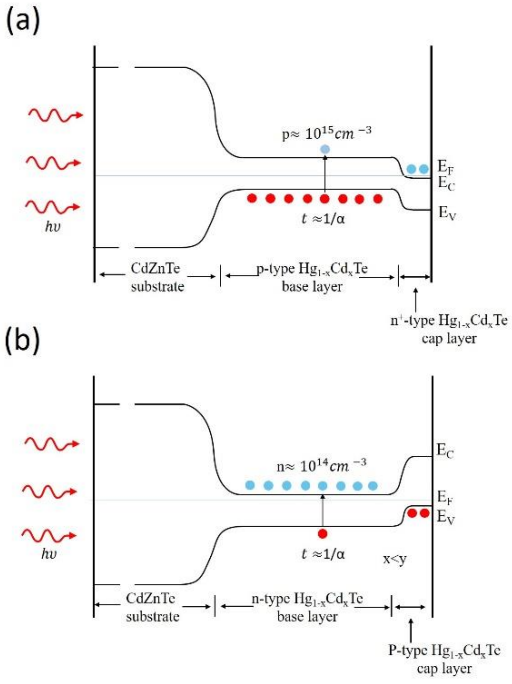

Figure 6.4. Homo (n +-on-p) and heterojunction (p-on-n) of band diagrams of commonly used MCT detectors (redrawn from ref. [2]).

Since In is very suitable for MCT in terms of solubility and diffusivity, it is used as n-type dopant material. Arsenic (As) atom has been shown to be the most suitable material for MCT material as a p-type dopant, due to its properties, such as low diffusivity, low activation energy, stability in the lattice, and concentration controllability [2]. However, As doping is not sufficient to obtain p-type MCT. Since As is an amphoteric (double acting) in MCT, MCT material must be annealed for the activation of As atoms. This topic will be discussed later in this section.

Figure 6.5 shows an IR detector FPA with a schematic representation of the hybrid version of the readout circuit (ROIC). Basically, FPA is a version of isolated pn junction diodes in a 2D pixel array. In this structure, one contact of each detector is common, and the other contacts are integrated with the silicon ROIC array.

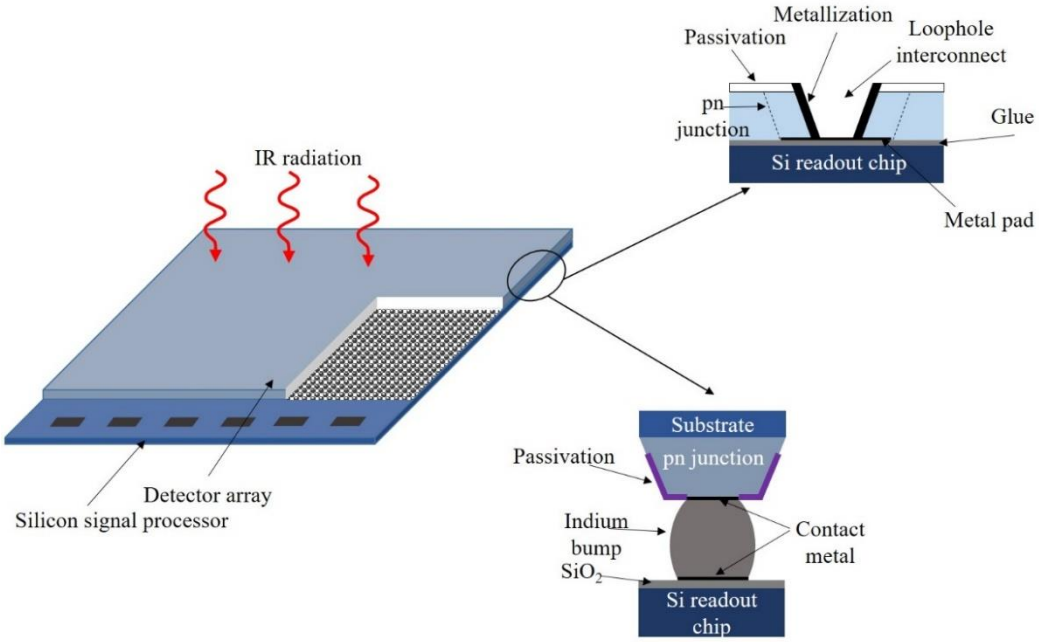

Figure 6.5. Schematic of hybridized FPA and ROIC (redrawn from ref. [7]).

Many pixel structures are used for HgCdTe FPA fabrication. Here, double-layer heterojunction (DLHJ), two-color triple-layer heterojunction, and via-hole (loophole) detector technologies are mentioned.

Double Layer Heterojunction (DLHJ): As can be seen in Figure 6.6, in this structure, a high bandgap p-contact layer is connected to the ROIC with an In bump. The n-layer is designed as an absorber material. Since the absorber layer is n-type, low carrier concentration can be obtained and it has fewer SRH centers than a p-type absorber. Moreover, the passivation of the n-type layer is easier than the p-type layer.

In many studies, the R_{0A} value of detectors with a DLHJ structure has been shown to be higher than in via-hole or planar detectors. Crosstalk is minimized since there is electrical isolation between the pixels.

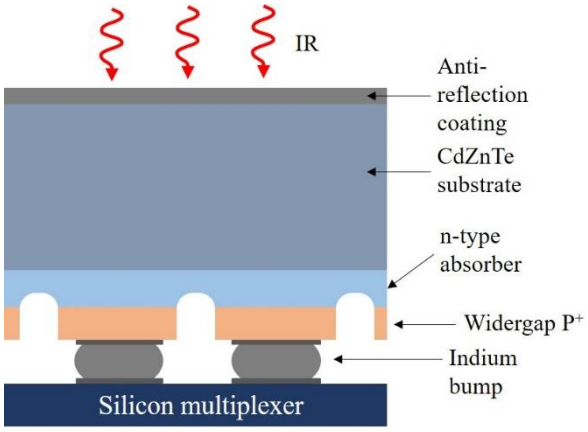

Figure 6.6. Pixel structure of DLHJ detector technology (redrawn from ref. [128]).

Two-color Triple Layer Heterojunction (TLHJ): This detector structure, developed by Raytheon Vision Systems (RVS), can work in dual-band mode by performing polarity switching due to its back-to-back diode structure. In this structure (Figure 6.7), n-type absorber1 (MWIR), p-type cap, and n-type absorber2 (LWIR) epilayers are grown on CdZnTe substrate using MBE method. The sidewalls of the pixels, isolated from each other by the etching method, are passivated with CdTe. Indium bumps are deposited on top of the pixels for hybridization with ROIC [129].

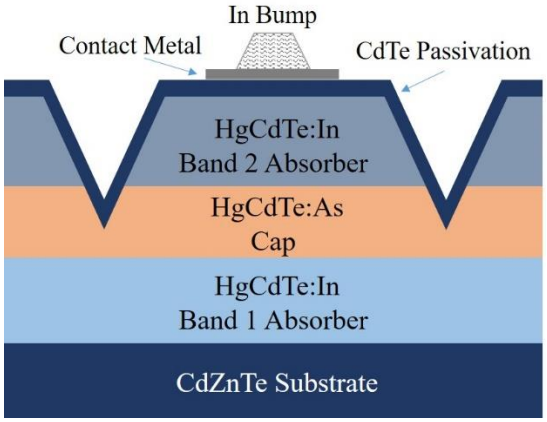

Figure 6.7. Pixel structure of the TLHJ (redrawn from ref. [129]).

Via-hole (loophole): In this architecture, also called high-density vertically integrated photodetector (HDVIP), a via-hole is drilled along the ROIC to the pixel structures (Figure 6.8). A cylindrical n-region is created around this via using the ion implantation method. This method makes it possible to produce FPA with dual-band and small pitch pixels (5 μm).

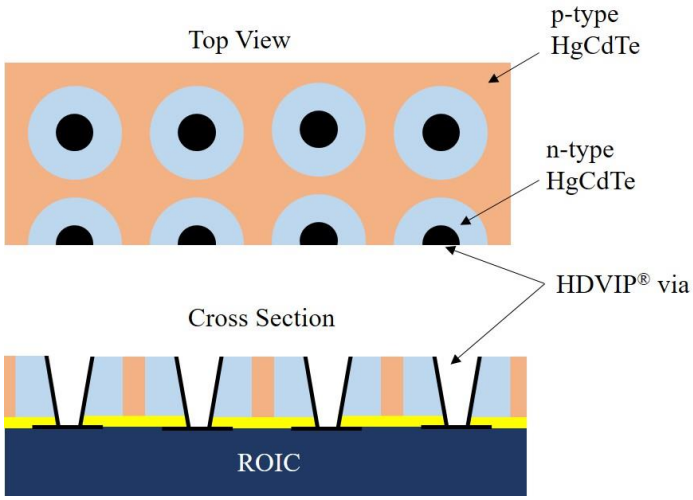

Figure 6.8. Pixel structure of the HDVIP architecture (redrawn from ref. [130]).

6.2 HgCdTe Unipolar Barrier Infrared Detectors

6.2.1 Barrier Engineering for HgCdTe Unipolar Detectors on Alternative Substrates

In this study, the graded layers with delta-dopings has been utilized to get valence band free nBn configurations for the HgCdTe material system in all the short-wave (SWIR), medium-wave (MWIR) and long-wave (LWIR) infrared bands. Shockley Read Hall (SRH), trap-assisted tunneling (TAT), Auger and radiative recombination mechanisms have been included in the analyses and strong suppression of G-R and TAT currents have been demonstrated with the designed structures. This methodology is especially useful when the carrier lifetime is limited due to alternative substrate usage, such as Si, GaAs and GaSb. No degradation in photo-response has been observed as adjusting the valence band offset is quite flexible with the delta-doped nano-layers and the valence band barrier can be completely removed. Calculations have been performed for 1–3 μs lifetime targeting the alternative substrate applications and up to 60 degrees of increase in the operation has been shown to be possible.

Mercury cadmium telluride (HgCdTe) infrared detectors shows one of the highest performance among all the infrared detector technologies due to the excellent optical and electrical properties [2]. However, economic and technical reasons limit the use of the conventional CdZnTe substrate for HgCdTe detectors in a wide range of applications [132]–[134]. As a solution, developing processes with alternative substrates for HgCdTe detectors is one of the preliminary research topics today. However, all the studies so far have a sizable lattice mismatch with HgCdTe layers affecting the performance of the detectors. The extra cooling requirement to compensate this performance drop may result in an increase in the system cost defeating the purpose of the alternative substrate technologies unless epilayer structure optimization methods are applied [135]–[138]. One of these methods is utilizing unipolar detector architectures that have emerged relatively recently as an

alternative to the conventional pn structures and provide performance improvements for various measures [39], [41]–[70], [139].

Here, nBn type HgCdTe detectors in the short-wave (SWIR), medium-wave (MWIR) and long-wave (LWIR) bands are designed by a relatively simple method that removes the valence band offset with the help of delta-doped layers and compositional grading [59], [101]. Calculation results show that designed detectors give considerably lower dark current compared to conventional pn heterojunction structures, leading to a higher operation temperature possibility, especially for the detectors with an alternative substrate that usually suffers from shorter SRH lifetimes.

6.2.1.1 Method

Current-voltage characteristics (I-V) comparison for both dark and illuminated environments is the main method to evaluate different designs in addition to the band diagrams, which are used for the explanation of the results. Shockley Read Hall (SRH) based on Schrafetter recombination model, trap-assisted tunneling (TAT) with Hurkx model that shortens the carrier lifetime and Auger and radiative recombination mechanisms have been included in the numerical simulations in terms of the various dark current mechanisms [84]. Since almost nonexistent depletion region is one of the most important benefits for the nBn structures, designed structures here are targeted more to the cases where the SRH lifetime is limited as in the case of HgCdTe detectors fabricated with alternative substrates. For these detectors, as the carrier lifetime can be as low as 50 ns [91], moderate values between 1 and 3 μs are chosen here. For all the nBn designs here, there is also a conventional pn heterojunction detector prepared with the same parameters in order to save the results from including experimental differences and focus the comparison on purely epilayer structures. Nonetheless, the reference pn structures here provide the same dark current levels with the previously reported experimental studies with alternative

substrates [140]. The SRH lifetimes and trap parameters [46] that are used in the simulations are shown in Table 6.1.

Table 6.1 SRH Lifetime and Trap parameters

Trap Parameters	*SWIR*	*MWIR*	*LWIR*
SRH lifetime (s)	3μs	1μs	1μs
Energy level (eV)	0.25Eg	0.25Eg	0.25Eg
Concentration (cm^{-3})	10^{13}	10^{13}	10^{13}
Capture Cross S. σ_n, σ_p (cm^2)	10^{15}, 10^{16}	10^{15}, 10^{16}	10^{15}, 10^{16}

Since there is no built-in voltage in the nBn structures, bias requirements are different for these detector types. In particular, nBn designs need a bias voltage to be able to collect the photo-generated carriers; however, pn heterojunction starts suffering from tunneling currents quickly with increasing bias, especially as the bandgap gets narrower. Therefore, the dark and photo-current characteristics of these structures are calculated at different bias points. A reverse bias voltage of 0.2 V where the photo-current saturates has been chosen for the nBn structures and a smaller value (0.1 V) for the conventional pn heterojunctions is used.

6.2.1.2 Device Design

The barrier in the designs here is obtained by compositional grading of un-doped HgCdTe material from low bandgap to high bandgap with the help of the almost unvarying lattice constant for different mole fractions in the HgCdTe material system as shown in Figure 6.9 (a). If the barrier is inserted into this structure with no additional bandgap engineering, a valence band offset forms, as can be seen in the calculated band diagram shown in Figure 6.9 (b). This will obviously block minority carriers and the responsivity of the detector will be severely affected.

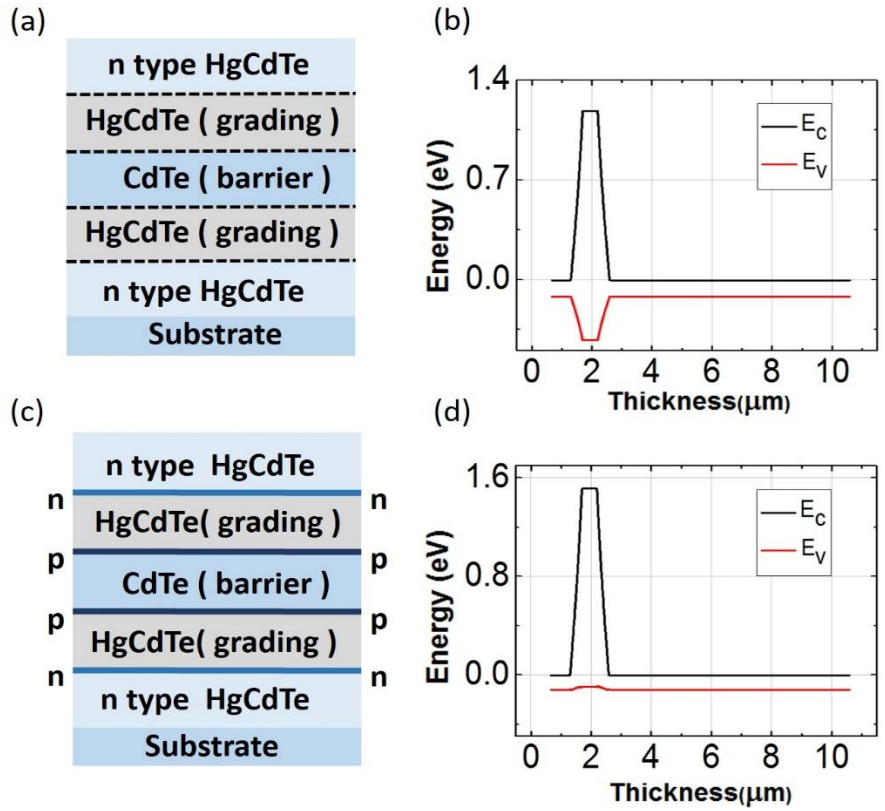

Figure 6.9. HgCdTe nBn detector with and without removed valence band offset; (a) and (c) pixel structures and (b) and (d) band diagrams.

As a solution, and the main topic in this work, a couple of thin n- and p-type delta doping layers can be placed on both sides of the graded layers in such a way that the quasi-electric fields generated by the graded layers will be suppressed similarly to the other material systems [59], [79], [77], [101]. Inserting delta-doped layers for adjusting the valence band barrier can indeed be extremely useful for HgCdTe detectors as obtaining an adjustable barrier material without a lattice mismatch issue is quite easy. In the barrier region, p-type delta doping nano-layers are placed on the edge of the high bandgap of the graded layers and n-type delta doping nano-layers on the edge of the low bandgap edge (Figure 6.9 (c)). The electric field generated by the charges of p and n layers will suppress the quasi-electric field generated by the graded layers resulting in a zero valence band offset, as demonstrated in Figure 6.9 (d).

The presented designs here do not take into account the effects of extended traps, which potentially can shortcut the barrier and may degrade the operational temperature [141] due to the complexity it will bring to the calculations. In addition, as a solution for the propagation of these defects into the epilayers from the substrate, an interfacial layer has been proposed to be utilized [111].

6.2.1.3 Results and Discussions

6.2.1.3.1 Comparison of nBn and pn Detectors in SWIR Band

The need for high-format FPAs and the possibility of producing the detectors at a lower cost, increase the interest for HgCdTe detectors on the alternative substrates in the SWIR region. However, due to the lattice constant difference between the substrate and the epilayers, the G-R and TAT current will increase in the detectors. Since the nBn detector architecture can suppress dark-current components originated from the depletion region, the method, which was the first time applied for obtaining InGaAs nBn detector [59], [101], can be applied to low-cost HgCdTe detectors in SWIR band. Therefore, in this section, HgCdTe nBn and pn detector structure are compared using the same the SRH and trap parameters. General pixel structures and band diagrams at operating bias of pn and nBn detector for the SWIR band are shown in Figure 6.10 (a)-(d). Structural and electrical parameters such as Cd mole ratio, layer thicknesses and the optimized doping concentrations for obtaining zero valence band offset used for these configurations are given in Table 6.2. Barrier thickness is chosen to be thick enough to avoid tunneling current and Cd mole fraction in the barrier is selected to be 1 to prevent the thermionic emission as much as possible. Figure 6.11 (a)-(b) shows the I-V curve calculations for both dark and illuminated (under 1.5 μm radiation) cases at two different (300–240 K) temperatures and the dark currents components in these I-V curves are shown in Figure 6.11 (c)-(h) for a 25×25 μm^2 detector area.

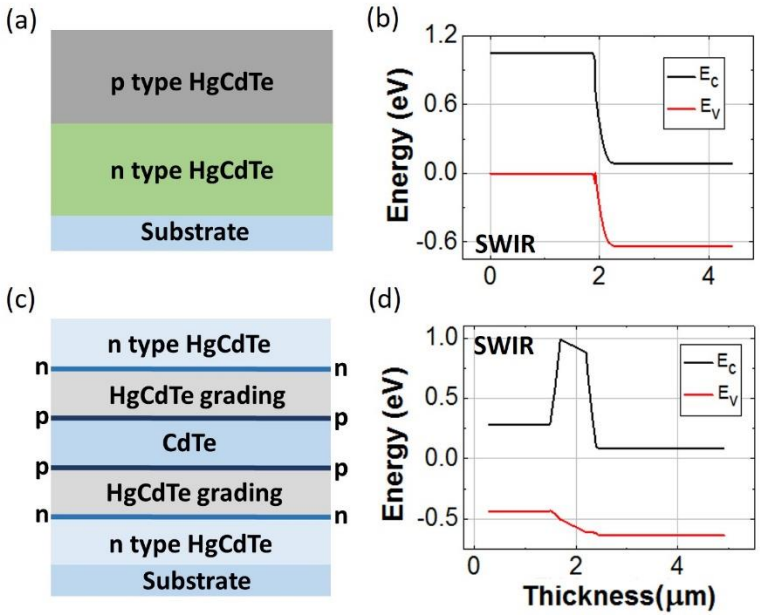

Figure 6.10. General pixel structures and band diagrams of pn and nBn detector for HgCdTe SWIR detectors

Table 6.2 SWIR nBn and pn Detector Pixel Layers Properties

SWIR		*nBn*	*pn*
Absorber	Cd	0.605	0.605
	Nd	1.1×10^{16} cm^{-3}	1.1×10^{16} cm^{-3}
	L	2.5 μm	2.5 μm
Contact	Cd	0.605	0.8
	Nd/Na	1.1×10^{16} cm^{-3}	2×10^{17} cm^{-3}
	L	1.2 μm	1.92 μm
Barrier	Cd	1.0	---
	Nd/Na	un-doped	---
	L	0.5 μm	---
D. Doping	Cd	0.605 and 1.0	---
	Nd/Na	1.5×10^{17}	---
	L	5 nm	---
Grading	Cd	0.605 to 1.0	---
	Nd/Na	un-doped	---
	L	385 nm	---

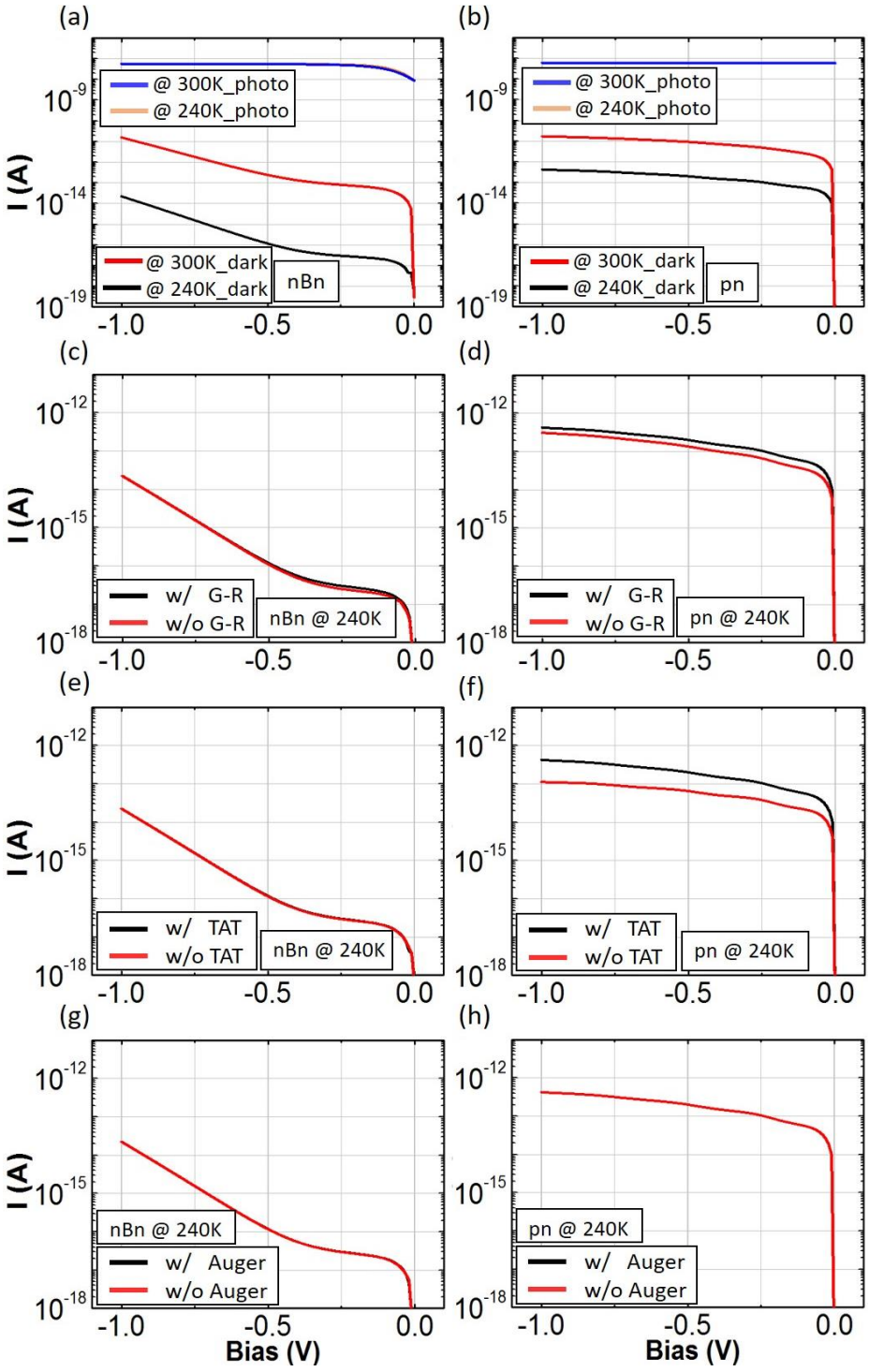

Figure 6.11. Comparisons of dark current results at two different temperatures (a) and (b) and separated dark current component (c)-(h) of nBn and pn detectors at 240 K in SWIR band. (Not: The photocurrent curves calculated for two different temperatures are overlap.)

When Figure 6.11 (a) and Figure 6.11 (b) are compared, there is more than one order of magnitude dark current difference at 300 K (7.19×10^{-14} A at −0.2 V vs. 2.53×10^{-12}A at −0.1 V) between nBn and pn detectors whereas there is almost no difference in terms of the photo-current. In order to get the same dark current levels from these structures, the pn heterojunction detector needs to be cooled down to 240 K clearly indicating the cost reduction potential for the nBn structure. Moreover, if the nBn design is also cooled down to 240 K, the dark current difference between the structures increases even further (> 2500 times) due to the fact that TAT contribution which is suppressed by the nBn design is more dominant at lower temperatures as seen in Figure 6.11 (e).

In Figure 6.11 (c)-(h), the dark current components (G-R, TAT, Auger) of the nBn and pn detectors for SWIR band were examined individually at 240 K. Although TAT current is more dominant in this temperature for the pn structure, the effect of the G-R current is still observed (Figure 6.11 (d)), where these components are successfully suppressed in the nBn design (Figure 6.11 (c) and Figure 6.11 (e)). In addition, the Auger mechanism (Figure 6.11 (g)-(h)) and radiative recombination is not effective for this band. At higher bias values, the effectiveness of the barrier starts to decrease as the bandgap for the SWIR region is relatively thicker.

6.2.1.3.2 Comparison of nBn and pn detector in MWIR band

The need for cooling the photon detectors to cryogenic temperatures for suppressing the dark current limits the application opportunities of the detectors and increases their cost for the lower bandgap regions. The applied nBn design can also solve the valence band discontinuity problem for MWIR region with its flexibility. The calculated band diagrams for nBn and pn structures are shown in Figure 6.12 (a)-(b), respectively, where the parameters used for both designs are listed in Table 6.3. Compositional gradings are again adjusted so that the barrier is composed of un-doped CdTe with a 500 nm thickness. The SRH lifetime for the MWIR case is chosen to be 1 μs, the illumination wavelength is 4 μm and the detector size is again

25×25 μm^2. Results comparing the applied nBn design with conventional pn heterojunction are summarized in Figure 6.13 where radiative recombination is not effective in neither of the cases.

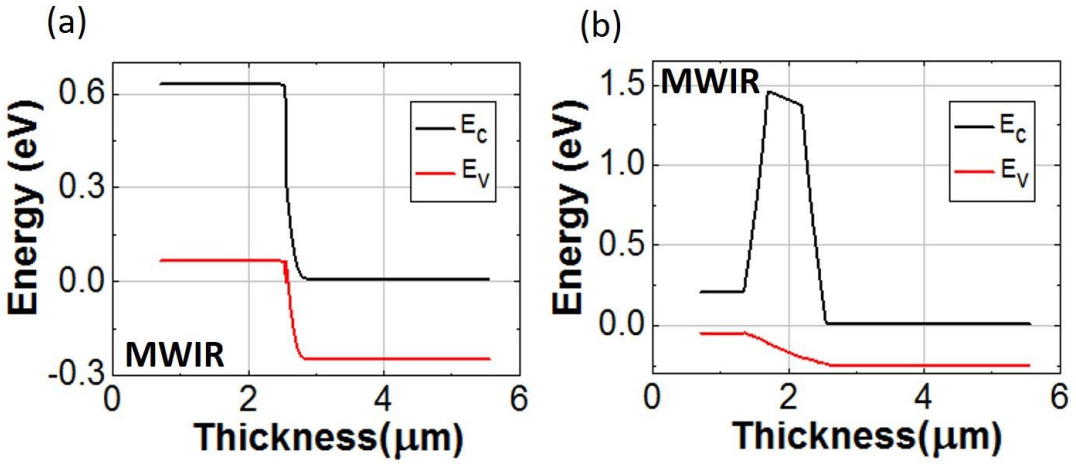

Figure 6.12. Band diagrams of (a) pn and (b) nBn detector for HgCdTe MWIR detectors.

Table 6.3 MWIR nBn and pn Detector Pixel Layers Properties

MWIR		*nBn*	*pn*
Absorber	Cd	0.3	0.3
	Nd	1×10^{16} cm^{-3}	1×10^{16} cm^{-3}
	L	3 μm	3 μm
Contact	Cd	0.3	0.5
	Nd/Na	1×10^{16} cm^{-3}	2×10^{17} cm^{-3}
	L	0.63 μm	1.85 μm
Barrier	Cd	1.0	---
	Nd/Na	un-doped	---
	L	0.5 μm	---
D. Doping	Cd	0.3 and 1.0	---
	Nd/Na	1.2×10^{17}	---
	L	5 nm	---
Grading	Cd	0.3 to 1.0	---
	Nd/Na	un-doped	---
	L	385 nm	---

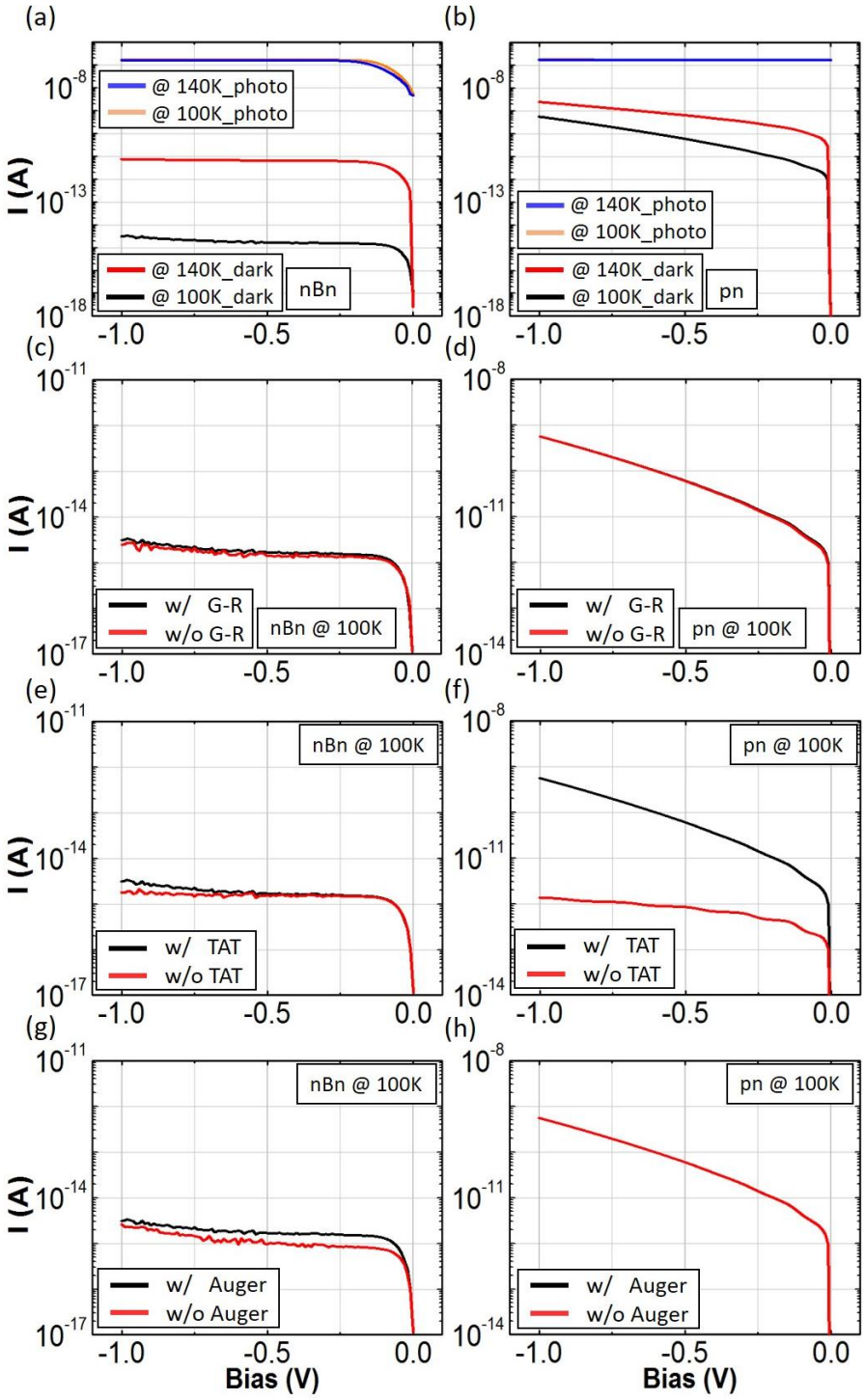

Figure 6.13. Comparisons of dark current results at two different temperatures (a) and (b) and separated dark current component (c)-(h) of nBn and pn detectors at 100 K in MWIR band. (Not: The photocurrent curves calculated for two different temperatures are overlap.)

As shown in Figure 6.13 (a)-(b), at 100 K, the dark current of the nBn design is 1.52×10^{-15} A at the operating point of −0.2 V, whereas it is 4.29×10^{-12}A at −0.1 V for the pn case. There is more than three orders of magnitude difference at 100 K and the dark current level obtained for the pn structure at this temperature occurs at 140 K for the nBn configuration. In Figure 6.13 (c)-(h), the dark current components of the nBn and pn structures for the MWIR band are examined at 100 K. At this temperature, TAT is the most effective mechanism (Figure 6.13 (f)) in terms of the dark current characteristics for the pn case as the G-R current component has been effectively reduced at this temperature (Figure 6.13 (d)). On the other hand, the TAT mechanism can be effectively suppressed in the nBn detector structure, as shown in Figure 6.13 (e). Therefore, unlike the pn detector, the dark current continues to drop as the temperature decreases. As shown in Figure 6.13 (g), the effect of the Auger dark current component is observable since the nBn detector gives very low dark current at 100 K. Calculated Auger 1 constant and lifetime values are 3.69×10^{-26} cm^6s^{-1}, 2.71×10^{-7} s, respectively, which are consistent with the values obtained from the previous studies [24], [142], [143].

6.2.1.3.3 Comparison of nBn and pn detector in LWIR band

In this section, the valence band suppressed nBn structure, which gives a lower dark current than the pn detector, was applied to the LWIR band in order to demonstrate its applicability. Figure 6.14 (a)-(b) shows the nBn and pn band diagrams in the LWIR band and the parameters used for each detector type are given in Table 6.4. In these calculations, the SRH lifetime used is again 1 μs and the absorption wavelength is 10 μm for the pixel area of 25×25 μm^2.

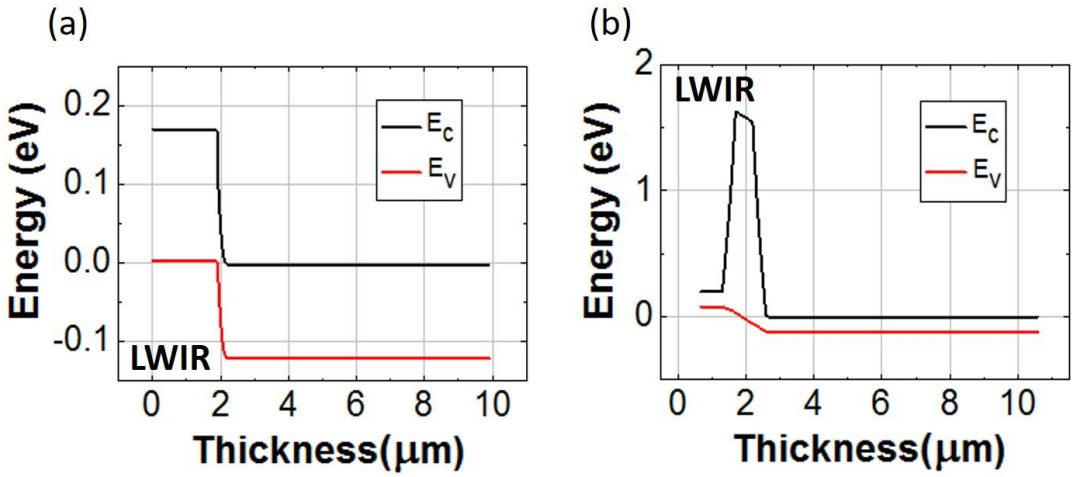

Figure 6.14. Band diagrams of (a) pn and (b) nBn detector for HgCdTe LWIR detectors.

Table 6.4 LWIR nBn and pn Detectors Pixel Layers Properties

LWIR		*nBn*	*pn*
Absorber	Cd	0.22	0.22
	Nd	5×10^{15} cm^{-3}	5×10^{15} cm^{-3}
	L	8 μm	8 μm
Contact	Cd	0.22	0.25
	Nd/Na	5×10^{15} cm^{-3}	1×10^{17} cm^{-3}
	L	0.63 μm	1.92 μm
Barrier	Cd	1.0	---
	Nd/Na	un-doped	---
	L	0.5 μm	---
D. Doping	Cd	0.22 and 1.0	---
	Nd/Na	1.2×10^{17}	---
	L	5 nm	---
Grading	Cd	0.22 to 1.0	---
	Nd/Na	un-doped	---
	L	385 nm	---

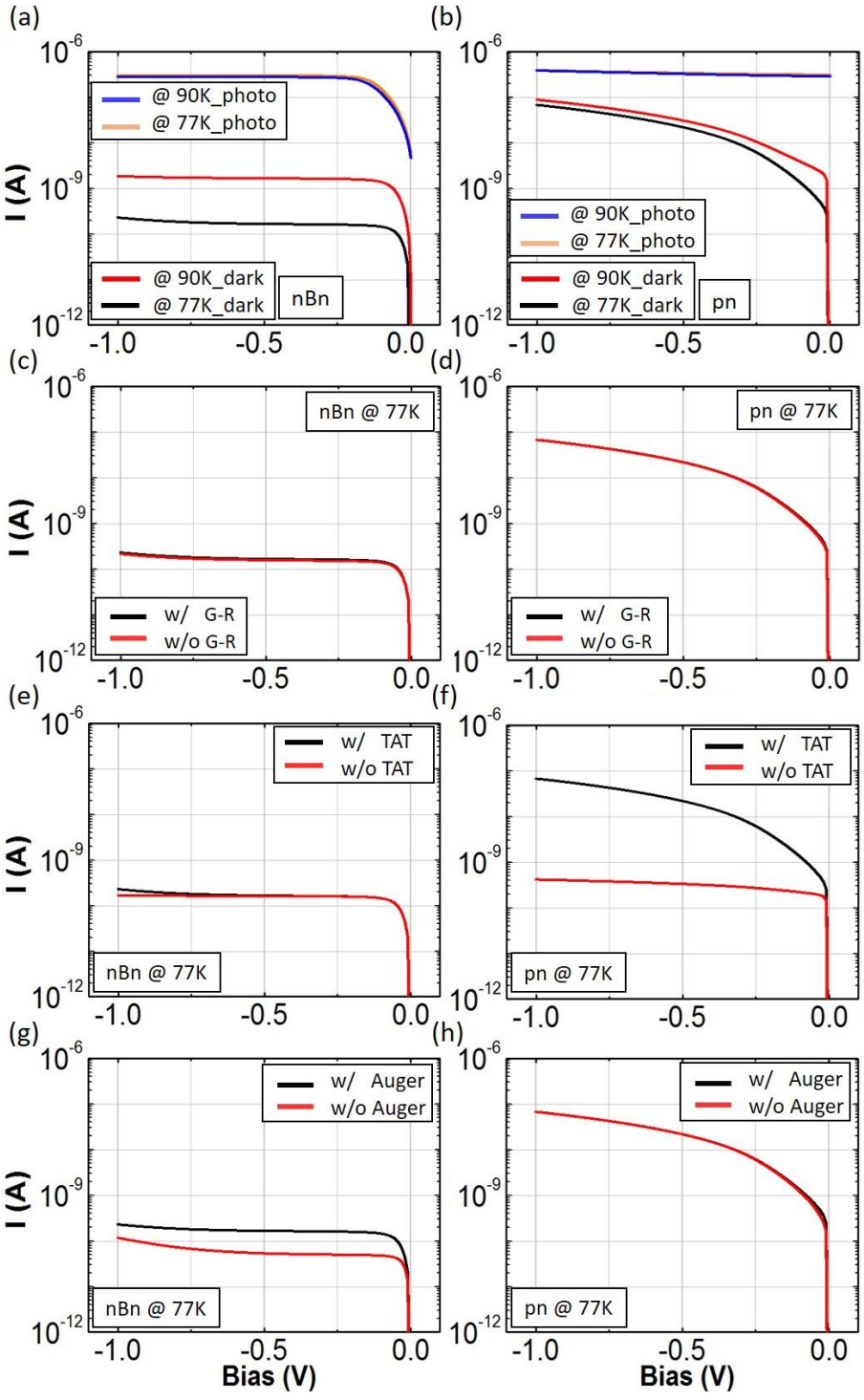

Figure 6.15. Comparisons of dark current results at two different temperatures (a) and (b) and separated dark current component (c)-(h) of nBn and pn detectors at 77 K in LWIR band. (Not: The photocurrent curves calculated for two different temperatures are overlap.)

Figure 6.15 (a)-(b) shows comparison between nBn and pn designs in the LWIR band at 77 K and 90 K where the dark current of nBn design is 1.58×10^{-10} A at a reverse bias of 0.2 V and pn heterojunction dark current level is 1.37×10^{-9}A at−0.1 V at 77 K. The dark current level for the nBn structure at 90 K is nearly the same with pn heterojunction at 77 K. The dark current difference between nBn and pn detector increases quickly for higher reverse bias values mainly because of the TAT component [135], [137]. There is again an effective suppression of the TAT current for the nBn structure and TAT is the most dominant dark current mechanism for the conventional pn heterojunction (Figure 6.15 (f)) for LWIR band [144]. The effect of the G-R current is never seen because of the low temperature. As shown in Figure 6.15 (h), similar to the MWIR case, the effect of Auger dark current is dominant at this temperature for the nBn configuration due to the suppressed TAT component. Auger constant value is calculated to be 4.4×10^{-25} cm^6 s^{-1} and the Auger 1 lifetime is obtained as 0.9×10^{-7} s in parallel with the earlier work [24], [142], [143].

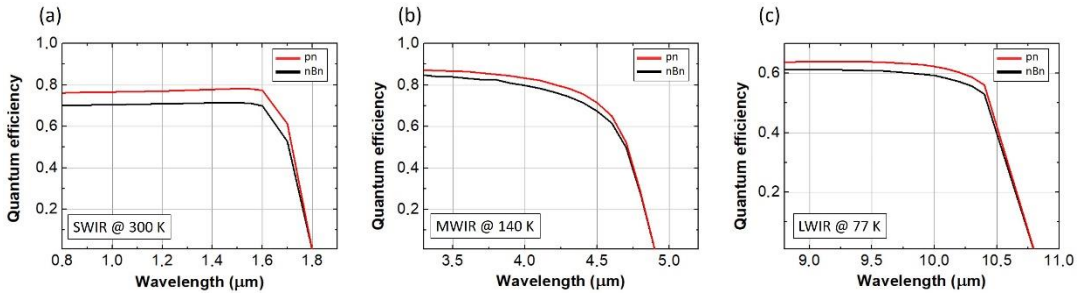

Figure 6.16. Quantum efficiency graphs of SWIR, MWIR, and LWIR band pn (at −0.1V) and nBn (at −0.4V) detectors.

Quantum efficiency graphs for pn and nBn detectors operating in SWIR, MWIR and LWIR bands are given in Figure 6.16. There are tolerable differences in the quantum efficiencies of nBn and pn detectors.

6.2.2 A Dual-Band HgCdTe nBn Infrared Detector Design

In this study, a dual-band nBn HgCdTe detector structure utilizing the graded layers with delta-dopings has been designed numerically and the results have been compared with a conventional pn detector for each band. Almost nonvarying lattice constant with respect to bandgap variation of the HgCdTe material makes this design plausible. Thus, Cd molar ratios of the n-type absorber layers have been selected to correspond to LWIR and MWIR bands and the barrier layer consists of an un-doped CdTe material. In addition, it is important to note that considering the dark current performances of the state of the art HgCdTe detectors fabricated with the traditional CdZnTe substrates, suppressing the dark current components associated with the depletion region, the major benefit of the nBn structure, may not seem to be necessary for this material system. However, there are many studies focusing on HgCdTe layers grown on the alternative substrates (usually with much shorter SRH lifetime values) and these devices may substantially benefit from the utilized method here.

6.2.2.1 Method and Device Design

One of the most critical points in designing nBn type detectors is the insertion of the barrier layer where there must be a high barrier for the majority carriers and no barrier should exist for the minority carriers in the electronic band structure. Therefore, if the absorber layer is n-type, as in our case, the barrier should only be in the conduction band. Moreover, the height of the barrier must be high enough to block thermionic emission and thick enough not to allow tunneling [42]. Despite the promise for better dark current characteristics, these restrictions make this type of barrier structures challenging to be applied to a variety of detector material systems such as InGaAs and HgCdTe due to the lack of suitable barrier material. As a result, additional band diagram engineering becomes necessary. Here, a few nm thick p and n delta-doped layers together with un-doped compositionally graded layers have

been utilized in both sides of the high bandgap layer (Figure 6.17) in order to remove the valence band discontinuity similar to the previous studies [59], [79], [83], [101], [139], [145].

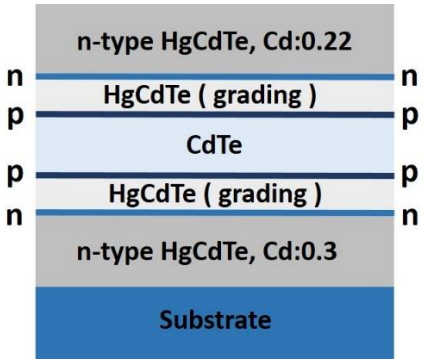

Figure 6.17. Pixel structure of LWIR/MWIR dual-band HgCdTe nBn.

Numerical calculations were made with the commercial software Sentaurus Device [84] using the parameter values in Table 6.5, Table 6.6 and Table 6.7 for the nBn structure, reference pn structure and the traps in the materials, respectively.

Table 6.5 Material Parameters for LWIR/MWIR Dual-Band HgCdTe nBn

Dual-band HgCdTe nBn	Absorber			Barrier			Delta-doping			Grading		
	Cd	Nd	L	Cd	Nd	L	Cd	Nd/Na	L	Cd	Nd	L
LWIR (absorber_1)	0.22	1×10^{16} cm^{-3}	8 µm	1.0	un-doped	0.5 µm	0.22 and 1.0	1×10^{17} cm^{-3}	5 nm	0.22 to 1.0	un-doped	385 nm
MWIR (absorber_2)	0.3	1×10^{16} cm^{-3}	3 µm	1.0	un-doped	0.5 µm	1.0 and 0.3	1×10^{17} cm^{-3}	5 nm	1.0 to 0.3	un-doped	385 nm

Table 6.6 Material Parameters for HgCdTe pn

HgCdTe pn		LWIR pn	MWIR pn
Absorber	Cd	0.22	0.3
	Nd	1e16	1e16
	L	8 µm	3 µm
Contact layer	Cd	0.5	0.5
	Na	1e17	2e17
	L	1.92 µm	1.85 µm

Table 6.7 Trap Parameters

	MWIR	LWIR
SRH lifetime (s)	10 μs	10 μs
Energy level (eV)	0.25 Eg	0.25 Eg
Concentration (cm^{-3})	10^{13}	10^{13}
Capture cross s. σ_n, σ_p (cm^2)	10^{15}, 10^{16}	10^{15}, 10^{16}

6.2.2.2 Results and Discussions

Figure 6.18 shows the numerically calculated band diagram of the unbiased LWIR/MWIR dual-band HgCdTe nBn detector. The electric field generated by the depleted n and p delta layer has successfully suppressed the electric field formed by the graded layers and as shown in the figure, there is no valence band offset that might prevent the minority carrier flow.

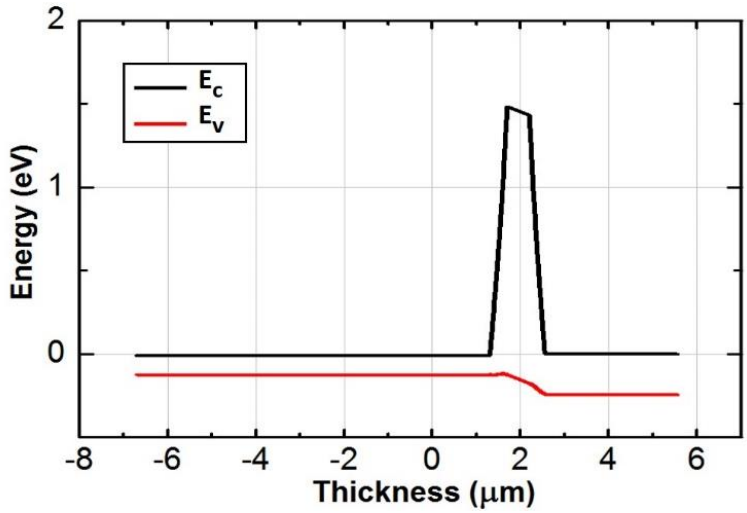

Figure 6.18. Calculated energy band diagram of LWIR/MWIR dual-band HgCdTe nBn detector at zero bias.

Figure 6.19 shows the band structure of the designed LWIR/MWIR dual-band HgCdTe nBn detector, where the LWIR band is under positive bias. Since the electrons formed in the MWIR absorber layer will be blocked by the barrier, the designed detector will only collect the photo-carriers generated in the LWIR band.

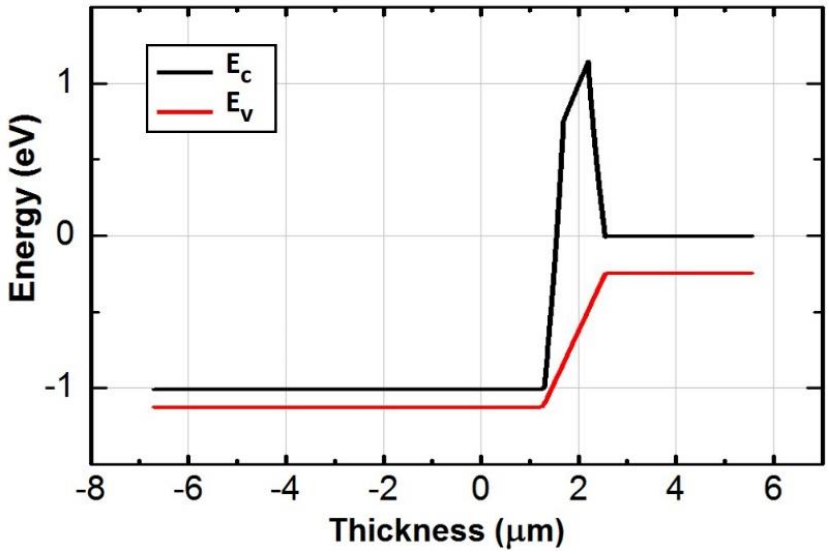

Figure 6.19. Calculated energy band diagram of LWIR/MWIR dual-band HgCdTe nBn detector while LWIR absorber is under positive bias.

Furthermore, Figure 6.20 shows the LWIR band photocurrent and dark current characteristics at 77 K of the designed nBn structure and the reference heterojunction pn detector. While both of the simulated structures have almost the same photocurrent levels, nBn design indicates superior characteristics in terms of the total dark current level and the voltage dependency of the dark current.

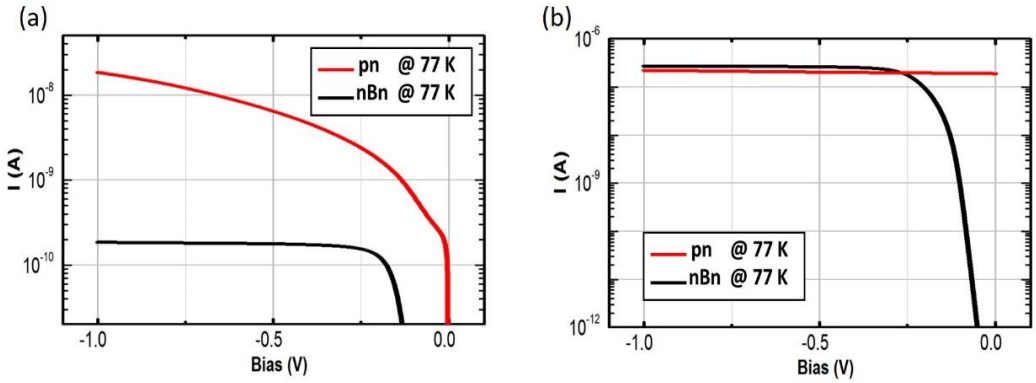

Figure 6.20. (a) Dark current characteristics of the nBn type dual-band HgCdTe detector design in LWIR band in comparison with conventional pn heterojunction (b) Photocurrent comparison between the designed nBn and pn structures in LWIR band.

As clearly seen in Figure 6.20 (a), as the reverse bias increases, the dark current of the pn detector increases with increasing reverse bias while the dark current of the nBn dual-band detector does not show a major reverse bias dependency mainly due to the fact that the nBn detector does not have a depletion region and can suppress the TAT current [139].

Figure 6.21 and Figure 6.22 show the simulation results for MWIR band in the same representation followed in Figure 6.19 and Figure 6.20 for the LWIR band where the polarity of the applied bias has been switched in order to collect the photo-generated carriers in the MWIR band.

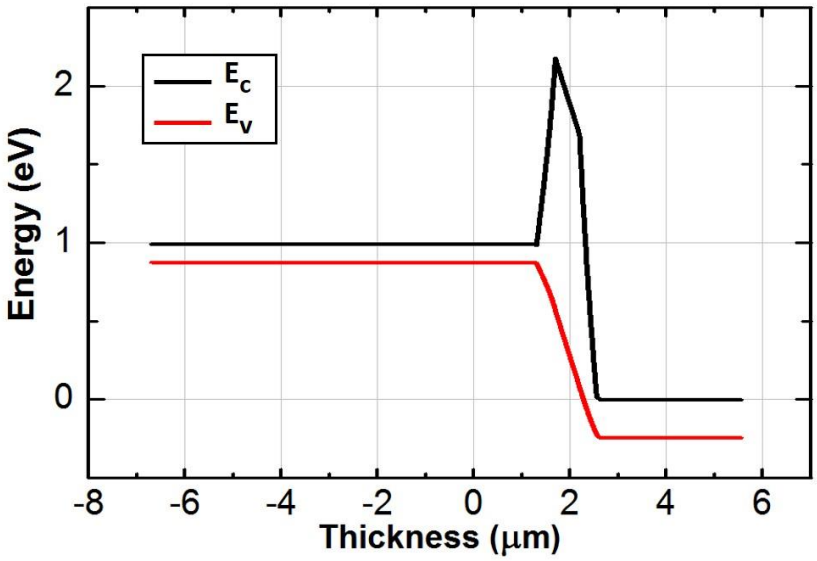

Figure 6.21. Calculated energy band diagram of LWIR/MWIR dual-band HgCdTe nBn detector while MWIR absorber is under positive bias.

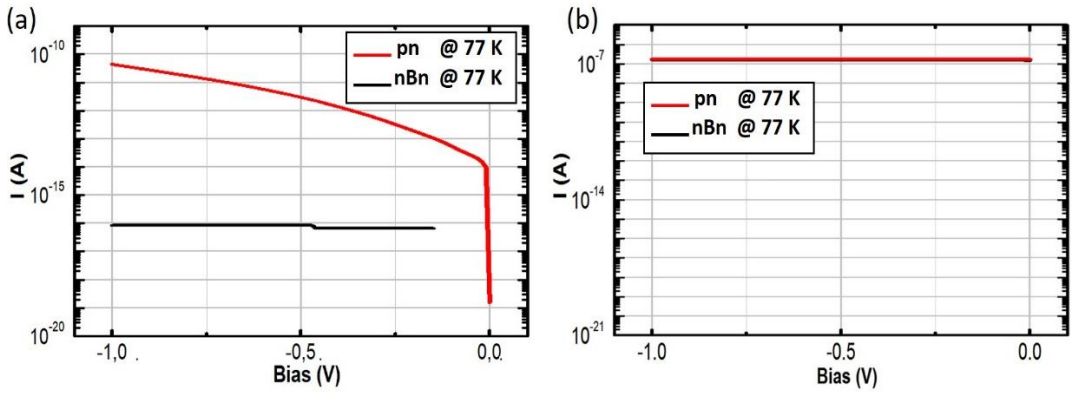

Figure 6.22. (a) Dark current characteristics of the nBn type dual-band HgCdTe detector design in MWIR band in comparison with conventional pn heterojunction (b) Photocurrent comparison between the designed nBn and pn structures in MWIR band. (Not: The photocurrent curves calculated for two structures (pn and nBn) are overlap.)

CHAPTER 7

CONCLUSION AND FUTURE WORK

In this thesis work, it has been numerically demonstrated that some of the material restrictions in barrier detector architecture can be eliminated in the conventional photodetector technology via bandgap engineering techniques. Synopsys Sentaurus TCAD commercial device simulator was used to conduct simulations and analyses by calculating the Poisson, continuity, and current equations with high precision. In this study, compositionally graded and delta-doped layers were utilized to attain InGaAs and HgCdTe nBn type barrier detector configurations with zero valence band offset.

For SWIR band InGaAs nBn detectors, lattice-mismatched InGaAs and lattice-matched InAlAs were used for the barrier material. At least 20 and 40 times improvement, respectively, was shown in the dark current level, without compromising any photoresponse, when compared to a conventional InGaAs pn junction via the suppression of the surface leakage and G-R current mechanisms. Moreover, the same method was used to obtain an e-SWIR /SWIR InGaAs dual-band nBn detector structure.

In the case of HgCdTe material systems, strong suppression of the G-R and TAT currents was demonstrated with the nBn designed structures in SWIR, MWIR and LWIR bands for the alternative substrate HgCdTe technology. The HgCdTe dual-band nBn detector configuration was also examined numerically in the MWIR/LWIR bands using compositionally graded and delta-doped layers.

Due to the flexibility of this method, the length and thickness of the barrier can be adjusted while at the same time zero valence band offset can be achieved for the compositionally bandgap adjustable materials.

Further works can be listed as follows:

- In the light of the simulations, the pixel structure of the InGaAs nBn detector will be grown and the detector fabrication will be conducted within the scope of the TUBİTAK 118E771 project using METU-KANAL equipment. In this project, crystal growth is planned to be made with METU-KANAL III-V Riber Epinat MBE reactor. According to the results of the XRD study after crystal growth, infrared detector fabrication processes will begin. First, grown wafer will be cut into slices, then with the help of the lithography method, etching, surface passivation coating, and ohmic contact creation will be performed, and finally, wire bonding will be made. For detector characterization, current-voltage and photoresponse measurements will be made.
- The reduction of Auger recombination will be numerically investigated in nBn HgCdTe detectors.
- The performance of the nBn detector structure in optical communication field will be numerically investigated.

REFERENCES

[1] R. V. Prakash, *Infrared thermography*. 2012.

[2] A. Rogalski, *Infrared Detectors*, vol. 41, no. 14. CRC Press, 2010.

[3] W. Herschel, " II. Experiments on the refrangibility of the invisible rays of the sun ," *Philos. Mag.*, vol. 8, no. 29, pp. 9–15, 1800, doi: 10.1080/14786440008562602.

[4] E. Velmre, "Thomas Johann Seebeck and his contribution to the modern science and technology," *BEC 2010 - 2010 12th Bienn. Balt. Electron. Conf. Proc. 12th Bienn. Balt. Electron. Conf.*, pp. 17–24, 2010, doi: 10.1109/BEC.2010.5631216.

[5] A. Rogalski, "History of infrared detectors," *Opto-Electronics Rev.*, vol. 20, no. 3, pp. 77–85, Jan. 2012, doi: 10.2478/s11772-012-0037-7.

[6] T. W. Case, "'Thalofide Cell'a New Photo-Electric Substance," *Phys. Rev.*, vol. 15, no. 4, pp. 289–292, Apr. 1920, doi: 10.1103/PhysRev.15.289.

[7] A. Rogalski, "Infrared detectors: An overview," *Infrared Phys. Technol.*, vol. 43, no. 3–5, pp. 187–210, 2002, doi: 10.1016/S1350-4495(02)00140-8.

[8] C. Beşikci, *EE514 Infrared Devices and Systems METU, Lecture Notes*. 2012.

[9] D. S. Tezcan, S. Eminoglu, and T. Akin, "A low-cost uncooled infrared microbolometer detector in standard CMOS technology," *IEEE Trans. Electron Devices*, vol. 50, no. 2, pp. 494–502, 2003, doi: 10.1109/TED.2002.807453.

[10] Y. Arslan, "High performance focal plane array technologies from short to long wavelength infrared bands," Middle East Technical University, 2014.

[11] P. Martyniuk and W. Gawron, "Barrier detectors versus homojunction photodiode," *Metrol. Meas. Syst.*, vol. 21, no. 4, pp. 675–684, 2014, doi: 10.2478/mms-2014-0058.

[12] M. Casalino, “Recent Advances in Silicon Photodetectors Based on the Internal Photoemission Effect,” *New Res. Silicon - Struct. Prop. Technol.*, 2017, doi: 10.5772/67720.

[13] L. Esaki and R. Tsu, “Superlattice and Negative Differential Conductivity in Semiconductor,” *IBM J. Res. Dev.*, vol. 14, no. 1, pp. 61–65, 1970.

[14] Y. Arslan, T. Colakoglu, and C. Besikci, “Diffraction-grating-coupled high quantum efficiency InP/InGaAs quantum well infrared photodetector focal plane array,” *IEEE J. Quantum Electron.*, vol. 49, no. 2, pp. 186–195, 2013, doi: 10.1109/JQE.2012.2237160.

[15] M. A. Dem’yanenko *et al.*, “AlGaAs/GaAs Quantum Well Infrared Photodetectors,” *Two-dimensional Mater. Photodetector*, 2018, doi: 10.5772/intechopen.71266.

[16] U. Serincan, B. Arikan, and O. Şenel, “Direct growth of type II InAs/GaSb superlattice MWIR photodetector on GaAs substrate,” *Superlattices Microstruct.*, vol. 120, no. March, pp. 15–21, 2018, doi: 10.1016/j.spmi.2018.05.020.

[17] O. Temel, “Molecular Beam Epitaxy Growth of InP/InGaAs Structures for Short Wavelength Infrared Photodetectors,” Middle East Technical University, 2014.

[18] M. Henini and M. Razeghi, *Handbook of Infrared Detection Technologies*. Elsevier Science, 2002.

[19] B. G. Streetman and S. K. Banerjee, *Solid State Electronic Devices*, 6th ed. Prentice Hall.

[20] G. R. Savich, “Analysis and Suppression of Dark Currents in Mid-Wave Infrared Photodetectors by,” University of Rochester, 2015.

[21] G. R. Savich, D. E. Sidor, X. Du, C. P. Morath, V. M. Cowan, and G. W. Wicks, “Diffusion current characteristics of defect-limited nBn mid-wave infrared detectors,” *Appl. Phys. Lett.*, vol. 106, no. 17, 2015, doi: 10.1063/1.4919450.

[22] D. R. Rhiger, “Performance comparison of long-wavelength infrared type II superlattice devices with HgCdTe,” *J. Electron. Mater.*, vol. 40, no. 8, pp. 1815–1822, 2011, doi: 10.1007/s11664-011-1653-6.

[23] A. Rogalski, K. Adamiec, and J. Rutkowski, *Narrow-Gap Semiconductor Photodiodes*. SPIE, 2000.

[24] P. Emelie, “HgCdTe Auger-Suppressed Infrared Detectors Under Non-Equilibrium Operation,” The University of Michigan, 2009.

[25] R. F. Pierret and G. W. Neudeck., *Advanced Semiconductor Fundamentals*, 2nd ed. New Jersey, 1987.

[26] M. Razeghi, *Fundamentals of solid state engineering*, 4th ed. Evanston, IL, USA: Springer, 2018.

[27] J. M. Ruiz-Palmero and H. Jackel, “Impact of Surface Traps on Downscaled InP / lnGaAs DHBTs,” *Proc. 7th Int. Conf. Solid- State Integr. Circuits Technol., Oct. 2004, pp. 1003–1006*, pp. 1003–1006, 2004, doi: 10.1109/ICSICT.2004.1436675.

[28] R. N. Hall, “Recombination processes in semiconductors,” *Proc. IEE - Part B Electron. Commun. Eng.*, vol. 106, no. 17S, pp. 923–931, May 1959, doi: 10.1049/pi-b-2.1959.0171.

[29] D. K. Schroder, *Schroder, Dieter K. Semiconductor material and device characterization*, Third. John Wiley & Sons, 2015.

[30] E. A. Kadlec, “Progress Towards Competitive III-V Infrared Detectors : Fundamental Material Characterization and Techniques,” University of New Mexico, 2017.

[31] S.Rein, *Lifetime Spectroscopy*. Springer, 2005.

[32] S. M. Sze, *Physics of Semiconductor Devices*, Third. Hsinchu: Wiley Interscience, 20007.

[33] B. T. Marozas, W. D. Hughes, X. Du, D. E. Sidor, G. R. Savich, and G. W. Wicks, "Surface dark current mechanisms in III-V infrared photodetectors [Invited]," *Opt. Mater. Express*, vol. 8, no. 6, p. 1419, 2018, doi: 10.1364/ome.8.001419.

[34] J. F. Klem, J. K. Kim, M. J. Cich, S. D. Hawkins, T. R. Fortune, and J. L. Rienstra, "Comparison of nBn and nBp mid-wave barrier infrared photodetectors," *Quantum Sens. Nanophotonic Devices VII*, vol. 7608, p. 76081P, 2010, doi: 10.1117/12.842772.

[35] P. Martyniuk, M. Kopytko, and A. Rogalski, "Barrier infrared detectors," vol. 22, no. 2, pp. 127–146, 2014, doi: 10.2478/s11772.

[36] A. Daniels, *Field guide to infrared systems*, SPIE field. 2007.

[37] A. M. White, "Infra red detectors," *United States Pat.*, no. 19, 1987.

[38] S. Maimon and G. W. Wicks, "nBn detector, an infrared detector with reduced dark current and higher operating temperature," *Appl. Phys. Lett.*, vol. 89, no. 15, pp. 1–4, 2006, doi: 10.1063/1.2360235.

[39] G. R. Savich, J. R. Pedrazzani, D. E. Sidor, and G. W. Wicks, "Benefits and limitations of unipolar barriers in infrared photodetectors," *Infrared Phys. Technol.*, vol. 59, pp. 152–155, 2013, doi: 10.1016/j.infrared.2012.12.031.

[40] G. R. Savich, J. R. Pedrazzani, D. E. Sidor, S. Maimon, and G. W. Wicks, "Use of unipolar barriers to block dark currents in infrared detectors," in *Infrared Technology and Applications XXXVII*, 2011, vol. 8012, p. 80122T, doi: 10.1117/12.884075.

[41] J. R. Pedrazzani, S. Maimon, and G. W. Wicks, “Use of nBn structures to suppress surface leakage currents in unpassivated InAs infrared photodetectors,” *Electron. Lett.*, vol. 44, no. 25, pp. 1487–1488, 2008, doi: 10.1049/el:20082925.

[42] D. E. Sidor, G. R. Savich, X. Du, and G. W. Wicks, “Infrared Physics & Technology Flat-band pn-based unipolar barrier photodetector,” vol. 70, pp. 111–114, 2015, doi: 10.1016/j.infrared.2014.09.037.

[43] A. P. Craig *et al.*, “Short-wave infrared barriode detectors using InGaAsSb absorption material lattice matched to GaSb Short-wave infrared barriode detectors using InGaAsSb absorption material lattice matched to GaSb,” vol. 201103, 2015, doi: 10.1063/1.4921468.

[44] M. Reine, J. Schuster, B. Pinkie, and E. Bellotti, “Numerical Simulation and Analytical Modeling of InAs nBn Infrared Detectors with p -Type Barriers,” vol. 42, no. 11, pp. 3015–3033, 2013, doi: 10.1007/s11664-013-2685-x.

[45] M. Reine, B. Pinkie, J. Schuster, and E. Bellotti, “Numerical Simulation and Analytical Modeling of InAs n B n Infrared Detectors with n -Type Barrier Layers,” vol. 43, no. 8, pp. 2915–2934, 2014, doi: 10.1007/s11664-014-3148-8.

[46] P. Martyniuk, W. Gawron, and A. Rogalski, “Theoretical modeling of HOT HgCdTe barrier detectors for the mid-wave infrared range,” *J. Electron. Mater.*, vol. 42, no. 11, pp. 3309–3319, 2013, doi: 10.1007/s11664-013-2737-2.

[47] P. Martyniuk and A. Rogalski, “Theoretical modeling of InAsSb / AlAsSb barrier detectors for higher- operation-temperature conditions,” 2015, doi: 10.1117/1.OE.53.1.017106.

[48] N. D. Akhavan, G. A. Umana-Membreno, G. Jolley, J. Antoszewski, and L. Faraone, “A method of removing the valence band discontinuity in HgCdTe-based nBn detectors,” *Appl. Phys. Lett.*, vol. 105, no. 12, pp. 2012–2016, 2014, doi: 10.1063/1.4896577.

[49] K. Jo, M. Kopytko, and J. Wro, “Engineering the Bandgap of Unipolar HgCdTe-Based nBn Infrared Photodetectors,” vol. 44, no. 1, pp. 6–8, 2015, doi: 10.1007/s11664-014-3511-9.

[50] N. D. Akhavan, G. A. Umana-Membreno, R. Gu, M. Asadnia, J. Antoszewski, and L. Faraone, “Superlattice Barrier HgCdTe nBn Infrared Photodetectors: Validation of the Effective Mass Approximation,” *IEEE Trans. Electron Devices*, vol. 63, no. 12, pp. 4811–4818, 2016, doi: 10.1109/TED.2016.2614677.

[51] J. W. Scott, C. E. Jones, E. J. Caine, and C. A. Cockrum, “Sub-pixel nBn detector,” U.S. Patent No. 8,044,435, 2011.

[52] S. J. Lee, S. K. Noh, E. Plis, S. Krishna, and K. S. Lee, “Subband transitions in dual-band n-B-n InAs/GaSb superlattice infrared photodetector identified by photoresponse spectra,” *Appl. Phys. Lett.*, vol. 95, no. 10, 2009, doi: 10.1063/1.3212738.

[53] E. Plis, S. S. Krishna, E. P. Smith, S. Johnson, and S. Krishna, “Voltage controllable dual-band response from InAs / GaSb strained layer superlattice detectors with nBn design,” vol. 47, no. 2, 2011, doi: 10.1049/el.2010.3096.

[54] S. S. Krishna *et al.*, “Bias Switchable Dual-Band InAs / GaSb Superlattice Detector With pBp Architecture Bias Switchable Dual-Band InAs / GaSb,” vol. 3, no. 2, 2011, doi: 10.1109/JPHOT.2011.2125949.

[55] A. Haddadi, R. Chevallier, G. Chen, A. M. Hoang, and M. Razeghi, “Bias-selectable dual-band mid- / long-wavelength infrared photodetectors based on InAs / InAs 1 2 x Sb x type-II superlattices,” vol. 011104, 2015, doi: 10.1063/1.4905565.

[56] N. D. Akhavan, G. Jolley, G. A. Umana-membreno, J. Antoszewski, and L. Faraone, “Design of Band Engineered HgCdTe nBn Detectors for MWIR and LWIR Applications,” vol. 62, no. 3, pp. 722–728, 2015.

[57] P. Klipstein *et al.*, “Reducing the cooling requirements of mid-wave IR detector arrays,” pp. 10–13, doi: 10.1117/2.1201111.003919.

[58] P. C. Klipstein, “XB n n and XB p p infrared detectors,” vol. 425, pp. 351–356, 2015, doi: 10.1016/j.jcrysgro.2015.02.075.

[59] F. Uzgur, U. Karaca, E. Kizilkan, and S. Kocaman, “All InGaAs Unipolar Barrier Infrared Detectors,” *IEEE Trans. Electron Devices*, vol. 65, no. 4, pp. 1397–1403, 2018, doi: 10.1109/TED.2018.2804483.

[60] P. Klipstein, “Depletion-Less Photodiode With Suppressed Dark Current and Method for Producing the Same,” 2005.

[61] A. Khoshakhlagh *et al.*, “Bias dependent dual band response from InAs / Ga (In) Sb type II strain layer superlattice detectors Bias dependent dual band response from InAs / Ga „ In … Sb type II strain layer superlattice detectors,” vol. 263504, pp. 1–4, 2007, doi: 10.1063/1.2824819.

[62] P. Klipstein, “"XB n " barrier photodetectors for high sensitivity and high operating temperature infrared sensors,” vol. 6940, p. 69402U, 2008, doi: 10.1117/12.778848.

[63] D. Z. Ting *et al.*, “A high-performance long wavelength superlattice complementary barrier infrared detector A high-performance long wavelength superlattice complementary barrier infrared detector,” vol. 023508, pp. 54–57, 2009, doi: 10.1063/1.3177333.

[64] S. Maimon, “Reduced dark current photodetector,” U.S.Patent No. 7,687,871, 2010.

[65] G. R. Savich, J. R. Pedrazzani, S. Maimon, and G. W. Wicks, “Suppression of surface leakage currents using molecular beam epitaxy-grown unipolar barriers Suppression of surface leakage currents using molecular beam epitaxy-grown unipolar barriers,” vol. 18, no. 2010, 2016, doi: 10.1116/1.3276513.

[66] G. R. Savich, J. R. Pedrazzani, D. E. Sidor, S. Maimon, and G. W. Wicks, “Dark current filtering in unipolar barrier infrared detectors,” *Appl. Phys. Lett.*, vol. 99, no. 12, pp. 2009–2012, 2011, doi: 10.1063/1.3643515.

[67] C. Liu, Y. Li, Y. Zeng, and E. T. Al, “Progress in Antimonide Based III-V Compound Semiconductors and Devices,” vol. 2010, no. August, pp. 617–624, 2010, doi: 10.4236/eng.2010.28079.

[68] A. W. K. Liu *et al.*, “MBE growth of Sb-based bulk nBn infrared photodetector structures on 6-inch GaSb substrates,” in *Infrared Technology and Applications XLI*, 2015, vol. 9451, no. June 2015, p. 94510T, doi: 10.1117/12.2178122.

[69] P. Norton, “HgCdTe infrared detectors,” *Opto-electronics Rev.*, vol. 10, no. 3, pp. 159–174, 2002, doi: 10.1016/b978-012265320-9/50076-3.

[70] J. R. Pedrazzani, “Characteristics of InAs-Based nBn Photodetectors Grown by Molecular Beam Epitaxy by,” University of Rochester, 2010.

[71] J. B. Rodriguez *et al.*, “NBn structure based on InAs/GaSb type-II strained layer superlattices,” *Appl. Phys. Lett.*, vol. 91, no. 4, pp. 1–3, 2007, doi: 10.1063/1.2760153.

[72] B. M. Nguyen, D. Hoffman, P. Y. Delaunay, and M. Razeghi, “Dark current suppression in type II InAsGaSb superlattice long wavelength infrared photodiodes with M-structure barrier,” *Appl. Phys. Lett.*, vol. 91, no. 16, pp. 89–92, 2007, doi: 10.1063/1.2800808.

[73] A. M. Itsuno, J. D. Phillips, and S. Velicu, “Mid-wave infrared HgCdTe nBn photodetector,” *Appl. Phys. Lett.*, vol. 100, no. 16, pp. 1–4, 2012, doi: 10.1063/1.4704359.

[74] N. D. Akhavan, G. A. Umana-Membreno, R. Gu, J. Antoszewski, and L. Faraone, “Optimization of Superlattice Barrier HgCdTe nBn Infrared Photodetectors Based on an NEGF Approach,” *IEEE Trans. Electron Devices*, vol. 65, no. 2, pp. 591–598, 2018, doi: 10.1109/TED.2017.2785827.

[75] J. F. Klem, J. K. Kim, M. J. Cich, G. A. Keeler, S. D. Hawkins, and T. R. Fortune, “Mesa-isolated InGaAs photodetectors with low dark current,” *Appl. Phys. Lett.*, vol. 95, no. 3, pp. 2–5, 2009, doi: 10.1063/1.3184807.

[76] J. F. Klem, J. K. Kim, M. J. Cich, S. D. Hawkins, T. R. Fortune, and J. L. Rienstra, “Comparison of nBn and nBp mid-wave barrier infrared photodetectors,” *Quantum Sens. Nanophotonic Devices VII*, vol. 7608, no. April, p. 76081P, 2010, doi: 10.1117/12.842772.

[77] Chanh Nguyen, Takyiu Liu, M. Chen, Hsiang-Chih Sun, and D. Rensch, “AlInAs/GaInAs/InP double heterojunction bipolar transistor with a novel base-collector design for power applications,” *IEEE Electron Device Lett.*, vol. 17, no. 3, pp. 133–135, Mar. 1996, doi: 10.1109/55.485191.

[78] H. Kroemer, “Nobel Lecture: Quasielectric fields and band offsets: teaching electrons new tricks,” *Rev. Mod. Phys.*, vol. 73, no. 3, pp. 783–793, Oct. 2001, doi: 10.1103/RevModPhys.73.783.

[79] E. F. Schubert, *Physical Foundations of Solid-State Devices*, vol. 31, no. 1. 2015.

[80] F. Capasso, “Compositionally Graded Semiconductors and their Device Applications,” in *Annual Review of Materials Science*, vol. 16, 1988, pp. 70–98.

[81] B. F. Levine, W. T. Tsang, C. G. Bethea, and F. Capasso, “Electron drift velocity measurement in compositionally graded Al xGa1-xAs by time-resolved optical picosecond reflectivity,” *Appl. Phys. Lett.*, vol. 41, no. 5, pp. 470–472, 1982, doi: 10.1063/1.93535.

[82] B. F. Levine *et al.*, “Measurement of high electron drift velocity in a submicron, heavily doped graded gap AlxGa1-xAs layer,” *Appl. Phys. Lett.*, vol. 42, no. 9, pp. 769–771, 1983, doi: 10.1063/1.94094.

[83] F. Uzgur and S. Kocaman, “InGaAs nBn SWIR detector design with lattice-matched InAlGaAs barrier,” *Turkish J. Electr. Eng. Comput. Sci.*, vol. 27, no. 1, pp. 1–10, 2019, doi: 10.3906/elk-1802-197.

[84] Sentaurus, “Sentaurus sDevice 2015,” *Simulation*, no. June, p. 2015, 2009.

[85] C. K. Maiti, *Introducing Technology Computer-Aided Design (TCAD): Fundamentals, Simulations, and Applications*. CRC Press, 2017.

[86] A. Vais, “Physical Simulation of GaN based HEMT,” 2012.

[87] B. V. Popescu, “Modeling and Simulation of InAs Nanowire Transistors,” 2015.

[88] M. Boroditsky *et al.*, “Surface recombination measurements on III-V candidate materials for nanostructure light-emitting diodes,” *J. Appl. Phys.*, vol. 87, no. 7, pp. 3497–3504, 2000, doi: 10.1063/1.372372.

[89] R. K. Ahrenkiel, R. Ellingson, S. Johnston, and M. Wanlass, *Recombination lifetime of In0.53Ga0.47As as a function of doping density*, vol. 72, no. 26. 1998.

[90] M. D. Pashley, K. W. Haberern, R. M. Feenstra, and P. D. Kirchner, “Different Fermi-level pinning behavior on n- and p-type GaAs(001),” *Phys. Rev. B*, vol. 48, no. 7, pp. 4612–4615, 1993, doi: 10.1103/PhysRevB.48.4612.

[91] A. A. Guzev *et al.*, “The electrical properties of HgCdTe layers grown by MBE on Si and P + / n junction formed on its basis MoP-IPRM-036,” vol. 59, no. 2013, pp. 2015–2016, 2016.

[92] V. Balynas, A. Krotkus, A. Stalnionis, A. T. Gorelionok, N. M. Shmidt, and J. A. Tellefsen, “Time-resolved, hot-electron conductivity measurement using an electro-optic sampling technique,” *Appl. Phys. A Solids Surfaces*, vol. 51, no. 4, pp. 357–360, 1990, doi: 10.1007/BF00324321.

[93] U. Karaca, “High performance near/short wavelength infrared megapixel InGaAs focal plane array fabrication development and new design proposals,” 2018.

[94] M. P. Hansen and D. S. Malchow, “Overview of SWIR detectors, cameras, and applications,” *Thermosense XXX*, vol. 6939, no. March 2008, p. 69390I, 2008, doi: 10.1117/12.777776.

[95] D. Malchow, J. Battaglia, R. Brubaker, and M. Ettenberg, “High speed short wave infrared (SWIR) imaging and range gating cameras,” *Thermosense XXIX*, vol. 6541, no. April 2007, p. 654106, 2007, doi: 10.1117/12.721747.

[96] R. B. Smith, *Introduction to hyperspectral imaging*. 2006.

[97] P. Bhattacharya, *Properties of Lattice-matched and Strained Indium Gallium Arsenide*. INSPEC, UK, 1993.

[98] Y. Ozer and S. Kocaman, “Generation recombination suppression via depletion engineered heterojunction for alternative substrate MWIR HgCdTe infrared photodetectors,” vol. 143103, 2017, doi: 10.1063/1.5000116.

[99] M. H. Dolas and S. Kocaman, “Fully Depleted InP Nano-Layer for in-Device Passivation of InGaAs SWIR Detectors,” vol. 3106, no. c, pp. 1–4, 2017, doi: 10.1109/LED.2017.2763616.

[100] Y. Arslan, F. Oguz, and C. Besikci, “640×512 Extended Short Wavelength Infrared In0.83Ga0.17As Focal Plane Array,” vol. 50, no. 12, pp. 957–964, 2014, doi: 10.1109/JQE.2014.2363938.

[101] F. Uzgur, U. Karaca, E. Kizilkan, and S. Kocaman, “Al/Sb free InGaAs unipolar barrier infrared detectors,” in *SPIE Defense + Security, 2017, Anaheim, California, United States*, vol. 1017706, no. May 2017, doi: 10.1117/12.2262519.

[102] K. R. Linga, “Design, fabrication and characterization of high performance InGaAs/InP focal plane arrays in the 1–2.6 μm wavelength region,” PhD. dissertation,” New Jersey Inst. Technol., Newark, NJ, USA, 1997.

[103] F. Rutz, P. Kleinow, R. Aidam, W. Bronner, L. Kirste, and M. Walther, “InGaAs infrared detector development for SWIR imaging applications,” *Electro-Optical Infrared Syst. Technol. Appl. X*, vol. 8896, p. 88960C, 2013, doi: 10.1117/12.2026879.

[104] J. Tan, A. Baiano, R. Ishihara, and K. Beenakker, “2D Simulation of Hot-Carrier-Induced Degradation and Reliability Analysis for Single Grain Si TFTs,” *Methodology*, no. June 2016, pp. 600–604, 2016.

[105] D. P. Mullin and H. H. Wieder, “Surface and interfacial properties of Ga0. 47In0. 53As–Al2O3 MIS structures.,” *J. Vac. Sci. Technol. B Microelectron. Nanom. Struct.*, vol. 1, no. 3, pp. 782–786, 1983, doi: 10.1116/1.582692.

[106] E. Takeda, C. Yang, and A. Miura-Hamada, *Hot-Carrier Effects in MOS Devices*. San Diego, CA: Academic Press, 1995.

[107] J. M. Moison and M. Bensoussan, “Surface recombination, surface states and Fermi level pinning,” *Rev. Phys. Appl*, vol. 22, no. 5, pp. 293–297, 1987, doi: 10.1051/rphysap:01987002205029300.

[108] P. A. Alekseev *et al.*, “Unified mechanism of the surface Fermi level pinning in III-As nanowires,” *Nanotechnology*, vol. 29, no. 31, pp. 1–7, Oct. 2017, doi: 10.1088/1361-6528/aac480.

[109] M. L. Vatsia, K. U. Stich, and D. Dunlap, “Night-sky radiant sterance from 450 to 2000 nanometers,” *ARMY NIGHT Vis. LAB FORT BELVOIR VA*, 1972.

[110] D. Olego, T. Y. Chang, E. Silberg, E. A. Caridi, and A. Pinczuk, “Compositional dependence of band-gap energy and conduction-band effective mass of In1-x-yGaxAlyAs lattice matched to InP,” *Appl. Phys. Lett.*, vol. 41, no. 5, pp. 476–478, 1982, doi: 10.1063/1.93537.

[111] T. S. Lee *et al.*, “MWIR detectors on HgCdTe grown by MBE on 3-inch diameter silicon substrates,” vol. 5564, pp. 113–122, 2004, doi: 10.1117/12.568012.

[112] F. Capasso, “Band-Gap Engineering: From Physics and Materials To New Semiconductor Devices.,” *Science (80-.).*, vol. 235, no. 4785, pp. 172–176, 1987, doi: 10.1126/science.235.4785.172.

[113] X. D. Wang *et al.*, “Dark current simulation of InP/In 0.53Ga 0.47As/InP p-i-n photodiode,” *Opt. Quantum Electron.*, vol. 40, no. 14-15 SPEC. ISS., pp. 1261–1266, 2008, doi: 10.1007/s11082-009-9279-0.

[114] H. Yuan, M. Meixell, J. Zhang, P. Bey, J. Kimchi, and L. C. Kilmer, “Low dark current small pixel large format InGaAs 2D photodetector array development at Teledyne Judson Technologies,” *Infrared Technol. Appl. XXXVIII*, vol. 8353, no. 1, pp. 835309-835309–8, 2012, doi: 10.1117/12.921232.

[115] M. MacDougal, J. Geske, C. Wang, and D. Follman, “Low-Light-Level InGaAs focal plane arrays with and without illumination,” *Infrared Technol. Appl. XXXVI*, vol. 7660, p. 76600K, 2010, doi: 10.1117/12.852605.

[116] F. Uzgur and S. Kocaman, “A dual-band HgCdTe nBn infrared detector design,” vol. 1112903, no. September 2019, p. 2, 2019, doi: 10.1117/12.2529240.

[117] E. P. G. Smith *et al.*, “HgCdTe focal plane arrays for dual-color mid- and long-wavelength infrared detection,” *J. Electron. Mater.*, vol. 33, no. 6, pp. 509–516, 2004, doi: 10.1007/s11664-004-0039-4.

[118] M. B. Reine *et al.*, “Independently accessed back-to-back HgCdTe photodiodes: A new dual-band infrared detector,” *J. Electron. Mater.*, vol. 24, no. 5, pp. 669–679, 1995, doi: 10.1007/BF02657977.

[119] M. Vallone, M. Goano, F. Bertazzi, G. Ghione, R. Wollrab, and J. Ziegler, “Modeling photocurrent spectra of single-color and dual-band HgCdTe photodetectors: Is 3D simulation unavoidable?,” *J. Electron. Mater.*, vol. 43, no. 8, pp. 3070–3076, 2014, doi: 10.1007/s11664-014-3252-9.

[120] S. Velicu *et al.*, “Two color high operating temperature HgCdTe photodetectors grown by molecular beam epitaxy on silicon substrates,” *Nanophotonics Macrophotonics Sp. Environ. VII*, vol. 8876, no. September, p. 887608, 2013, doi: 10.1117/12.2025301.

[121] M. F. Vilela *et al.*, “High-performance M/LWIR Dual-Band HgCdTe/Si focal-plane arrays,” *J. Electron. Mater.*, vol. 42, no. 11, pp. 3231–3238, 2013, doi: 10.1007/s11664-013-2798-2.

[122] W. Hu *et al.*, “128 × 128 long-wavelength/mid-wavelength two-color HgCdTe infrared focal plane array detector with ultralow spectral cross talk,” *Opt. Lett.*, vol. 39, no. 17, p. 5184, 2014, doi: 10.1364/ol.39.005184.

[123] B. Pinkie and E. Bellotti, “Numerical simulation of spatial and spectral crosstalk in two-color MWIR/LWIR HgCdTe infrared detector arrays,” *J. Electron. Mater.*, vol. 42, no. 11, pp. 3080–3089, 2013, doi: 10.1007/s11664-013-2647-3.

[124] P. K. Saxena, “Numerical study of dual band (MW/LW) IR detector for performance improvement,” *Def. Sci. J.*, vol. 67, no. 2, pp. 141–148, 2017, doi: 10.14429/dsj.67.11177.

[125] A. D. D. Dwivedi, A. Pranav, G. Gupta, and P. Chakrabarti, “Numerical Simulation of HgCdTe Based Simultaneous MWIR/LWIR Photodetector for Free Space Optical Communication,” *Int. J. Adv. Appl. Phys. Res.*, vol. 2, no. 2, pp. 20–27, 2015, doi: 10.15379/2408-977x.2015.02.02.4.

[126] M. Kopytko, W. Gawron, A. Kębłowski, D. Stępień, P. Martyniuk, and K. Jóźwikowski, “Numerical analysis of HgCdTe dual-band infrared detector,” *Opt. Quantum Electron.*, vol. 51, no. 3, pp. 1–8, 2019, doi: 10.1007/s11082-019-1755-6.

[127] H. Koçer, “Numerıcal Modelıng and Optımızatıon of HgCdTe Infrared Photodetectors for Thermal Imaging,” Middle East Technical University, 2011.

[128] S. Kasap and P. Capper, *Springer Handbook of Electronic and Photonic Materials*. Springer, 2017.

[129] E. P. G. Smith *et al.*, “Status of Two-Color and Large Format HgCdTe FPA Technology at Raytheon Vision Systems,” *Quantum Sens. Nanophotonic Devices III*, vol. 6127, no. 61271F, 2006, doi: 10.1117/12.666668.

[130] J. Armstrong, M. Skokan, M. Kinch, and J. Luttmer, “HDVIP five-micron pitch HgCdTe focal plane arrays,” *SPIE Def. + Secur. 2014, Balt. Maryland, United States*, vol. 907033, doi: https://doi.org/10.1117/12.2053286.

[131] E. Şaşmaz, “Molecular beam epitaxial growth and characterization of extended short wavelength infrared mercury cadmium telluride detectors.,” Middle East Technical University, 2017.

[132] M. Reddy *et al.*, “MBE growth of HgCdTe on large-area Si and CdZnTe wafers for SWIR, MWIR and LWIR detection,” *J. Electron. Mater.*, vol. 37, no. 9, pp. 1274–1282, 2008, doi: 10.1007/s11664-008-0428-1.

[133] V. M. Bazovkin *et al.*, “High operating temperature SWIR p + – n FPA based on MBE-grown HgCdTe / Si (0 1 3),” *INFRARED Phys. Technol.*, vol. 76, pp. 72–74, 2016, doi: 10.1016/j.infrared.2016.01.018.

[134] A. V Voitsekhovskii *et al.*, “Admittance of metal – insulator – semiconductor structures based on graded-gap HgCdTe grown by molecular-beam epitaxy on GaAs substrates,” *INFRARED Phys. Technol.*, vol. 71, pp. 236–241, 2015, doi: 10.1016/j.infrared.2015.04.009.

[135] M. Carmody *et al.*, “Long wavelength infrared, molecular beam epitaxy, HgCdTe-on-Si diode performance,” *J. Electron. Mater.*, vol. 33, no. 6, pp. 531–537, 2004, doi: 10.1007/s11664-004-0042-9.

[136] K. Jowikowski and A. Rogalski, “Effect of Dislocations on Performance of LWIR HgCdTe Photodiodes,” *J. Electron. Mater.*, vol. 29, no. 6, pp. 736–741, 2000, doi: https://doi.org/10.1007/s11664-004-0042-9.

[137] R. S. List, “Electrical Effects of Dislocations and Other Crystallographic Defects in Hgo . 78Cdo . 22Te n-on-p Photodiodes,” *J. Electron. Mater.*, vol. 22, no. 8, 1993.

[138] Y. Ozer and S. Kocaman, “Generation recombination suppression via depletion engineered heterojunction for alternative substrate MWIR HgCdTe infrared photodetectors,” *J. Appl. Phys.*, vol. 122, no. 14, 2017, doi: 10.1063/1.5000116.

[139] F. Uzgur and S. Kocaman, “Barrier engineering for HgCdTe unipolar detectors on alternative substrates,” *Infrared Phys. Technol.*, vol. 97, no. December 2018, pp. 123–128, 2019, doi: 10.1016/j.infrared.2018.12.026.

[140] J. B. Varesi, R. E. Bornfreund, A. C. Childs, and W. A. Radford, “Fabrication of High-Performance Large-Format MWIR Focal Plane Arrays from MBE-Grown HgCdTe on 4 ≤ Silicon Substrates,” vol. 30, no. 6, pp. 566–573, 2001.

[141] A. I. D. Souza, J. Bajaj, R. E. D. E. Wames, and D. D. Edwall, “MWIR DLPH HgCdTe Photodiode Performance Dependence on Substrate Material,” vol. 27, pp. 727–732, 1998.

[142] M. Vallone, “Physics-based simulation of narrow and wide band gap photonic devices (Ph.D. thesis),” 2016.

[143] V. C. Lopes, A. J. Syllaios, and M. C. Chen, “Minority carrier lifetime in mercury cadmium telluride,” *Semicond. Sci. Technol*, vol. 8, no. 6S, p. 824, 1993, doi: 10.1088/0268-1242/8/6S/005.

[144] Y. Nemirovsky, R. Fastow, M. Meyassed, and A. Unikovsky, “Trapping effects in HgCdTe,” in *AIP Conference Proceedings*, 1991, vol. 1829, pp. 1829–1839, doi: 10.1063/1.41060.

[145] N. D. Akhavan, G. A. Umana-Membreno, R. Gu, J. Antoszewski, and L. Faraone, “Delta Doping in HgCdTe-Based Unipolar Barrier Photodetectors,” *IEEE Trans. Electron Devices*, vol. 65, no. 10, pp. 4340–4345, 2018, doi: 10.1109/TED.2018.2861378.

CURRICULUM VITAE

PERSONAL INFORMATION

Surname, Name: Uzgur, Fatih
Nationality: Turkish (TC)
Date and Place of Birth: 13 January 1983, Kars
Marital Status: Married
Phone: +90 535 215 30 82
email: uzgur@metu.edu.tr
fatihuzgur@yahoo.com
uzgurfatih@gmail.com

EDUCATION

Degree	Institution	Year of Graduation
PhD	Middle East Technical University, Micro and Nanotechnology	2020
BS	Atatürk Üniversitesi, Matematik	2007
BS	Atatürk Üniversitesi, Fizik	2006
High School	Kağıthane İHL, İstanbul	2000

WORK EXPERIENCE

Year	Place	Enrollment
2010-2020	Middle East Technical University, Micro and Nanotechnology Department	Research Assistant

RESEARCH PROJECTS

Year	Project	Granted by	Enrollment
2019-…	Genişletilmiş SWIR Bölgesinde Çalışan Delta Katkılı nBn Yapısında Kızılötesi Dedektör	TÜBİTAK	Project Scholar
2019-2020	Kızılötesi Dedektör Takımı Geliştirilmesi (NAR) Projesi	Savunma Sanayi Başkanlığı	Researcher

FOREIGN LANGUAGES

Advanced English

PUBLICATIONS

Journal Publications:

[1] Uzgur, Fatih, and Serdar Kocaman. "Barrier engineering for HgCdTe unipolar detectors on alternative substrates." Infrared Physics & Technology 97 (2019): 123-128.

[2] Uzgur, Fatih, and Serdar Kocaman. "InGaAs nBn SWIR detector design with lattice-matched InAlGaAs barrier." Turkish Journal of Electrical Engineering & Computer Sciences 27.1 (2019): 1-10.

[3] Uzgur, Fatih, et al. "All InGaAs unipolar barrier infrared detectors." IEEE Transactions on Electron Devices 65.4 (2018): 1397-1403.

Conference Proceedings:

[1] Uzgur, Fatih, and Serdar Kocaman. "A dual-band HgCdTe nBn infrared detector design." Infrared Sensors, Devices, and Applications IX. Vol. 11129. International Society for Optics and Photonics, 2019.

[2] Uzgur, Fatih, et al. "Al/Sb free InGaAs unipolar barrier infrared detectors." Infrared Technology and Applications XLIII. Vol. 10177. International Society for Optics and Photonics, 2017.